



TECHNISCHE
UNIVERSITÄT
WIEN
Vienna | Austria



DISSERTATION

Self-excited vibrations of magnetic track brakes

Modelling, analysis and mitigation

ausgeführt zum Zwecke der Erlangung des akademischen Grades eines Doktors der
technischen Wissenschaften (Dr. techn.), eingereicht an der TU Wien, Fakultät für
Maschinenwesen und Betriebswissenschaften, von

Dipl.-Ing. Daniel Tippelt

Mat.Nr.: 0426458

unter der Leitung von:

Univ.Prof. Dipl.-Ing. Dr.techn. Johannes Edelmann
Institut für Mechanik und Mechatronik, E325-01

Wien, Juni 2022

Begutachtet von:

Prof. Dr. Manfred Plöchl
Institut für Mechanik und
Mechatronik, TU Wien

Prof. Dr. Maksym Spiryagin
Centre for Railway Engineering
CQUniversity, Australia

Eidesstattliche Erklärung

Dipl.-Ing. Daniel Tippelt

Ich erkläre an Eides statt, dass die vorliegende Arbeit nach den anerkannten Grundsätzen für wissenschaftliche Abhandlungen von mir selbstständig erstellt wurde. Alle verwendeten Hilfsmittel, insbesondere die zugrunde gelegte Literatur, sind in dieser Arbeit genannt und aufgelistet. Die aus den Quellen wörtlich entnommenen Stellen, sind als solche kenntlich gemacht. Das Thema dieser Arbeit wurde von mir bisher weder im In- noch Ausland einer Beurteilerin/einem Beurteiler zur Begutachtung in irgendeiner Form als Prüfungsarbeit vorgelegt. Diese Arbeit stimmt mit der von den Begutachterinnen/Begutachtern beurteilten Arbeit überein.

Ich nehme zur Kenntnis, dass die vorgelegte Arbeit mit geeigneten und dem derzeitigen Stand der Technik entsprechenden Mitteln (Plagiat-Erkennungssoftware) elektronisch-technisch überprüft wird. Dies stellt einerseits sicher, dass bei der Erstellung der vorgelegten Arbeit die Qualitätsvorgaben im Rahmen der geltenden Regeln zur Sicherung guter wissenschaftlicher Praxis „Code of Conduct“ an der TU Wien eingehalten wurden. Zum anderen werden durch einen Abgleich mit anderen studentischen Abschlussarbeiten Verletzungen meines persönlichen Urheberrechts vermieden.

Wien, 19. Juni 2022

Daniel Tippelt

Danksagung

Die vorliegende Arbeit wurde im Laufe meiner beruflichen Tätigkeit in der Entwicklungsabteilung für Magnetschienenbremsen bei der Knorr-Bremse GmbH in Mödling sowie am Institut für Mechanik und Mechatronik der Technischen Universität Wien, Forschungsbereich für Technische Dynamik und Fahrzeugdynamik verfasst.

Prof. Dr. Johannes Edelmann und Prof. Dr. Manfred Plöchl danke ich für die wissenschaftliche Betreuung und Begutachtung, die zahlreichen fruchtbaren Diskussionen, sowie zielgerichteten Fragen, die stets zu neuer Inspiration verhalfen. Prof. Dr. Maksym Spiryagin danke ich für die Zweitbegutachtung meiner Arbeit.

Für die Förderung meines beruflichen Weges und die Motivation für den Beginn der Dissertation gilt mein großer Dank Dr. Michael Jirout. Darüber hinaus für die firmenseitige Betreuung über den gesamten Zeitraum und seine unentwegte Ermutigung zum Abschluss der Arbeit.

Dipl.-Ing. Volker Jörgl danke ich für die forschungsorientierte Ausrichtung des Entwicklungsbereichs für Magnetschienenbremsen durch welche die vorliegende Arbeit erst möglich wurde, sowie meinen Kollegen für anregende Fachgespräche, die entgegenkommende Zusammenarbeit und angenehme Arbeitsatmosphäre.

Besonderer Dank gebührt meiner Familie, einerseits für die Entfaltung meiner Begeisterung zur Lösung technischer Problemstellungen und andererseits für die Unterstützung vor, während und nach der Entstehung dieser Dissertation.

Kurzfassung

Magnetschienenbremsen sind vom Rad-Schiene Kontakt unabhängige Bremssysteme von Schienenfahrzeugen, die im Falle von Schnellbremsungen aktiviert werden. Im Drehgestell eingebaute Elektromagnete werden auf die Schiene abgesenkt und erzeugen eine magnetische Anzugskraft zwischen Bremse und Schiene. Dadurch entsteht im Magnet-Schiene Kontakt eine Reibkraft, die durch die Struktur der Bremse auf das Drehgestell übertragen wird. Um hohe Verzögerungsspitzen bei niedrigen Geschwindigkeiten zu vermeiden, wurden Magnetschienenbremsen bisher nicht bis zum Stillstand verwendet. Um gerade bei niedrigen Rad-Schiene Kraftschlüssen die Bremswege zu verkürzen, sollen in Zukunft Magnetschienenbremsen auch bis zum Stillstand aktiv bleiben. Im niedrigen Geschwindigkeitsbereich wurden jedoch starke Vibrationen der Magnetschienenbremse festgestellt, die zu hohen mechanischen Belastungen führen und damit den Einsatz bis zum Stillstand verhindern.

Die vorliegende Dissertation beschäftigt sich mit der Identifikation von Selbsterregungsmechanismen, die für diese Vibrationen ursächlich sind. Den Beginn bilden Fahrversuche unter realen Bedingungen, deren Analyse periodische Schwingungen in einem asymmetrischen Schwingungsmodus der Bremse zeigt, deren Auftreten mit hohen Bremskräften korreliert.

Zur Erforschung des zugrunde liegenden Selbsterregungsmechanismus werden vereinfachte und detailliertere dynamische Modelle der Magnetschienenbremse entwickelt, die sich aus gekoppelten Teilmodellen in den elektrischen, magnetischen und mechanischen Domänen zusammensetzen. Dafür erforderliche Modellparameter werden aus Fahrversuchen und Laborversuchen ermittelt.

Durch Anwendung etablierter Methoden der linearen Stabilitätstheorie werden mit den vereinfachten Modellen zwei Mechanismen identifiziert, die (in Kombination) selbsterregte Schwingungen auslösen können. Einerseits führen negative Gradienten des Reibwerts zwischen Polschuhen und Schiene bei niedrigen Geschwindigkeiten zu negativen Dämpfungstermen der Systemgleichungen, wodurch eine Selbsterregung entsteht. Andererseits besteht eine träge Wechselwirkung zwischen mechanischen und elektromagnetischen Zustandsgrößen, die in ungünstigen Fällen ebenfalls zu oszillatorisch instabilem Systemverhalten führt. Beeinflusst wird diese Wechselwirkung sowohl durch geometrische Abmessungen, als auch durch den Betrag des Reibwerts, sowie Parameter des magnetischen Kreises. Bei Systemen mit mehreren Elektromagneten in Serienschaltung wird

dieser Selbsterregungsmechanismus für asymmetrische Schwingungsformen zusätzlich verstärkt. Durch Analysen im Zeitbereich werden die Energiequellen bestimmt, die für die Aufrechterhaltung der entstehenden Grenzzykel verantwortlich sind.

Anhand eines detaillierteren Mehrkörperdynamik-Modells werden die mit den vereinfachten Modellen gewonnenen Erkenntnisse überprüft sowie Bremsmanöver simuliert, die mit Fahrversuchsdaten verglichen werden. Dabei wird gezeigt, dass selbsterregte Schwingungen von Magnetschienenbremsen sowohl von Konstruktionsparametern, als auch äußeren Einflüssen wie Materialansammlungen an Reibflächen, sowie den Magnetschiene Kontaktbedingungen abhängen. Um in Zukunft selbsterregte Schwingungen bei niedrigen Geschwindigkeiten zu vermeiden, werden Konstruktionsvorschläge entwickelt, um damit das Bremsvermögen von Schienenfahrzeugen zu erhöhen.

Abstract

Magnetic track brakes are braking systems of railway vehicles independent of the wheel-rail contact, which are activated in emergency braking manoeuvres. Electromagnets installed in the bogie are lowered onto the rail and generate a magnetic attraction force between the brake and the rail. This creates a frictional force in the magnet-rail contact, which is transmitted to the bogie by the structure of the brake. To avoid high deceleration peaks, magnetic track brakes are not used until standstill of the vehicle. To reduce braking distances, especially in low wheel-rail adhesion conditions, magnetic track brakes are to remain active until standstill in the future. However, severe vibrations of a magnetic track brake were detected in vehicle tests at low velocities, leading to high mechanical loads and thus impeding this target.

This dissertation focuses on identifying the self-excitation mechanisms causing these vibrations. Vehicle tests performed under realistic operating conditions are the starting point. The analysis of these tests shows periodic vibrations in an asymmetric vibration mode of the brake correlating with high magnitudes of braking forces.

To investigate the underlying self-excitation mechanism, simplified and more detailed dynamical models of a magnetic track brake are developed, which are assembled from coupled sub-models in the electrical, magnetic and mechanical domains. Model parameters required for the models are determined from vehicle tests and laboratory experiments.

By applying established methods of linear stability theory to the simplified models, two mechanisms are identified which (in combination) may cause self-excited vibrations. On the one hand, it is found that negative gradients of the coefficient of friction in the magnet-rail contact lead to negative damping terms of the system equations, resulting in self-excitation. On the other hand, an inertial coupling exists between mechanical and electromagnetic state variables, which can also cause oscillatory unstable system behaviour. This coupling is influenced both by geometric dimensions of the track brake and by the magnitude of the coefficient of friction, as well as parameters of the magnetic circuit. For systems with multiple magnets in series connection, this self-excitation mechanism is amplified for asymmetrical oscillation modes. Time-domain analyses determine the energy sources for maintaining the resulting limit cycles.

Using a more detailed multibody dynamics model, the findings obtained with the simplified models are validated and braking manoeuvres are simulated, which are compared with

vehicle test data. It is shown that self-excited vibrations of magnetic track brakes are dependent on both design parameters and external influences such as accumulation of material on friction surfaces, as well as the magnet-rail contact conditions. To avoid self-excited vibrations at low velocities in the future, new designs are proposed to increase the braking capacity of rail vehicles.

Contents

Kurzfassung	vii
Abstract	ix
Contents	xi
1 Introduction and state of the art	1
1.1 Components and function principle of an electromagnetic track brake .	3
1.2 Known issues of magnetic track brakes	7
1.3 Aims and objectives	9
1.4 State of the art and fundamentals	10
1.5 Outline of this thesis	22
2 Vehicle and laboratory tests	23
2.1 Measurement object and measured quantities	23
2.2 Field tests on self-excited vibrations	26
2.3 Modal analysis of the magnetic track brake	36
2.4 Field tests on the coefficient of friction	40
3 Modelling the electromagnetic track brake	43
3.1 Mechanical submodels of the track brake	44
3.2 Magnetic submodels of the track brake	50
3.3 Electrical submodels of the track brake	54
3.4 Coupled system models	57
4 Linear stability analysis of a magnetic track brake	63
4.1 Linearisation and stability border	64
4.2 Numerical stability analysis	67
4.3 Analysis in the time domain and energy considerations	74
4.4 Linear analysis of the double-magnet model	85
5 Analysis of the multibody dynamics model of the track brake	91
5.1 Brake-rail contact and steady state analysis	92
5.2 Stability analysis	95
	xi

5.3	Analysis in the time domain	99
6	Mitigation of self-excited vibrations	105
6.1	Alternative design concepts	106
6.2	Comparison of the designs	109
7	Conclusions and Outlook	119
7.1	Conclusions	119
7.2	Outlook	121
A	Measurement channels	123
B	Identification of system parameters	127
B.1	Identification of contact parameters	127
B.2	Identification of the effective air-gap	130
	Bibliography	133

Introduction and state of the art

Braking systems of railway vehicles must be able to decelerate and stop trains within specified distances. For mainline trains, stopping distances are given by distances between signals which divide railway lines into controlled sectors in which only a single train may operate at once. The length of a sector, and as a result the stopping distance of a train, therefore limits the number of trains on a railway line. To guarantee safe operation, it is most relevant to keep planned stopping distances in all occurring environmental and operational conditions. However, most braking systems of railway vehicles depend on the wheel-rail contact forces which vary with different types of contaminants of the track such as moisture, dust, grease and leaves. Predicting and improving adhesion coefficients in the wheel-rail contact has been an ongoing challenge for train operators, manufacturers of braking systems and researchers for decades. Systems coping with degraded adhesion conditions nowadays are the wheel-slide-protection (WSP), sanding devices, friction enhancers and magnetic track brakes. In modern vehicles, the WSP in combination with sanding can reliably restore wheel-rail adhesion values. Friction modifiers can be applied at fixed locations in the known critical areas of railway tracks. Finally, magnetic track brakes are additional braking systems of railway vehicles which act directly on the rails instead of being dependent on the wheel-rail contact. On the one hand, magnetic track brakes contribute to the overall brake force of the train. On the other hand, magnetic track brakes have proven to enhance the wheel-rail adhesion values of succeeding wheelsets. As a result, magnetic track brakes are mandatory in mainline trains in many countries for velocities over 140 km/h. The design and application of magnetic track brakes is regulated in UIC leaflet 541-06 [1] as well as in the European standard EN16207 [2] and the Ergänzungsregelung Nr. B 012 [3] issued by the German Federal Railway Authority. Studies on brake performance were published, for example, by Arias-Cuevas and Li [4, 5] and the European Railway Research Institute [6].

It is known from the operation of magnetic track brakes that brake forces increase with decreasing velocity resulting in high peak decelerations of the vehicle when applied until

full stop. To avoid discomfort and injuries of passengers, track brakes for mainline applications therefore were deactivated in the past at velocities lower than 25 km/h. However, as demands on brake performance continuously increase, operators choose to use the track brake until (nearly) full stop. To optimise braking systems and to add additional safety margins in stopping distances, activation of track brakes until full stop is increasingly becoming a standard customer requirement.

During field tests, severe vibrations of the magnetic track brake were measured at velocities below 25 km/h causing discomfort, noise and also high loads on mechanical components. As data analyses have shown that external excitations were unlikely, it is assumed that they are of a self-exciting type. The mechanism that leads to unstable system behaviour is however unknown. Thus, it is of great interest to analyse the vibrations in detail and to explore the mechanisms causing them. To prevent self-excited vibrations to occur in future designs of magnetic track brakes, it is essential to be able to predict them using mathematical models. Subsequently, methods for stabilising the system can be developed. This thesis focuses on analysing, modelling and mitigating self-excited vibrations of magnetic track brakes.

This first chapter is aimed at providing an insight into the mechanical design and function of magnetic track brakes. Furthermore, an overview of the methods used in this thesis and relevant literature is given. Finally, the chapter defines the aims and objectives and gives an overview on the structure of this thesis.

1.1 Components and function principle of an electromagnetic track brake

According to the European standard EN16207 [2], magnetic track brakes for mainline trains are assembled as rectangular brake frames. In a brake frame, the braking magnets are centred above the rail and linked by track rods. Figure 1.1 depicts a drawing of a magnetic track brake of a mainline train. In the brake frame shown, the track brake consists of four small magnets, two on each side. The rear and the front magnets are linked by connecting beams. Further main components of a track brake are the actuating cylinders, the mechanical stops and the centring devices.

Braking magnets of track brakes used for mainline applications are electromagnets as shown in Figure 1.2. When the brake is activated, the magnets come into contact with the rail, which creates a frictional force which is used for braking. As depicted, braking magnets consist of a coil body and an open ferromagnetic core which is then closed to a magnetic circuit by the rail.

The core of the magnet in the figure is subdivided into endpieces at both ends and three intermediate elements. The endpieces are rigidly connected to the coil body whereas the intermediate elements are designed moveable inside the coil body to compensate irregularities of the rail. The bottoms of the endpieces and the intermediate elements are

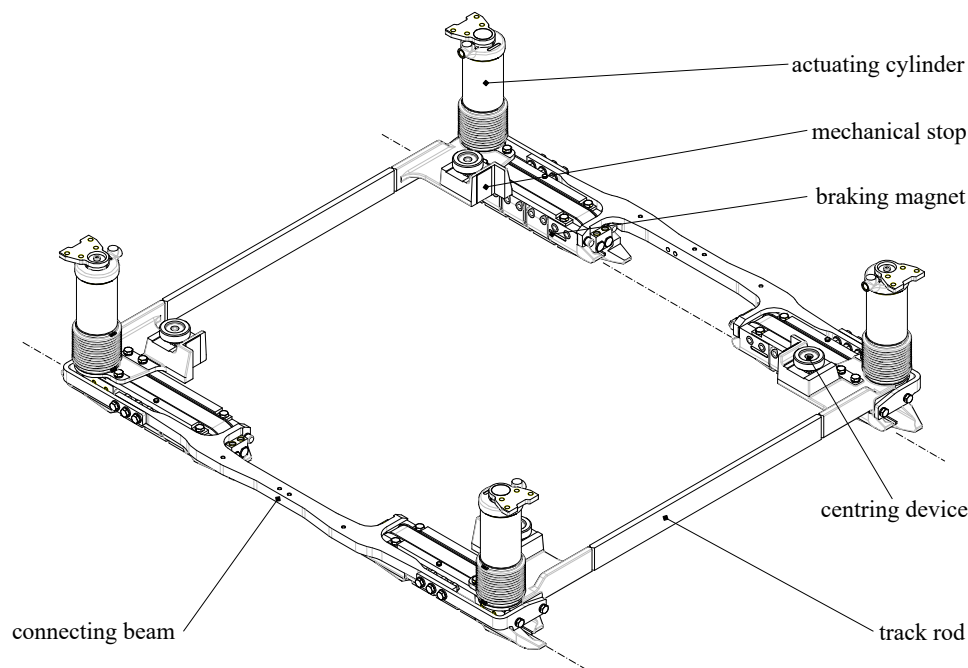


Figure 1.1: Electromagnetic track brake – overview

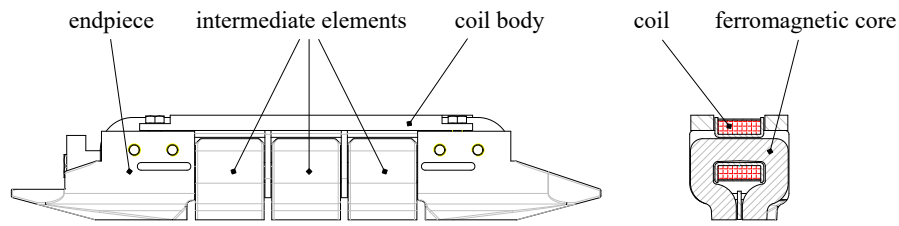


Figure 1.2: Braking magnet

referred to as pole shoes and are designed to slide on the rails. Pole shoes can be made from different materials including low carbon steel, spheroidal cast iron and sinter.

Mechanical stops transmit not only longitudinal forces but also lateral forces between the track brake and the bogie. Therefore, the stops are positioned in longitudinal and lateral directions. Longitudinal forces $F_{B,i,x}$ include brake forces as well as impact loads at the beginning of a braking manoeuvre. Lateral forces $F_{Q,i,y}$ may occur during braking manoeuvres on curved tracks and on crossings and switches. The mechanical stops are designed to have several millimetres of clearance between the brake and the bogie. As a result, the track brake can compensate small lateral movements of the train while staying centred on the rail.

Track rods are used to couple the movements of the magnets on both sides. This improves the travel of the magnets over crossings and switches. Track rods prevent magnets from a rolling motion about the longitudinal axis and keep the magnets at a constant lateral distance.

In most cases, track brakes only have two braking magnets. However, limited space in modern bogies sometimes requires longitudinally split magnets which must then be linked by **connecting beams**.

Actuating cylinders are single acting pneumatic cylinders with spring return. When the track brake is activated, the actuating cylinders lower the track brake from the ready position above the rail onto the rail. When deactivated, two compression springs inside the actuation cylinders pull the track brake against the bogie. Figure 1.3 shows an actuating cylinder. To compensate movements between the track brake and the rail, actuating cylinders have built-in spherical elastic joints on both sides.

Centring devices are used to fix the track brake against the bogie when the track brake is not active. They consist of a centring cone mounted on the brake frame and a form-fit centring ring on the bogie. The centring ring is spring-mounted with an elastomer torus to compensate deflections of the mounting points and mechanically decouple the brake frame from the bogie.

Magnetic track brakes work independently of the wheel-rail contact. The **function principle** of a magnetic track brake is based on friction between the rail and the braking

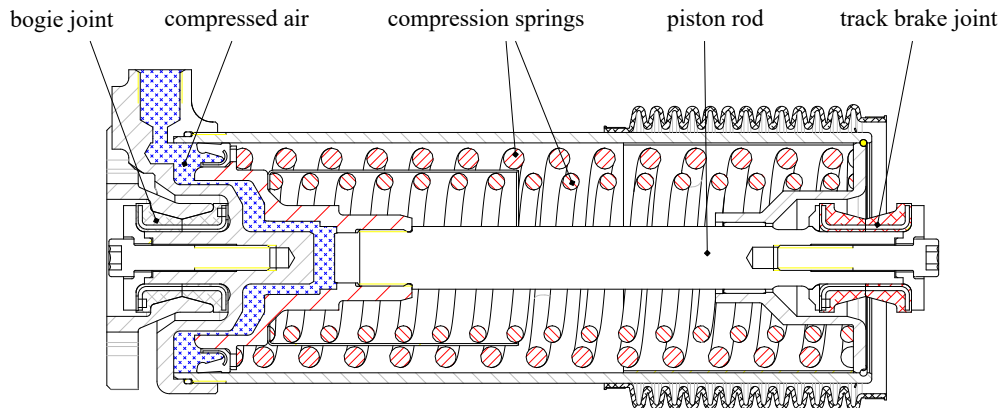


Figure 1.3: Actuating cylinder

magnets. This leads to wear of both the pole shoes and the rail. Therefore, magnetic track brakes are only used in emergency brake events but not in service brake applications.

To avoid disturbances of track-side signalling equipment, railway regulations [2] require track brakes to rest in a nominal distance of approximately 100 mm above the top of the rail when deactivated. Therefore, two operational conditions, the ready position and the braking position, must be distinguished.

In the **ready position** (see Figure 1.4), the track brake is fixed to the bogie as the actuation cylinders are depressurised and no voltage is applied to the electromagnets. Due to the prestressed springs inside the actuating cylinders, the cylinder force F_{cyl} pulls the track brake against the centring devices. As a result, the reaction forces of the centring devices F_{cd} occur. Because of the form-fit of the centring cone and the centring ring, the track brake is secured to the bogie. In the ready position, the track brake is mounted in a nominal distance above the rail of approximately 100 mm. However, this distance may change due to spring deflection of the primary suspension of the bogie and also wear of the wheels.

When **braking** (see Figure 1.5), the actuating cylinders are filled with compressed air. The pressure p_{cyl} increases up to a predefined steady state value. As a result, the track brake moves towards the rail and touches down onto the rail. Depending on the actual pressure and distance above the rail in the ready position, the brake frame is pressed to the rail by the actuation cylinder force F_{cyl} . As a result, the rail closes the magnetic cores of the brake magnets. Due to the applied voltage, a current i passes through the coils and excites the magnetic circuit. Thus, magnetic forces F_A between the rail and the pole shoes evolve. As the pole shoes of the magnets slide on the rails, friction forces $F_R = F_N \mu_G$ are generated. Here, μ_G is the coefficient of sliding friction and F_N is the actual normal force between the rail and the magnets and is calculated as the sum of

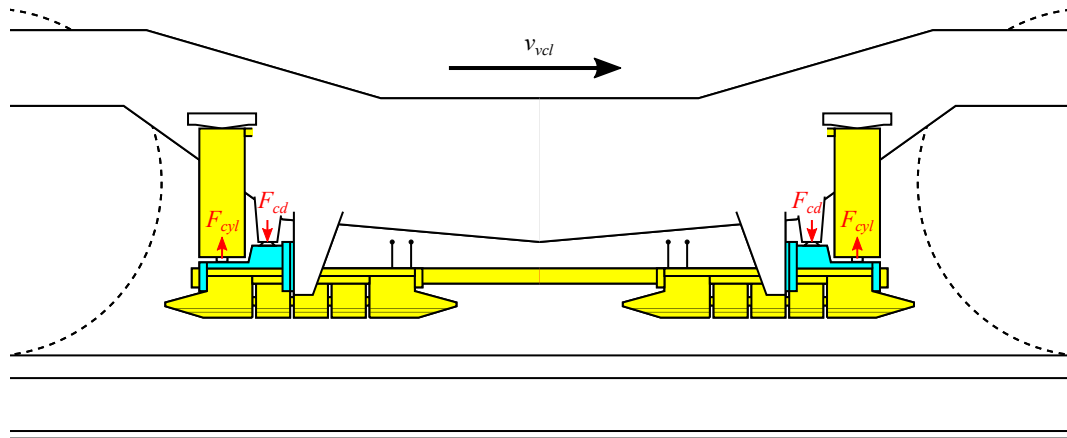


Figure 1.4: Track brake in ready position.

the actuation cylinder force, the vertical component of the magnetic attractive forces and the weight of the magnetic track brake (1.1). However, the weight $m_{MG}g$ and the cylinder forces F_{cyl} are usually small compared to the attractive forces $F_{A,z}$. Therefore, the weight and the actuation cylinder forces are often neglected.

$$F_N = \sum F_{cyl} + \sum F_{A,z} + m_{MG}g \quad (1.1)$$

Friction forces are then transmitted by the mechanical stops to the bogie. Between the track brake and the bogie, the brake force of the magnetic track brake $F_{B,x}$ evolves. When the track brake is deactivated, the source voltage is turned off. As a result, magnetic forces and brake forces decrease. The actuation cylinders are depressurised and the track brake moves back to the ready position.

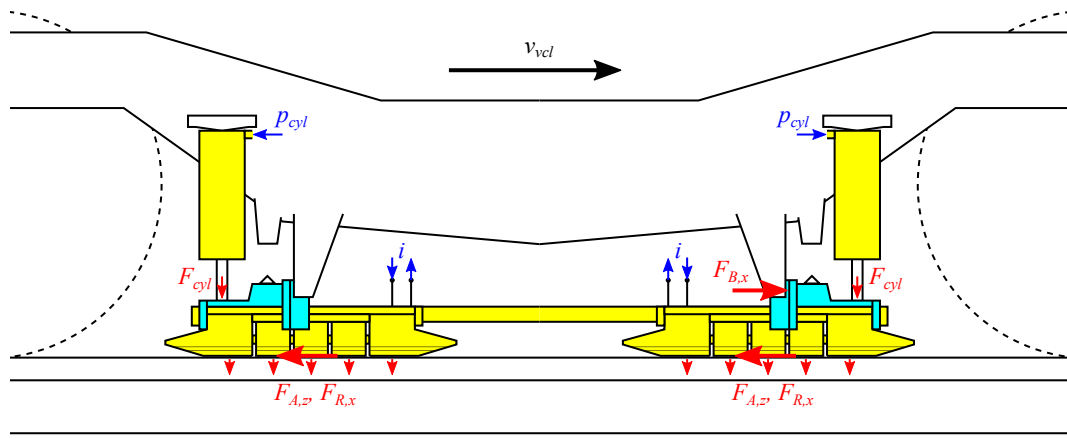


Figure 1.5: Track brake in braking position.

1.2 Known issues of magnetic track brakes

Despite their unquestioned capabilities as an emergency braking system, magnetic track brakes nowadays are not used as a primary service braking system. The sliding contact of the braking magnets on the rail obviously leads to undesirable wear. Subsequently, typical known issues of track brakes are described.

Increasing brake forces at low velocities The brake forces of magnetic track brakes increase with decreasing velocity with the steepest increase just before full stop of the vehicle. This is known from the literature on track brakes ([7], [8],[9], [10]), studies on braking performance ([4], [5], [6]), field tests and also passenger experience. Figure 1.6 shows a diagram of the brake force with respect to the vehicle velocity published by Hendrichs [9].

The reason for the increase of brake force is credited to a rising coefficient of friction. This coincides with results published from experiments on the velocity dependent sliding friction behaviour of metal-metal pairings ([11], [12]) which will be discussed later. Due to this behaviour, when the track brake is activated until full stop, resulting peaks in deceleration of the vehicle lead to uncomfortable stopping jerks, best known from emergency brakings of trams. Even though this behaviour is regarded acceptable in trams, magnetic track brakes in mainline trains are usually deactivated at approximately 25 km/h (or even 50 km/h [7]).

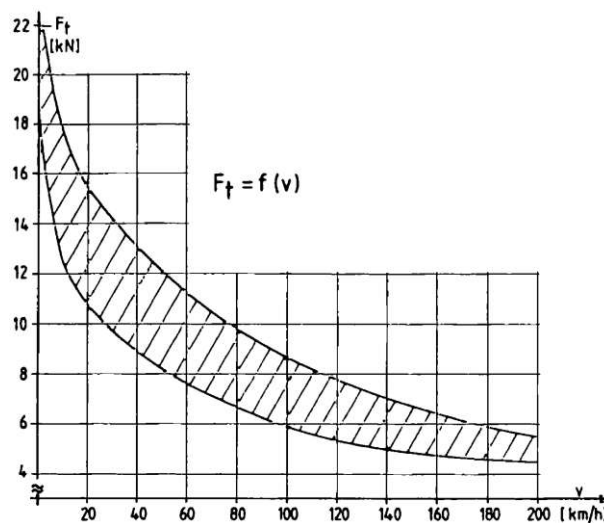


Figure 1.6: Brake force characteristics with respect to the vehicle velocity [9]

To avoid dangerous signal overruns in low adhesion conditions, nowadays an increasing number of operators demand the ability to use track brakes until (nearly) full stop of the vehicle. Therefore, future track brakes must be designed to operate in the low velocity range as well.

Accumulation of material on the pole shoes Especially when braking from high velocities, track brakes with steel pole shoes tend to accumulate material from the track. This material consists of dust and grease but also welded particles from the rail and is therefore referred to as pick-up weldings. Figure 1.7 shows an example of material adhering on the pole shoes. Pick-up weldings on steel pole shoes affect braking performance negatively as they increase the effective air-gap between the magnet and the rail. To restore brake forces, pick-up weldings must be removed periodically in maintenance.

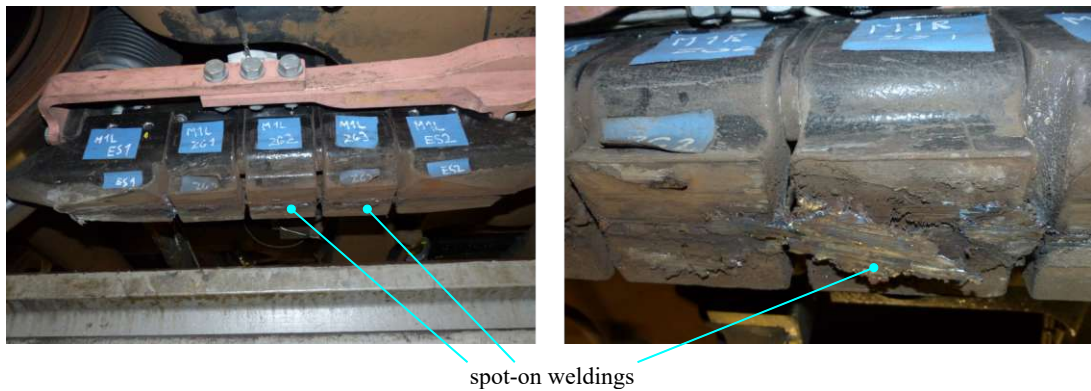


Figure 1.7: Pick-up weldings on pole shoes

Vibrations at low vehicle velocities New findings have shown that severe vibrations of the track brake may evolve when approaching velocities $v < 25$ km/h. The vibrations are characterised by oscillations of the interfacing forces $F_{B,x}$ between the track brake and the bogie as well as of the bending moments of the connector beams and track rods, Figure 1.8. As measurements did not show any excitation emanating from the vehicle in the relevant frequency band, vibrations are assumed to be of a self-excited type.

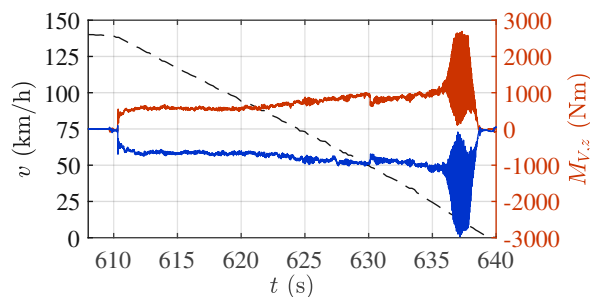


Figure 1.8: Measurements of vibrations at low velocity

1.3 Aims and objectives

Structural vibrations at low velocities lead to high mechanical loads which impede the use of the magnetic track brake until standstill of the vehicle. To maximise braking performance this thesis aims to understand and predict structural vibrations of a magnetic track brake and to prevent them in the future by appropriate methods. Assuming that the vibrations are self-excited, the mechanism behind is to be studied. Based on this hypothesis, the question is raised how the energy supplied to the system by external sources is transformed to maintain the vibrations. Since vibrations of magnetic track brakes are known to occur in only a limited number of designs, it can be assumed that there are design parameters that favour their occurrence. These parameters are to be identified with the aim to develop proposals for more favourable designs.

To address these problems, it is required in a first step to develop appropriate mathematical models of the magnetic track brake. Since magnetic track brakes are electro-magneto-mechanical systems and it is not clear which domains are relevant for the occurring vibrations, a mathematical model has to cover all three domains. The models should be suitable for investigating mechanisms in principle on the one hand and on the other hand offer a sufficient level of detail to allow for qualitative statements on the stability behaviour of the magnetic track brake. Measurement data from vehicle tests and laboratory tests are to be used to identify model parameters and to validate calculation results.

Using established methods of stability analysis of dynamical systems, the key parameters of influence are to be found within the scope of this thesis. Based on these parameters, methods are to be developed to avoid vibrations in future magnetic track brakes even at low speeds and thus improve the braking performance of trains.

1.4 State of the art and fundamentals

Although self-excited vibrations of magnetic track brakes are a yet unexplored phenomenon, it is possible to build on findings and established methods of various adjacent fields of research. This includes the stability theory of dynamical systems, which in particular offers methods for the analysis of self-excited systems. Further links exist to the fields of tribology of sliding steel bodies, braking systems for rail vehicles as well as to previous studies on magnetic track brakes. In this section, important sources of literature and basic assumptions are presented.

1.4.1 Stability analysis of dynamical systems

Stability analyses of technical systems focus on their behaviour near to an unperturbed state. In Leipholz's comprehensive introduction to stability theory [13], several definitions of stability are given. The stability concept of Lyapunov is widely referred to in assessing the stability of the solutions of dynamical systems. According to the definition, a stable system is able to remain within a defined region near to an initial state after small perturbations.

Mack and Plöchl [14] give an overview on the stability of motion including a summary of the concepts introduced in [13]. A system of n first order differential equations with the generalised coordinates q_i ($i = 1 \dots n$) and the parameters α_k ($i = 1 \dots m$) is described by its system equations

$$\dot{q}_i = F_i(q_1, q_2, \dots, q_n, \alpha_1, \alpha_2, \dots, \alpha_m, t). \quad (1.2)$$

The unperturbed state of (1.2) is given by the state variables q_i^0 and parameters α_k^0 . Let a perturbation of this state be given by the state variables q_i^s , the initial conditions be specified by $t = t_0$, $\varepsilon > 0$ and $\eta(\varepsilon) > 0$ be small positive numbers. The steady state of the system is *stable* if for each

$$|q_i^0(t_0) - q_i^s(t_0)| \leq \eta(\varepsilon) \quad (1.3)$$

condition (1.4) holds:

$$|q_i^0(t) - q_i^s(t)| \leq \varepsilon \quad \text{for } t > t_0 \quad (1.4)$$

Moreover, the state is *asymptotically stable*, if

$$|q_i^0(t) - q_i^s(t)| \rightarrow 0 \quad \text{for } t \rightarrow \infty. \quad (1.5)$$

Figure 1.9 shows an example from [14] of a system in a two dimensional Euclidean space. The example shows a steady state defined by $q_i^0 \equiv 0$. The three curves are

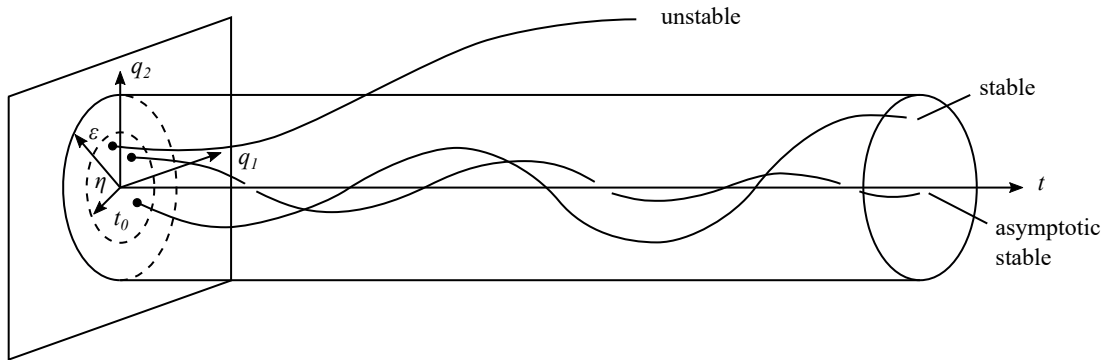


Figure 1.9: Trajectories of perturbed motion, reproduced from Mack and Plöchl [14]

trajectories starting at perturbed initial states showing unstable, stable and asymptotic stable behaviour.

For a linear autonomous system of equations $\dot{\mathbf{x}} = \mathbf{A}_{sys}\mathbf{x}$ of order n with the system matrix \mathbf{A}_{sys} and a state vector \mathbf{x} , the characteristic polynomial $p(\lambda)$ is given by Equation (1.6).

$$p(\lambda) = \det(\mathbf{A}_{sys} - \lambda\mathbf{I}) = \lambda^n + a_1\lambda^{n-1} + a_2\lambda^{n-2} + \dots + a_{n-1}\lambda + a_n \quad (1.6)$$

Here, a_i are the coefficients of the characteristic polynomial. The solutions of the characteristic polynomial λ are the *eigenvalues* of the system. The non-trivial solutions of the linear system of equations $\mathbf{x}(t)$ are *asymptotically stable* if all eigenvalues have negative real parts $\text{Re}(\lambda) < 0$. If one or more eigenvalues have positive real parts, the linear system is *unstable*. For a vanishing real part $\text{Re}(\lambda) = 0$, the stability limit is found for the linear system. However, for linearised systems, no stability statement is possible in this case.

Based on the coefficients of the characteristic polynomial, the Stodola criterion and the Hurwitz criterion describe necessary as well as necessary and sufficient conditions for asymptotic stability of linear systems, see e.g. Müller and Schiehlen [15].

Stodola criterion

A necessary condition for all eigenvalues to have negative real parts is that the coefficients of the characteristic polynomial (1.6) are positive, see Equation (1.7).

$$a_i > 0 \quad \text{for } i = 1 \dots n \quad (1.7)$$

Hurwitz criterion

The coefficients of the characteristic polynomial a_i are used to build the Hurwitz matrix \mathbf{H} :

$$\mathbf{H} = \begin{bmatrix} a_1 & 1 & 0 & \cdots & 0 \\ a_3 & a_2 & a_1 & \cdots & \vdots \\ a_5 & a_4 & a_3 & \cdots & \vdots \\ \vdots & \vdots & \vdots & \ddots & \vdots \\ 0 & \cdots & \cdots & \cdots & a_n \end{bmatrix} \quad (1.8)$$

A necessary and sufficient criterion for all eigenvalues to have negative real parts is that all main principal minors of \mathbf{H} are positive $H_i > 0$, with

$$H_1 = a_1, H_2 = \det \begin{bmatrix} a_1 & 1 \\ a_3 & a_2 \end{bmatrix}, \dots, H_n = \det \mathbf{H}. \quad (1.9)$$

Critical stability boundary

As stated by [15], the critical stability boundary of a linear system can be found as follows: Beginning within the region of asymptotic stability, the parameters of the system are varied until Equation (1.10) is satisfied.

$$H_n = a_n H_{n-1} = 0 \quad (1.10)$$

If $a_n = 0$, the monotone marginal stability is found. This means, that a pure real eigenvalue becomes zero $\lambda = 0$. If $H_{n-1} = 0$, the oscillatory marginal stability is found. As a result, the real parts of a pair of conjugate complex eigenvalues become zero $\lambda_{i,1,2} = \pm i\omega$ with $\omega > 0$.

Root locus and phase portraits

Phase portraits show state variable trajectories of solutions of differential equations in state space.

Figure 1.10 shows trajectories in the vicinity of an equilibrium state of a two dimensional linear system with a pair of conjugate complex eigenvalues $\lambda_{1,2} = \alpha \pm i\omega$. The left diagram shows a stable focus for $\alpha < 0$ with trajectories of periodic solutions $\mathbf{x}(t)$ converging towards the equilibrium state. The centre diagram shows an unstable focus for $\alpha > 0$ where small perturbations from the equilibrium states lead to diverging (periodic) solutions. For $\alpha = 0$, periodic solutions are obtained with closed trajectories around the equilibrium.

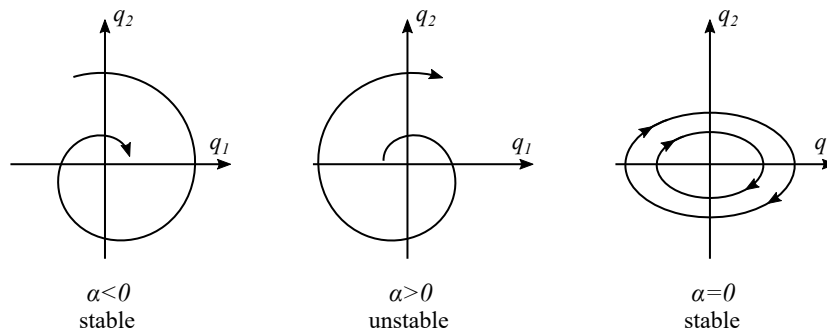


Figure 1.10: stable/unstable focus in phase space, reproduced from [13]

In the case of a non-linear system linearised at a steady state, it must be noted that the phase portraits of the linearised system only represent the system behaviour in a vicinity around the linearisation point. Outside this vicinity, due to non-linear effects, both the solutions and thus also the phase portraits of the linearised system can differ greatly from those of the original system. The linearised system cannot characterise the behaviour of a system after the loss of stability. In the case of non-linear systems, the occurrence of limit cycles is an important special case where solutions near to an unstable focal point converge to a stable (limited) periodic solution [13].

Hopf bifurcation

Figure 1.11 shows a pure real negative eigenvalue $\lambda_k = \alpha_k$ and a pair of conjugate complex eigenvalues $\lambda_{i,i+1} = \alpha_i \pm i\omega_i$ in the complex plane. When analysing eigenvalues with respect to a system parameter ν , a *Hopf bifurcation* point is found as a pair of conjugate complex eigenvalues crosses the imaginary axis. Kuznetsov [16] states that a bifurcation represents a structural change in system behaviour, such as the birth/death of an equilibrium or a switch from stable to unstable behaviour.

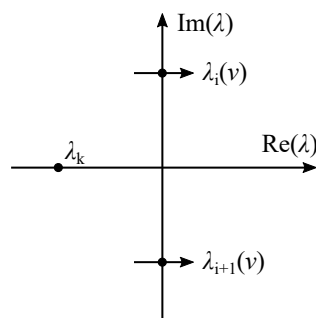


Figure 1.11: Root locus of eigenvalues in the complex plane

As described in [17], "A Hopf bifurcation is the transformation of a focus-type equilibrium

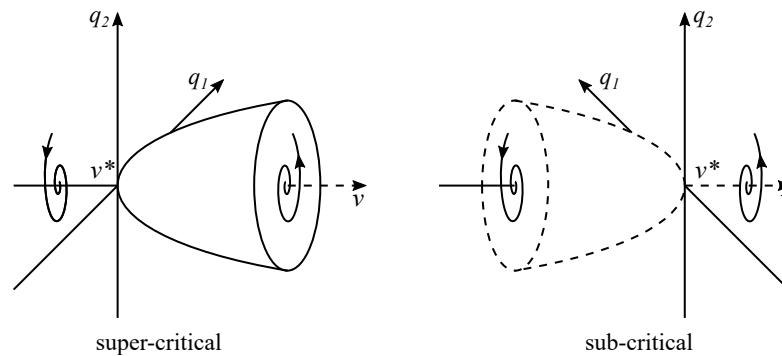


Figure 1.12: Hopf-bifurcation, reproduced from [17]

into a limit cycle". Figure 1.12 shows the phase portraits of the two types of *Hopf bifurcations* with respect to the system parameter ν . The diagram on the left side shows the *super-critical* case. For $\nu < \nu^*$, a stable focus point exists. When increasing ν , the stable focus gets unstable and solutions converge to a stable limit cycle. The right diagram on the other hand shows the *sub-critical* case with an unstable limit cycle with diverging trajectories. For $\nu < \nu^*$, trajectories inside the limit cycle converge to the equilibrium point which defines the *basin of attraction*. When increasing ν , an unstable focus point is born – the bifurcation is catastrophic with infinitely increasing amplitudes.

1.4.2 Types of self-excited vibrations

Self-excited vibrations are wide-spread phenomena in technical, physical, economic but also biological systems [18]. Self-excited vibrations may include cross-domain phenomena such as aero-elastic or fluid-structure interactions. Even though often desired as in bowed string musical instruments, self-excited vibrations are most often unwanted in technical systems. Well-known examples of self-excited vibrations in technical systems are squealing disc brakes and railway wheels in curves, chattering wiper blades and clutches, and roaring rails. Paniccioli and Serge[18] give an overview on many further examples. Mechanisms leading to self-excited vibrations are manifold. They include friction vibrations, occurrence of non-conservative follower loads, mode coupling and coupled vibrations. However, all types of self-excited vibrations have the existence of an external energy source in common that provides the energy to generate and maintain oscillations despite the obligatory damping effects [19]. Moreover, a mechanism is needed that can transfer energy from the external source to the oscillating system. Subsequently, a few types of self excited vibrations are introduced.

Friction-induced self-excited vibrations

Systems with friction-induced self-excited vibrations are systems where the self-excitation mechanism results from a negative friction gradient with respect to the sliding velocity.

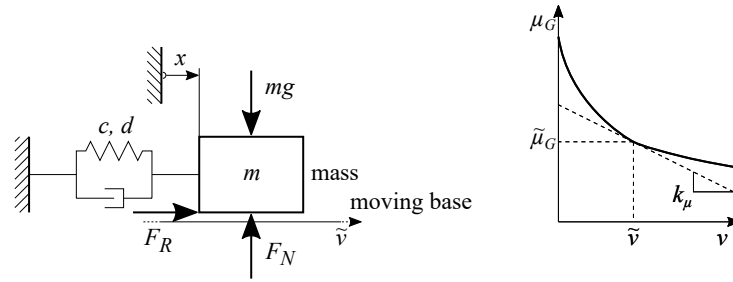


Figure 1.13: Simple friction oscillator, adapted from [20]

With such systems, it is typical for one single oscillation mode to become unstable. Such systems are described, for example, by Popp [20], Chen [21], Ibrahim [22] and others.

Figure 1.13 shows a typical example of friction-induced vibrations. A mass m supported by a spring-damper (c and d) slides on a belt with a constant conveying velocity \tilde{v} .

The sliding friction coefficient is velocity dependent with typically decreasing characteristics for increasing velocities – see Figure 1.13 on the right. In the linear(-ised) case, the sliding friction coefficient is given by $\mu_G(v) = \tilde{\mu}_G + k_\mu v$, where k_μ is the gradient with respect to the relative sliding velocity. The equation of motion of the system is given by:

$$m\ddot{x} + \underbrace{(d + k_\mu)}_{\text{damping term}} \dot{x} + cx = mg\tilde{\mu}_G \quad (1.11)$$

The system becomes unstable when the velocity dependent damping term in (1.11) becomes negative. This is the case when the (negative) gradient k_μ exceeds the internal damping d of the system (1.12).

$$-k_\mu > d \quad (1.12)$$

Mode-coupling induced vibrations

As stated by Hoffmann and Gaul [19], the coupling of two vibrational modes is another well-known mechanism leading to oscillatory unstable systems. With this type of self-excited vibrations typically two modes merge together and form a pair consisting of a stable and an unstable mode. To study this type of self-excited vibrations, Hoffmann et al. [23] use an expanded belt-conveyor model as seen in Figure 1.14. The model has two degrees of freedom x and y and also two deflection modes. In contrast to the model shown in Figure 1.13, the present model uses a constant friction coefficient μ .

Results show that the friction force F_F acts as a cross-coupling link between the vertical and the horizontal deflections. It is further shown that the coefficient of friction μ can be used to control the eigenvalues. In Figure 1.15 Hoffmann et al. [23] show the ratio

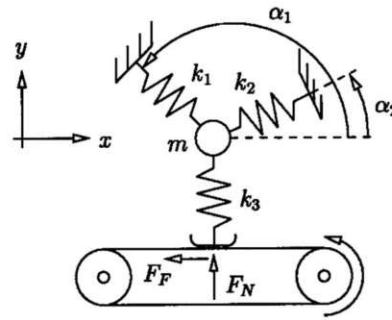


Figure 1.14: Model for analysing the mode-coupling mechanism, Hoffmann et al. [23]

of the occurring natural frequencies $\frac{\omega_2}{\omega_1}$ and their "growth rate" D with respect to the coefficient of friction μ .

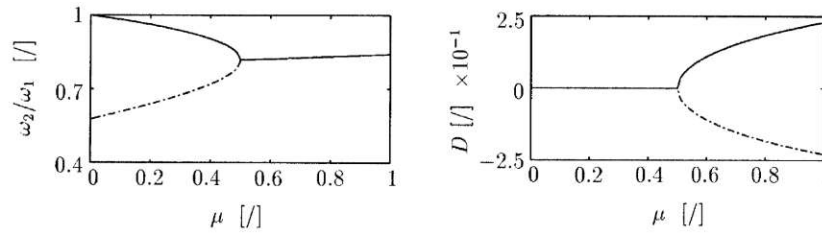


Figure 1.15: Results from Hoffmann et al. show the merging of natural frequencies in the mode-coupling mechanism [23]

For small values of μ , there are two separate natural frequencies, both with a growth rate of zero. For high values of μ however, the frequencies of the two modes merge into a pair of an unstable and a stable mode.

Inertial self-excitation

Babitsky and Landa [24] describe a class of dynamical systems where self-excitation may occur due to the inertial coupling between the variables. In their study, linearised systems consisting of a second order and a first order coupled differential equation of the form (1.13)-(1.14) are analysed.

$$\ddot{x} + 2\delta\dot{x} + \omega_0^2 x = -ky \quad (1.13)$$

$$\dot{y} + \gamma y = ax + c\dot{x} \quad (1.14)$$

By applying the Hurwitz criterion to (1.13)-(1.14), criteria for oscillatory stability (1.15) and monotone stability (1.16) are obtained:

$$0 < 2\delta(\omega_0^2 + 2\delta\gamma + \gamma^2) - k[a - c(2\delta + \gamma)] \quad (1.15)$$

$$0 < ak + \omega_0^2\gamma \quad (1.16)$$

For a set of suitable parameters, the system (1.13)-(1.14) may become oscillatory unstable.

1.4.3 Instantaneous and equivalent brake force

The braking performance of railway vehicles is assessed on the basis of measured braking decelerations [25]. The technical literature distinguishes between instantaneous and equivalent decelerations. Instantaneous decelerations a_{vcl} represent actual decelerations, equivalent decelerations $a_{vcl,eq}$ are a theoretical calculated value based on an assumed uniformly decelerated motion. Following this definition, instantaneous brake forces $F_{B,x}$ and equivalent brake forces $F_{B,x,eq}$ are derived. The equivalent force is derived through (1.17) to (1.19).

$$P_{B,x}(t) = F_{B,x}(t)v_{vcl}(t) \quad (1.17)$$

$$W_{B,x} = \int_{t_{10}}^{t_{20}} P_{B,x}(t)dt \quad (1.18)$$

$$F_{B,x,eq} = \frac{W_{B,x}}{\int_{t_{10}}^{t_{20}} v_{vcl}(t)dt} \quad (1.19)$$

Here, $P_{B,x}$ is the power of the brake force, $W_{B,x}$ the mechanical work evaluated over the time of brake application $t_{20} - t_{10}$ and $v_{vcl}(t)$ the vehicle velocity.

1.4.4 Velocity dependent coefficient of friction

As stated in Section 1.2, increasing brake forces of magnetic track brakes at low velocities is a well-known phenomenon. The main reason for this behaviour is the rising sliding friction coefficient with decreasing velocity. Assuming a (relatively) constant magnetic attraction force $F_{A,z}$ between the magnet and the rail, this implies a negative friction gradient $\frac{\partial \mu_G}{\partial v_{vcl}} < 0$ with respect to the sliding velocity which may be a source of friction-induced self-excited vibrations. To study possible self-excitation mechanisms of a magnetic track brake, realistic friction characteristics are mandatory.

The materials of the friction partners of a track braking system are usually mild steel S235 on the part of the pole shoes and hardened rail steel according to EN 13674-1 [26] such as R260 and R350. For such material pairings considerable velocity dependent sliding friction characteristics are found in different fields of engineering.

In the literature, general and application-based studies on friction characteristics of steel-steel pairings, such as Montgomery's pin-on-disc experiments [11] and the pad-on-disc experiments of Desplanques et al. [12] are found. The studies focus on experimental or analytical estimation of the friction coefficient under laboratory conditions of one rotating and one fixed contact partner. In a rotating system, surface conditioning effects due to repeated overtravel may occur. Due to the linear motion of the track brake over the rail, such effects do not exist in practice. Therefore, it appears inconsistent to use friction coefficient characteristics originating from tribometer tests.

In addition, there are numerous theoretical studies on the representation of friction at low and high sliding speeds. Olsson et al. [27] gives an overview of dynamical and static models close to static friction for dry and lubricated contacts. Here, special focus is put on effects that are relevant in the transition between static and sliding friction. One representative example for high sliding speeds is described by Ettles [28], in which the coefficient of friction depends on the local temperature in the friction contact. For many of the models however, it appears unfeasible to determine the necessary parameters for the case of the magnetic track brake and the rail. Hale et al. [29] investigate phenomenologically the velocity-dependent friction and wear between rails and sliding pads on a linear high-speed testing facility for (very high) velocities in the range of 0-1530 m/s. With increasing contact forces and speeds, decreasing friction values between the steel contact partners are measured, which are by a factor > 2 higher than the brake force coefficients of the magnetic track brake, see below.

A lot of effort has been made on analysing the wheel-rail contact parameters. Lewis and Olofsson [30] give an overview on the friction characteristics in the wheel-rail contact point, Godet [31] of the well-established third body layer model. It is assumed that railheads are contaminated by materials such as grease and brake dust or foliage, which act as an additional contact partner and therefore influence the friction parameters. These influences may be intensified by environmental conditions. It can be assumed that the sliding friction coefficient of a track brake on the rail surface may be influenced similarly. Friction characteristics in the wheel-rail context are often described as creep-friction or slip-coefficient of traction curves. Well established calculation methods for the contact area as well as contact tangential forces with respect to the wheel creep include Kalker's CONTACT [32] and FASTSIM [33] as well as Polach's algorithm [34]. Based on conclusions drawn from measurement data, Zhang et al [35] and Polach [36] propose modifications to the models to include a friction coefficient reduction factor for increasing friction velocity. Available published measurement data includes results from vehicle tests by Logston and Itami [37] as well as from laboratory experiments by Fletcher and Lewis [38]. Figure 1.16 shows typical characteristics of the friction coefficient in longitudinal direction f_x for wet and dry conditions with maximum values between 3-10 %. For higher slip values, the coefficient of traction decreases, which implies a negative friction gradient [36].

Negative friction gradients are associated with self-excited vibrations of wheelsets [39]. It has been shown that due to different friction characteristics, environmental conditions and lubrication have an impact on the occurrence of self-excited vibrations of wheelsets.

However, studies on the wheel-rail contact focus on a primarily rolling motion of the wheel over the rail. High slip or creep leads to wear on both wheel and rail. Wheel slide protection for both, traction and braking prevents high relative velocity in the contact point between wheel and rail. As a result, relevant creep values found in the literature are usually smaller than 10 %. This contrasts to the pure sliding motion of a track brake on the rail. Although the wheel-rail contact problems have many similarities to the track brake-rail contact, creep-friction curves from the literature cannot be used for this study.

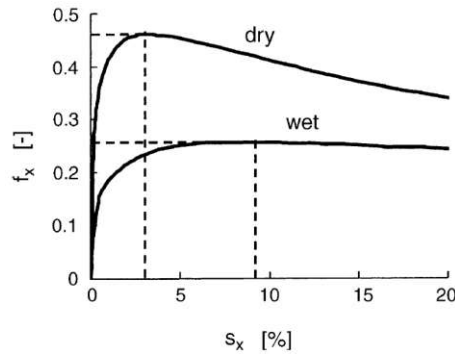


Figure 1.16: Friction of the wheel-rail contact [36]

Lastly, in the literature on magnetic track brakes ([7], [8], [40], [41], [42], [4], [5], [43], [44], [6]) the brake force $F_{B,x}(v)$ is defined as:

$$F_{B,x}(v) = F_A f_{MG}(v) \quad (1.20)$$

Here, F_A is the magnetic attractive force and $f_{MG}(v)$ the brake force coefficient. Figure 1.17 shows the brake force coefficient with respect to the velocity according to a study conducted by the European Rail Research Institute [6]. The data shows a steep increase of brake force when approaching low velocities. Similar characteristics are found in the paper from Jirout et al. [40], Cruceanu et al. [42] and also in the technical descriptions of track brakes by Gfatter et al. [7].

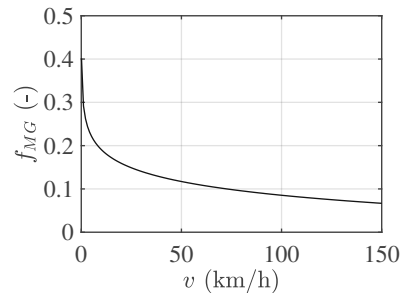


Figure 1.17: Coefficient of brake force according to data from [6]

The characteristics found for magnetic track brakes, however, are to be understood as coefficients of brake force rather than coefficients of friction. Coefficients of brake force $f_{MG}(v)$ are used to predict the braking performance of railway vehicles in service, considering an average value of contamination on both rail and pole shoes of the track brake. The nominal attractive force is a test-bench value according to [2] and [3]. According to the standard, the attractive force is measured under ideal conditions on a machined rail with a flat surface and therefore represents a theoretical maximum value of the magnet. During braking, the area of contact between the track brake and the rail is

most likely not ideal due to the curved railhead on the one side and pick-up weldings on the other. The actual attractive force during braking will most likely be lower than the nominal value. As a result, the actual friction coefficient μ_G will most often be higher than the brake force coefficient f_{MG} .

None of the friction characteristics available in the literature appears to be suitable for the purposes of this thesis. Therefore, velocity-dependent friction characteristics for the magnetic track brake are determined in vehicle tests within the scope of this thesis.

1.4.5 Mathematical modelling of electromagnets and magnetic track brakes

Kallenbach et al. [45] give a comprehensive introduction to the mathematical characterisation of electromagnets. Magnetostatic and dynamical problems are described and guidelines for modelling are provided. This includes a comparison of state-of-the-art modelling techniques such as the network method and the finite element method.

Darula and Sorokin [46] give an overview of modelling methods of electro-magneto-mechanical actuators in general. They focus on the electrical part by comparing circuits with and without capacitors. System models with 2 or 1.5 degrees of freedom are derived which are used to analyse the transfer function in the frequency domain.

Jirout et al. [40] use an electro-magneto-mechanical model to simulate a track brake as seen in Figure 1.18. The study addresses the simulation of impact forces between the magnetic track brake and the bogie at the beginning of a braking manoeuvre, considering the electromagnetic attraction process. The electric part of the model consists of a voltage source and a coil, which is represented by an electrical resistance and an inductance. The magnetic circuit is modelled by a ferromagnetic rail as well as a magnetic core and an air-gap. The magnetic track brake is accelerated against a spring force by the resulting magnetic force in vertical direction to the track. The frictional forces between the rail and the brake magnet caused by normal forces lead to a deceleration of the magnet. By applying a friction model that takes into account a transient progression of the friction coefficient, impact forces between the bogie and the magnetic track brake are determined that are qualitatively comparable with vehicle test data.

Döbrössy [41] builds on the electro-magneto-mechanical model for track brakes in low-suspension from [40] and develops it further to include a look-up table for magnetic forces from a previous magnetostatic finite element calculation. In the thesis, different combinations of brake magnets and spring suspensions are simulated and the results are validated with laboratory tests. The results show a strong dependence of the reaction time of the magnetic track brake on the operating current and the size of the air-gap.

Using a multibody dynamics model of a magnetic track brake for mainline trains, Jirout analyses in [8] structural dynamical phenomena occurring during mechanical testing. Fatigue endurance tests as well as FMEA (failure mode and effects analysis) load cases are simulated and compared with laboratory tests. Furthermore, the structural dynamical

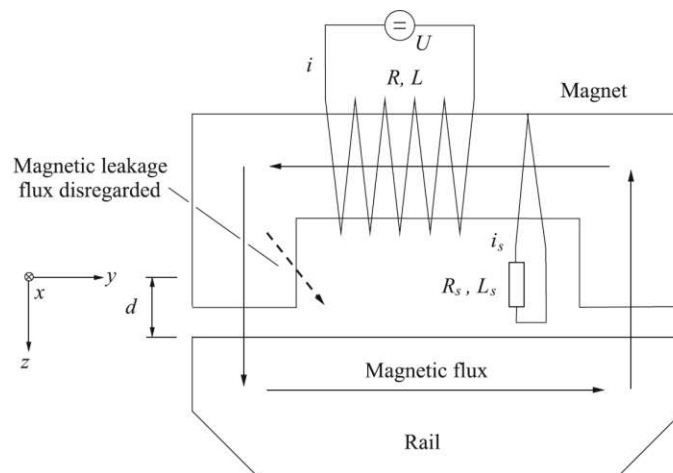


Figure 1.18: Electro-magneto-mechanical model of a track brake from [40]

model is used to simulate braking manoeuvres assuming a Hertzian contact between pole shoes and rail as well as static magnetic forces.

The dynamics of the track brake in the ready position is further studied by Tippelt [47]. Based on findings from [8], a parametric multibody dynamics model is used to simulate a vibration test in the standby position according to the vibration standard EN61373 [48]. In particular, the modelling of the centring device between the magnetic rail brake and the bogie is considered. Simulations with the model show limitations of excess amplification factors used in long-life tests.

Pötscher [49] measures nonlinear magnetic properties of various rail steel grades for varying temperatures. Magnetic B - H characteristics are obtained, where B and H represent the magnetic flux density and the magnetic field strength. Numerical analyses further investigate the influence of temperature and steel quality on the magnetic attraction force. The ferromagnetic permeability of the investigated materials decreases with increasing temperature. Finite element models of the magnetic track brake are used to validate measurement results of a test rig for measurement of magnetic forces, Figure 1.19. Pötscher discusses the influence of an air-gap between the rail and the magnet on magnetic attraction forces.

Galardi et al. [44] compare the dynamical activation process of an electromagnetic track brake simulated by a network model and by application of the finite element method. After calibration of the network model, the results show good agreement. Furthermore, magnetostatic calculations of attraction forces are validated using a test rig similar to the one described in [49].

Lu et al. [43] develop a detailed network model of the track brake by taking into account fillet radii of the rail head. Considering non-linear B - H characteristics, magnetic forces calculated with the network model show good agreement with finite element results.

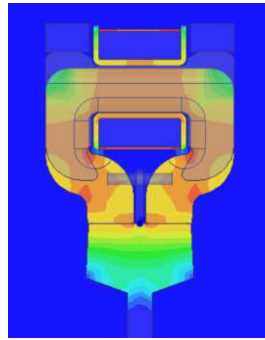


Figure 1.19: Magnetic flux density in a cross section of the track brake [49]

Tippelt et al. published in [50] and [51] first results on self-excited vibrations of a magnetic track brake, which are part of this thesis.

1.5 Outline of this thesis

The starting point of this thesis are vehicle tests and laboratory tests with the aim of studying the vibrations of the magnetic track brake, Chapter 2. Vibrations are measured in an asymmetric deflection mode with a magnetic track brake applied with strain gauges, force and current sensors and analysed using statistical methods. With experimental and finite element modal analyses, eigenfrequencies and eigenmodes of the structure are evaluated. Further data for determining velocity-dependent friction characteristics are acquired from driving tests.

Chapter 3 deals with the modelling of a magnetic track brake in the mechanical, magnetic and electrical domains. The modelling pursues two goals: On the one hand, simplified analytical models are to be created with which self-excitation mechanisms can be intuitively explored. On the other hand, models are to be created that are capable of qualitatively comparable results with driving tests.

Chapter 4 aims to identify and understand self-excitation mechanisms using simple electro-magneto-mechanical models. Established methods of linear stability analysis are applied to determine the influence of individual model parameters on stability criteria. Furthermore, the chapter aims to reveal energy sources that maintain vibrations of the magnetic track brake by analysing limit cycles.

By analysing the more complex multibody dynamics model, Chapter 5 focuses on the influence of magnet-rail contact conditions and vehicle velocity on stability. In addition, the comparability of simulation results with measurements from vehicle tests is examined.

Chapter 6 shows how changes in mechanical and electrical design may improve the stability behaviour of magnetic track brakes. Based on findings of the previous chapters, design recommendations are developed to increase brake performance and mitigate or eliminate self-excited vibrations.

Vehicle and laboratory tests

To learn more about the phenomenon of vibrations of the magnetic track brake at low velocities, vehicle (field-) tests and laboratory tests are performed and described in this chapter. First, the measurement object and the quantities measured in the tests are described. Then, vehicle tests on self-excited vibrations are presented including original measurement data. These tests are the starting point of this study. Measurements of selected braking tests performed during these vehicle tests are discussed to analyse the vibrations of the magnetic track brake. Experimental and finite element modal analyses complement the field test to extract the data required for the simulation models described in Chapters 4 and 5. Data of another vehicle test is presented which focuses on the measurement of the sliding friction coefficient between the pole shoes and the rail. The outcome of this test are velocity dependent friction characteristics for different environmental conditions. These characteristics are essential for the simulation models.

2.1 Measurement object and measured quantities

The laboratory experiments and field tests were conducted using a magnetic track brake equipped with sensors to observe the state of the brake. Figure 2.1 shows the electromagnetic track brake used for the field and laboratory experiments with all measurement points applied. For the field tests, the track brake is installed in a bogie of an electrical multiple unit (EMU) train. The measuring cables are routed from the sensors to the inside of the carbody to the data acquisition system. The sensors measuring the quantities s_{vcl} , v_{vcl} and a_{vcl} are located inside the carbody.

All sensors as well as the measurement chain are described in appendix, Table A.1 and Figure A.1. The measured quantities are grouped as followed:

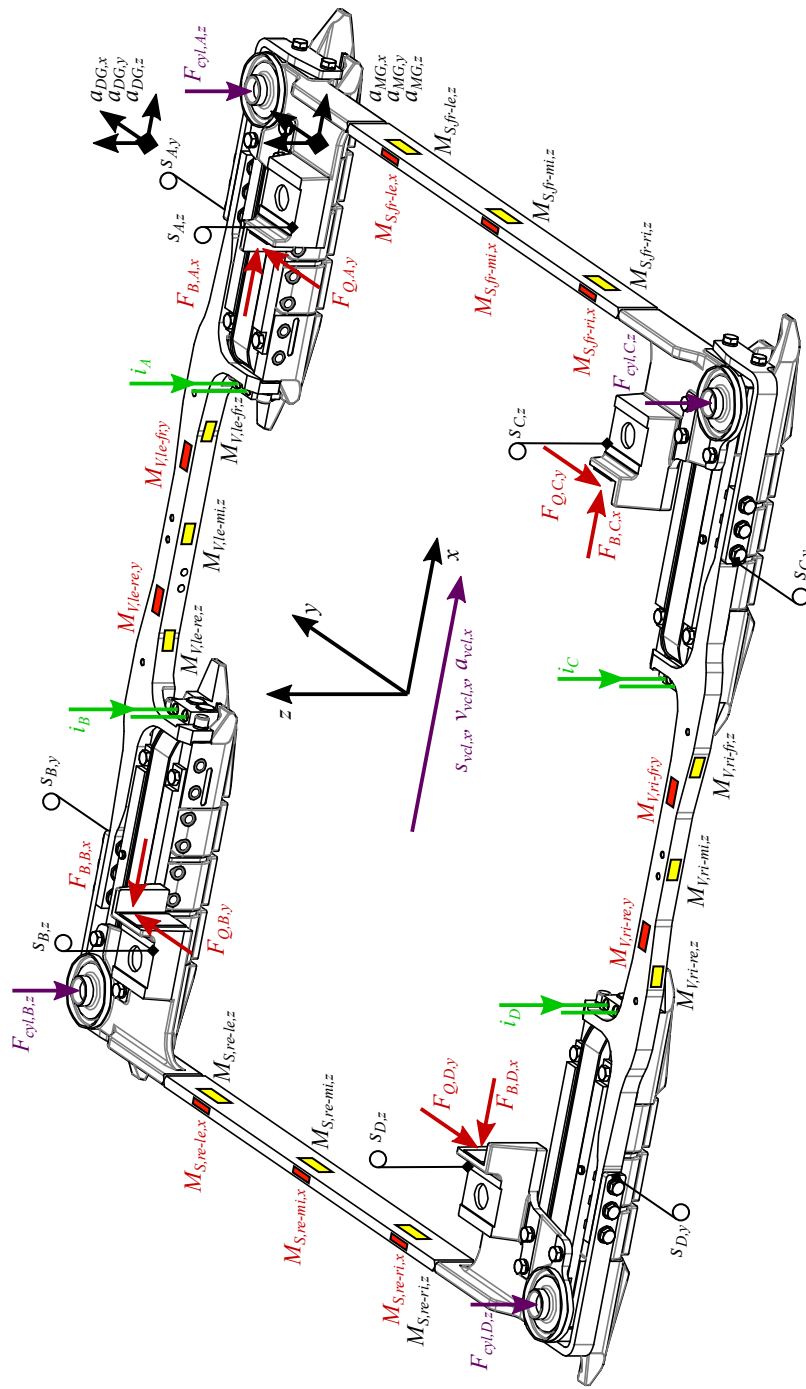


Figure 2.1: Measured quantities of the magnetic track brake

- Transmitting forces $F_{B,i,x}$ and $F_{Q,i,y}$ (field tests only):
The force transducers installed inside the mechanical stops measure longitudinal and lateral forces between the bogie and the track brake. Signals of longitudinal forces $F_{B,i,x}$ are intended, on the one hand, for direct measurement of the brake force of the track brake and, on the other hand, for measurement of dynamical forces such as impact loads during the brake activation process and loads induced by vibrations. $F_{Q,i,y}$ may be used for measurement of lateral forces during passage of crossings and switches.
- Bending moments of the longitudinal connectors $M_{V,i,y}$, $M_{V,i,z}$ and the track rods $M_{S,i,x}$ and $M_{S,i,z}$:
Using strain gauges, bending strains are measured in several positions as seen in Figure 2.1. Before the assembly of the track brake, signals of the bending strains are referenced to signals of defined bending moments. Positions of the strain gauges are chosen that various deflection modes of the track brake frame can be distinguished from their signals. Strain gauges are applied to measure bending moments in two directions of the beams. These are the y and z direction for the longitudinal connectors, further x and z for the track rods.
- Electrical current i :
Clamp-on current transducers are applied to the electric power cables of each magnet. As a result, the electrical activation process can be analysed in detail.
- Displacement with respect to the bogie $s_{i,y}$ and $s_{i,z}$:
Lateral and vertical displacements of the magnets with respect to the position of the bogie are measured using string potentiometers.
- Actuation cylinder forces $F_{cyl,i,z}$:
Forces produced by the pre-stressed actuation cylinders are measured indirectly by measurement of the pressure inside the piston chamber p_{cyl} and the vertical displacements $s_{i,z}$ of the track brake with respect to the bogie.
- Stopping distance s_{vcl} , velocity v_{vcl} , and deceleration a_{vcl} of the vehicle:
These signals are measured directly on the vehicle using an accelerometer and a speed-over-ground sensor. The quantities are cross-referenced by a GPS receiver.
- Accelerations of the bogie $a_{DG,i}$ and the track brake $a_{MG,i}$:
Using accelerometers, vibrations occurring on the bogie and the track brake are measured. These include vibrations during braking but also impact-accelerations during the brake activation process.

2.2 Field tests on self-excited vibrations

Field tests are conducted on an actual railway line under operational conditions. The trainset used in the tests is a four-car EMU with conventional motor bogies (MB1, MB5) at both ends, 2 Jacobs motor bogies (JMB2, JMB4), and a Jacobs trailer bogie (JTB3) between the two centre cars, Figure 2.2.

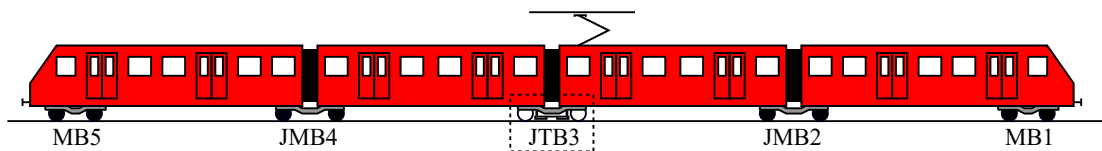


Figure 2.2: Configuration of the train

The magnetic track brake is installed in JTB3, Figure 2.3. The positions of the measuring points in the right connector are marked. In these tests, emergency brake activations are conducted in the $R+MG$ braking mode. This means that all available braking systems of the train including the magnetic track brake are active. Tests are performed with different initial velocities in the range of $v_{vcl,0} \approx 25-100$ km/h and until full stop. The track brake is active from the beginning of the braking manoeuvre. When the vehicle velocity v_{vcl} falls below 10 km/h, the track brake is deactivated automatically. Braking tests are performed in varying environmental conditions and several railway lines over straight and curved tracks as well as over switches and crossings.

In total, over a period of three days, 132 braking manoeuvres with the magnetic track brake are performed. In approximately 1/10 of the brakings, severe vibrations occur.

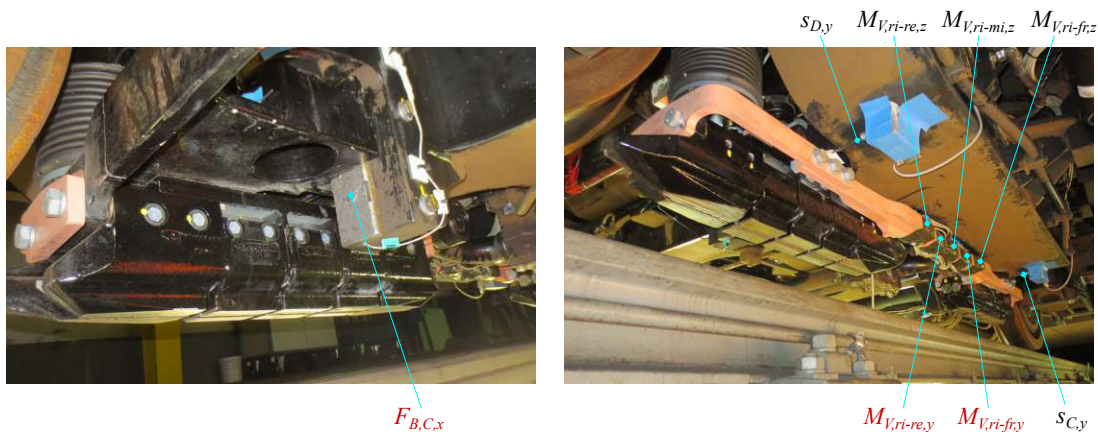


Figure 2.3: Track brake during the field test

Analysis of the measured signals

An example of a typical time history of a braking manoeuvre is discussed thoroughly, Figure 2.4. In this manoeuvre, the direction of motion of the train is in negative x direction. The *rear* side of the track brake is therefore leading in the direction of motion, Figure 2.1. In Diagram (a), the velocity v_{vcl} shows the deceleration of the vehicle from an initial velocity of roughly 80 km/h until full stop. Further, the signal of the linear transducer $s_{A,z}$ shows the vertical movement of the track brake. At the beginning of the record, $s_{A,z}$ is zero as the track brake is in its ready position fixed towards the bogie by the actuation cylinders and the centring devices. After brake activation, the brake frame travels 0.1 m onto the rail. During braking, the signal is nearly constant. Finally, the brake frame returns back to its ready position and the signal to 0.0 m.

Diagram (b) depicts signals of the pressure of the actuation cylinders p_{cyl} and the electric current i_{AD} . At the beginning of the record, the pressure rises until 6.8 bar and is then constant until deactivation. Kinks in the signal show the moments in time when the track brake lifts off the bogie and touches down onto the rail. In these tests, the electromagnets are activated with a delay with respect to the pressurization of the cylinders. Therefore, the signal of the current begins to rise after the touch-down. Also note the build-up time of the current due to the inductance of the electromagnets. After the delay and build-up times, the signal of the current is nearly constant at approximately 10.2 A. The moment of track brake deactivation at $v_{vcl} \approx 10$ km/h is clearly marked by a drop of i_{AD} and a kink in the signal of p_{cyl} .

Diagram (c) shows the transmitting forces between the track brake and the bogie $F_{B,B,x}$ and $F_{B,D,x}$ (at the rear side). After a build-up time, the transmitting forces increase during braking with decreasing velocity and increasing sliding friction coefficient μ_G . Until the recorded time index $t \approx 2405.5$ s the brake forces show the expected behaviour with only minor disturbances. At the end of the braking manoeuvre, vibrations with high amplitudes evolve at a frequency of roughly 28 Hz. These vibrations continue until the deactivation of the track brake.

The measured bending moments of the left and right connector beams with respect to the vertical axis ($M_{V,le-re,z}$, $M_{V,le-mi,z}$, $M_{V,le-fr,z}$, $M_{V,ri-re,z}$, $M_{V,ri-mi,z}$ and $M_{V,ri-fr,z}$) can be seen in Figure 2.4 (d). The bending moments result from a lateral offset between the lines of action of the friction forces $\mu_G F_{A,z}$ and the transmitting forces $F_{B,i,x}$. The left and the right sides are shown with opposed signs to underline the symmetrical behaviour of the left and right sides. The bending moments increase roughly linearly with the transmitting forces. Interestingly, on both sides there is a gradient from the front measuring points ($M_{V,le-fr,z}$, $M_{V,ri-fr,z}$) to the rear ($M_{V,le-re,z}$, $M_{V,ri-re,z}$) with the highest amplitudes in the leading measurement points (note the direction of motion in negative x direction). The vibrations can also be seen very clearly in these signals.

Diagram (e) depicts the bending moments of the front and rear track rods with respect to the vertical axis ($M_{S,fr-le,z}$, $M_{S,fr-mi,z}$, $M_{S,fr-ri,z}$, $M_{S,re-le,z}$, $M_{S,re-mi,z}$ and $M_{S,re-ri,z}$). Until the evolvment of the vibrations, the signals show similar behaviour to

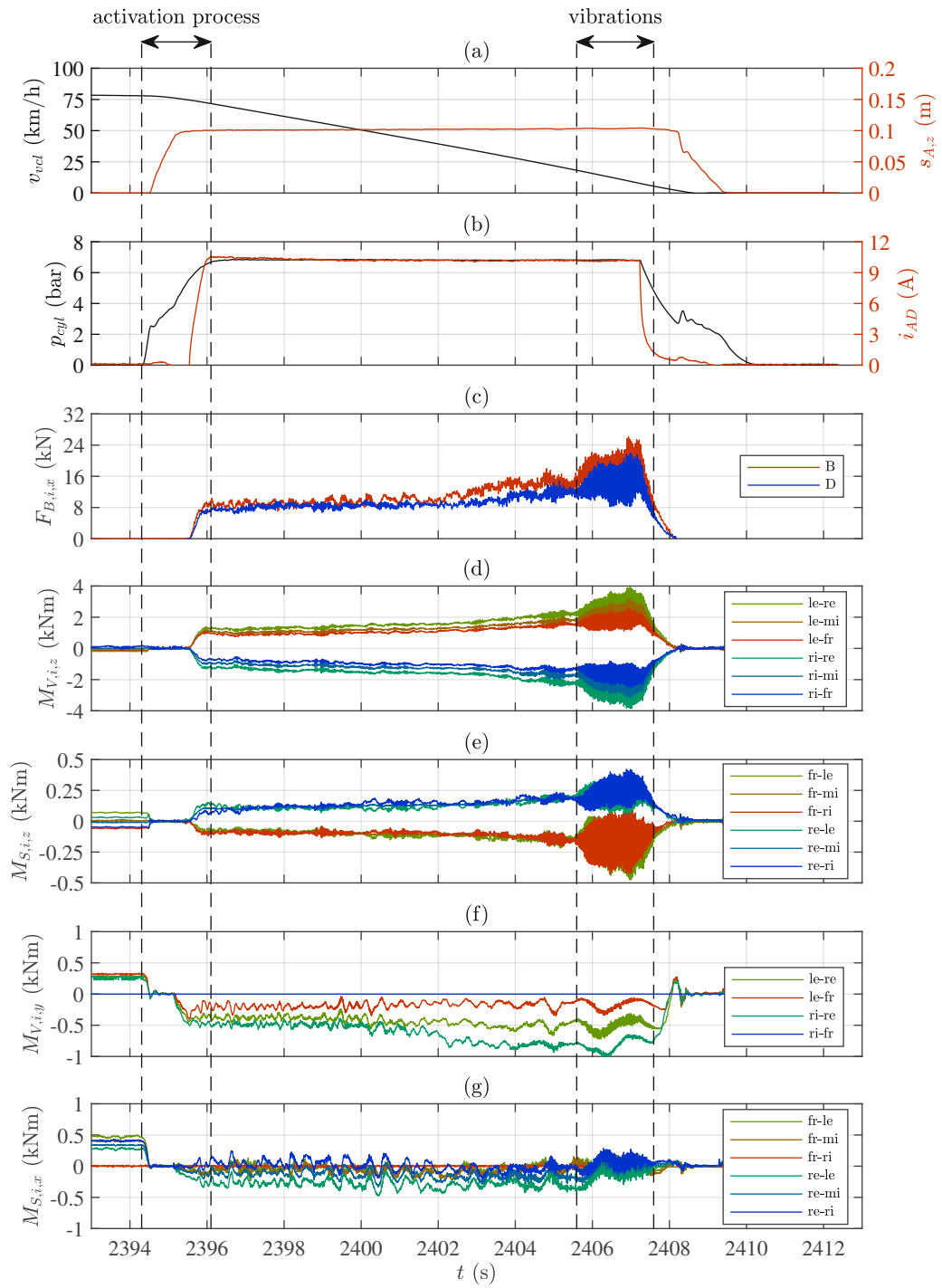


Figure 2.4: Field test measurements, overview

the transmitting forces and the bending moments of the connector beams with increasing magnitudes during the braking manoeuvre.

Diagram (f) shows the bending moments of the left and right connector beams with respect to the lateral axis ($M_{V,le-re,y}$, $M_{V,le-fr,y}$, $M_{V,ri-re,y}$ and $M_{V,ri-fr,z}$). The signal of $M_{V,ri-fr,z}$ is permanently zero as this measurement channel failed during the tests. From the others it can be seen that there is a positive bending moment in the ready position of the track brake when the actuation cylinders pull the track brake towards the centring devices. When the brake moves down onto the rail the bending moments are roughly zero. After the touch-down of the brake onto the rail, the bending moments become negative. During braking, the bending moments vary in the range of ± 500 Nm. This indicates a change in the magnet-rail contact conditions. During the vibrations, there are only minor amplitudes in the signals of the bending moments with respect to the lateral axis. This indicates that the track brake oscillates generally in the x - y -plane without a vertical component.

In the last diagram, the bending moments of the front and rear track rods with respect to the longitudinal axis ($M_{S,fr-le,x}$, $M_{S,fr-mi,x}$, $M_{S,fr-ri,x}$, $M_{S,re-le,x}$, $M_{S,re-mi,x}$ and $M_{S,re-ri,x}$) are shown. The measuring point $M_{S,fr-ri,x}$ has failed during the tests, therefore the signals are zero. At the beginning of the record the behaviour is similar to the bending moments of the connector beams with respect to the lateral axis. The bending moment is positive when the brake is pulled towards the centring devices and zero while moving downwards. When braking however, the signals fluctuate around the zero-line indicating dynamical brake-rail contact conditions. Also, vibrations show only minor amplitudes at these measuring points.

Next, the activation of the track brake is analysed in more detail in the range of time index $t \approx 2394$ - 2397 s. This covers the whole activation process from the pressurisation of the actuation cylinders until the full evolvment of the brake forces, Figure 2.5.

The process can be separated into in the following phases:

- Phase I, ready position, pressurisation:
The pressure p_{cyl} rises in the actuation cylinders with a steep gradient, Diagram (b). As a result, the bending moments $M_{V,i,y}$ and $M_{S,i,x}$ decrease to zero, Diagrams (f) and (g). At the end of this phase, the track brake loses contact with the centring devices.
- Phase II, track brake moves towards the rail:
The actuation cylinders extend, the track brake moves towards the rail and the signal $s_{A,z}$ increases, Diagram (a). As Diagrams (d) to (g) show, all bending moments are near zero as no external forces act on the structure of the brake frame. p_{cyl} rises with a flatter gradient until the touch-down of the magnets onto the rail.
- Phase III, track brake is contacting the rail (electrically still deactivated):
The track brake touches the rail, but no electrical voltage is yet applied to the

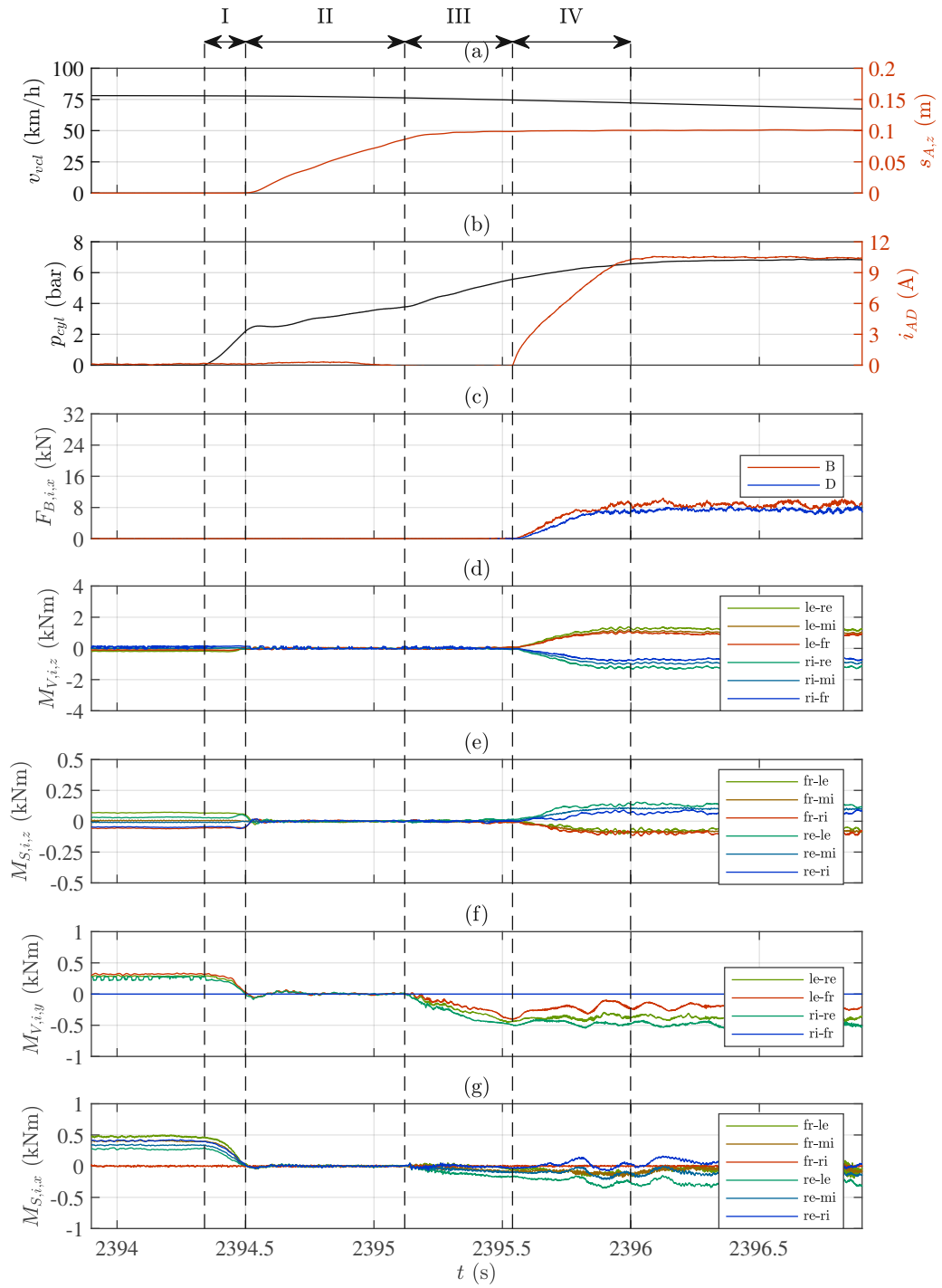


Figure 2.5: Field test measurements, detail: brake activation process

electromagnets. The vertical forces of the actuation cylinders increasingly push the track brake onto the rail due to a further increase of p_{cyl} . As a result, bending moments of the connector beams with respect to the lateral axis $M_{V,i,y}$ become negative, Diagram (f). The transmitting forces $F_{B,i,x}$ are still near zero, Diagram (c).

- Phase IV, electrical activation:
Voltage is applied and therefore the current i_{AD} evolves, Diagram (b). Magnetic forces evolve and pull the magnet onto the rail. Friction forces between the pole shoes of the magnets and the rail are transmitted to the bogie and $F_{B,i,x}$ increase. Moreover, the bending moments with respect to the vertical axis $M_{V,i,z}$ and $M_{S,i,z}$ increase. This phase ends when the current reaches a steady value.

Finally, the oscillations are regarded in greater detail. Figure 2.6 shows the respective time frame at $t = 2405.5-2406.5$ s. From the transmitting forces it can be seen that the track brake vibrates in an asymmetric mode as the signals of the forces $F_{B,B,x}$ and $F_{B,D,x}$ oscillate in phase opposition.

This observation is confirmed by the signals of the bending moments with respect to the z -axis of the left and right connector beams $M_{V,i,z}$. The quasi-static symmetrical bending moments of the left and right connectors are superimposed by an anti-symmetrical oscillation. Moreover, the signals of the bending moments of one side are approximately in phase with the brake forces of the same side (e.g. $F_{B,B,x}$ and $M_{V,le-re}-M_{V,le-fr}$).

From the signals of the bending moments with respect to the z -axis of the front and rear track rods, the anti-symmetric vibration can also be detected. The signals of the left ($M_{S,fr-le,z}$ and $M_{S,re-le,z}$) and right ($M_{S,fr-ri,z}$ and $M_{S,re-ri,z}$) measuring points oscillate in phase opposition around the constant signal of the centre ($M_{S,fr-mi,z}$ and $M_{S,re-mi,z}$) measuring points.

Evaluation of the vibrations in the frequency domain

To observe the influence of velocity on both amplitude and frequency, analyses are performed in the frequency domain. The diagrams in Figure 2.6 show that the signals of the eccentric bending moments with respect to the vertical axis of the track rods (e.g. $M_{S,re-fr,z}$) are suitable indicators of occurring vibrations.

During braking, the signals of the bending moments are recorded for a broad band of vehicle velocities. Subsequently, data sets are segmented and evaluated for discrete velocity windows with a size of $\Delta v = 1$ km/h. Figure 2.7 shows the power spectral density (PSD) of a segment of $M_{S,re-fr,z}$ for a window of $v_{vcl} = 10-11$ km/h. The diagram clearly indicates a dominant single peak in the PSD level of the signal at a frequency of $f = 28.5$ Hz.

To get an overall view on the occurrence of vibrations, the PSDs for all 132 braking tests are averaged for the velocity windows to mean PSDs. By plotting the PSDs with respect

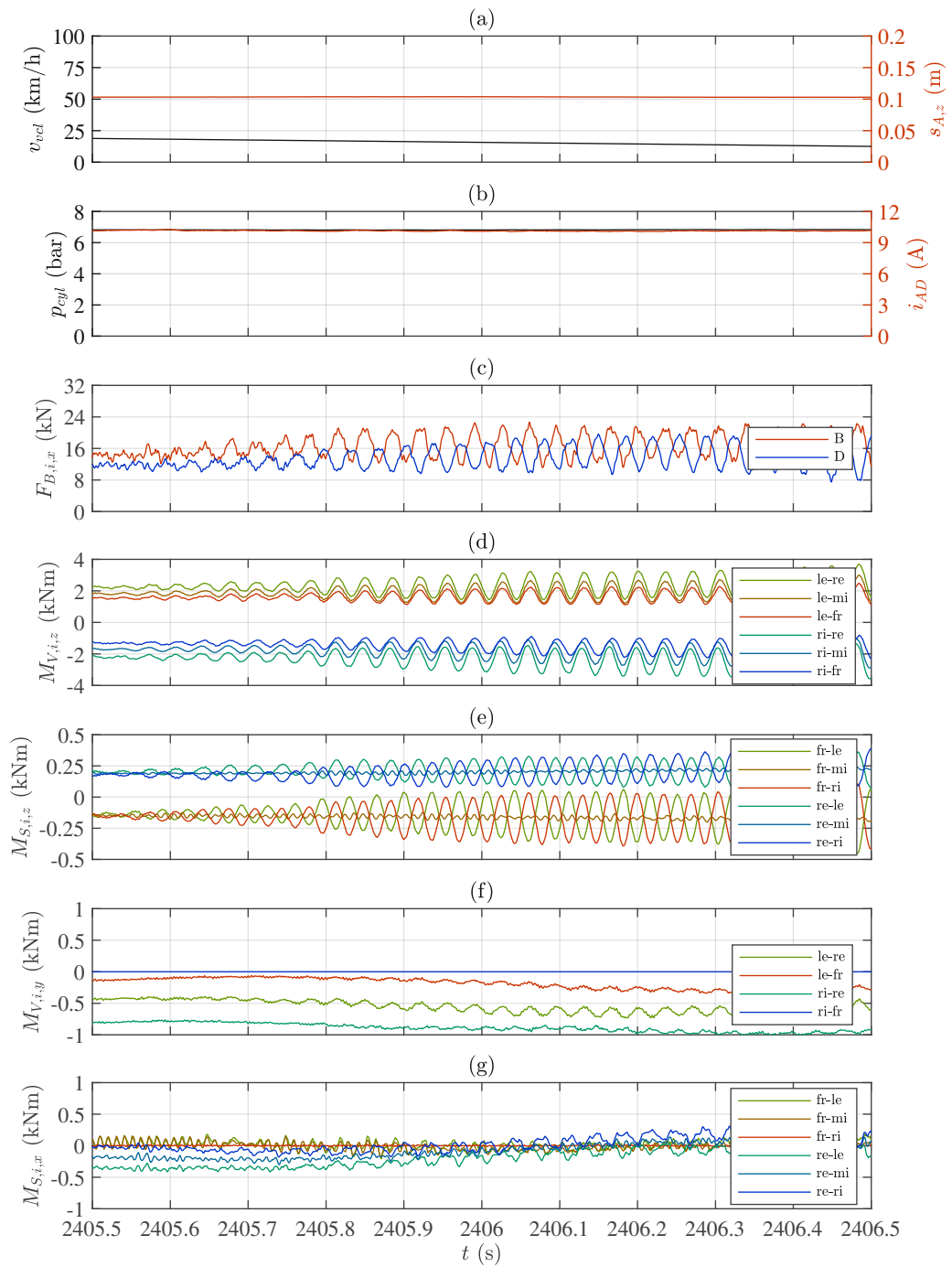


Figure 2.6: Field test measurements, detail: oscillation at low velocities

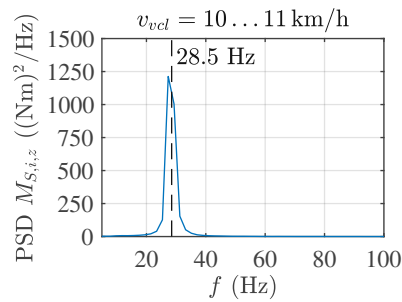


Figure 2.7: Mean PSD of bending moment at 10 km/h

to v_{vel} , velocity dependent oscillations and possible frequency shifts can be recognised. Figure 2.8 shows a diagram of the mean PSDs calculated for the different velocity windows. The PSD values are represented as colour map over the horizontal frequency axis. The vertical axis shows the velocity range from 0-100 km/h. The diagram indicates that the dominant oscillation frequency of ≈ 28.5 Hz is constant for all velocities.

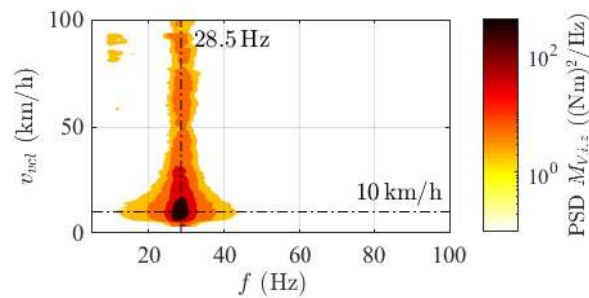


Figure 2.8: Mean PSD for 0-100 km/h

The root of the area below the PSD curve of one segment of a signal (as in Figure 2.7) corresponds to the root mean square (RMS) for the evaluated velocity. By evaluating all segments, the RMS value is obtained as a function of vehicle velocity as seen in Figure 2.9.

In the diagram, the RMS values and therefore the amplitudes significantly rise for velocities lower than 20 km/h. When approaching ≈ 10 km/h, the RMS values decrease again. No conclusions can be drawn for velocities below 10 km/h, as the brake was deactivated at this velocity.

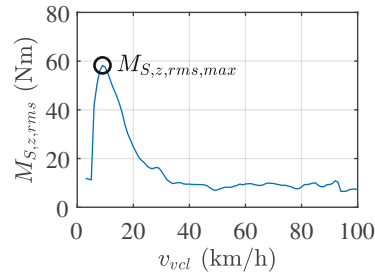


Figure 2.9: RMS value of the bending moment with respect to v_{vcl}

Correlation of vibrations and brake force

It is clear that the mechanisms leading to the vibrations cannot be identified by solely evaluating the vehicle tests. Nevertheless, it has already been phenomenologically observed that the vibrations are dependent on the vehicle speed while the dominant frequency is not.

Next, the vehicle test data is used to investigate whether the occurrence of the vibrations correlates not only with the velocity but also with the magnitude of the brake forces (at approximately constant velocity). As already discussed in Section 1.2, the (velocity-dependent) brake force may vary within broad bands of variation ([52],[9]), Figure 1.6. On the one hand, the magnetic attraction force F_A is strongly influenced by pick-up weldings on the pole shoes. On the other hand, the sliding friction coefficient μ_G between pole shoes and rail depends on the environmental conditions.

Figure 2.10 shows the equivalent brake force $F_{B,x,eq}$ (1.19) with respect to the initial vehicle velocity $v_{vcl,0}$. Each point in the diagram represents one braking manoeuvre with an initial velocity of between 18 and 135 km/h. It can be seen that brake forces generally increase with decreasing velocity. The two dashed lines show the 25 % and 75 % percentiles during the tests. The large degree of variation observed can be explained mainly by changing weather conditions during the test days and pick-up weldings observed on the pole shoes, Figure 1.7.

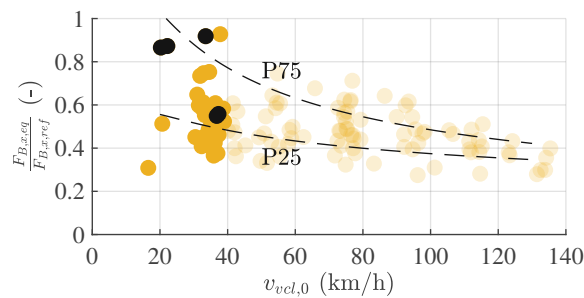


Figure 2.10: Normalised equivalent brake force vs. initial velocity

For the correlation analysis between vibrations and brake force, it is intended to select only braking manoeuvres with similar test parameters. To obtain comparable data, the datasets are therefore selected using the following criteria:

1. The tests must have been conducted at a low initial velocity of under $v_{vcl,0} \approx 40$ km/h. It is assumed that no further pick-up weldings are added on the pole shoes at low velocities. Therefore, contact conditions between rail and track brake are assumed to be constant during one brake test. The remaining records are marked in Figure 2.10 with bold dots.
2. The tests must have been performed in close succession. The remaining records are marked in the diagram as bold black dots.

The braking tests selected are listed in Table 2.1.

Test	time	initial velocity
V1006	Day 1, 2:23	25.2 km/h
V1007	Day 1, 2:24	23.1 km/h
V1008	Day 1, 2:26	37.2 km/h
V1014	Day 1, 2:56	40.3 km/h
V1019	Day 1, 4:31	39.9 km/h

Table 2.1: Selected braking tests

Figure 2.11 shows the maximum RMS level of the bending moment in a track rod $M_{S,z,rms,max}$ with respect to the equivalent brake force $F_{B,x,eq}$. Again, every point represents one braking test. The bold yellow and black dots mark the selected data points considering the above criteria. Although the data points are generally highly scattered, a correlation between $F_{B,x,eq}$ and $M_{S,z,rms,max}$ can be observed with the selection made. It can therefore be assumed that the occurrence of vibrations is more probable with high levels of brake force than with low levels. However, a systematic analysis of parameters using mathematical models is required to make qualitative statements. Such mathematical models are developed in Chapter 3.

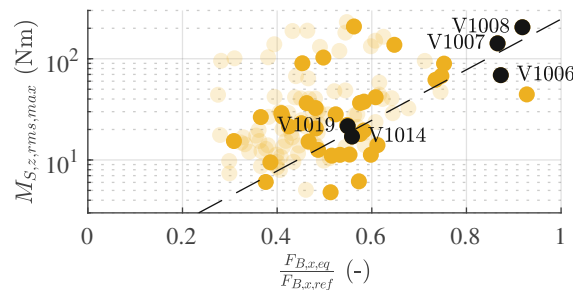


Figure 2.11: Correlation between brake force and RMS value of the bending moment

2.3 Modal analysis of the magnetic track brake

Experimental and finite element modal analyses are performed to determine whether the measured vibrations correspond to an eigenmode of the structure. Any magnetic forces between the magnet and the rail are neglected at this stage. Figure 2.12 shows the first three eigenmodes of the structure obtained by the FE analysis. Here, the boundary conditions are chosen to simulate the state of the track brake while braking. The magnets are assumed to slide on the top surface of the rail. Therefore, the vertical displacements of the pole shoes with respect to the horizontal plane are constrained. Mechanical stops on both sides on the front of the track brake are assumed to have contact with the bogie with displacements in the longitudinal and lateral directions of the mechanical stops constrained. The frequency of the vibrations occurring in the vehicle tests corresponds to that of the second asymmetric mode of the structure, Figure 2.12(c).

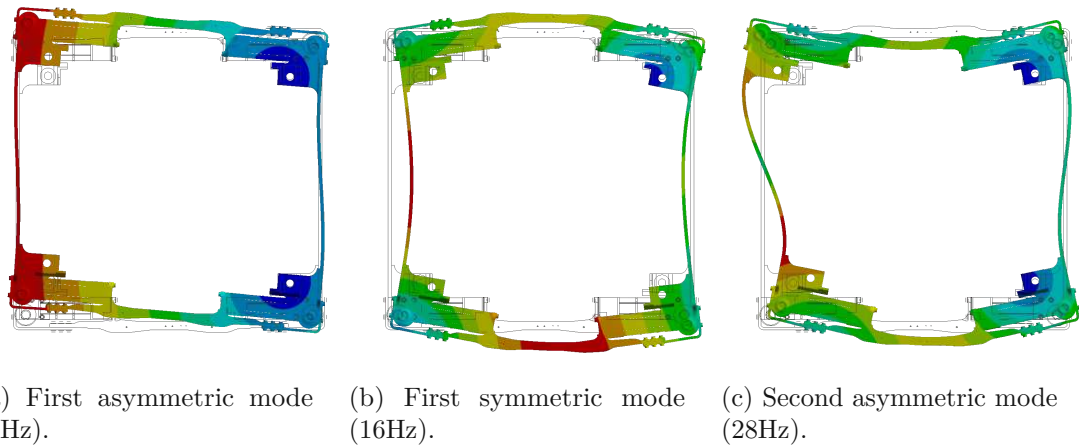


Figure 2.12: First three eigenmodes of the track brake frame (FE modal analysis)

Subsequently, the associated eigenmode is verified using time histories of bending moments from the vehicle tests as well as a laboratory experiment. From the finite element modal analysis, the modal bending moments with respect to the z -axis are derived. Figure 2.13 shows diagrams of the modal bending moments in the second asymmetric mode individually for the longitudinal connectors and the track rods. In the diagrams, the locations of the measurement points introduced in Figure 2.1 are highlighted. The second asymmetric mode can be clearly identified from the signals using the following criteria:

- The bending moments of the left and right connector beams point in opposite directions.
- The bending moments of the rear and front track rods point in opposite directions.
- In both track rods, bending moments change signs at their geometrical centres.

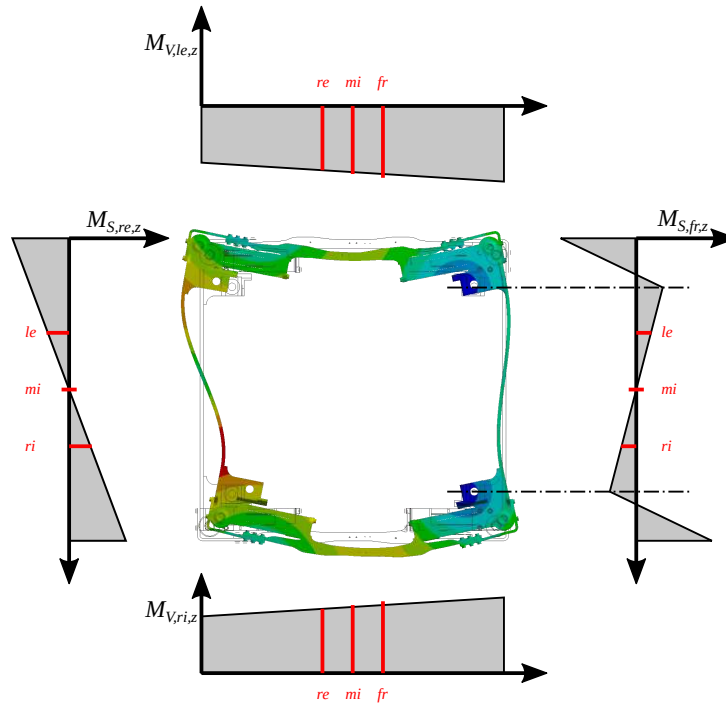


Figure 2.13: Bending moments of second asymmetric mode

To validate the results of the structural finite element model, a vibration test of the track brake is performed. In this test, a track brake is mounted on a 6-DoF hydraulic vibration test rig as seen in Fig 2.14. To simulate the boundary conditions of the finite element analysis, the track brake is placed on an inclined plane on the test bench with the mechanical stops fixed. The pole shoes can slide on the inclined plane. The vibration test rig is excited around the rotated vertical axis z_{MG} with a sine sweep of constant angular acceleration amplitude. During the test, the frequency is varied in the range of $f_{sweep} = 0\text{-}40$ Hz.

The strain gauge measuring points applied to the track brake in this laboratory test correspond to those from the vehicle test, Figure 2.1. At 8 Hz and 28 Hz, asymmetrical eigenmodes were found. Figure 2.15 shows signals of bending moments with respect to the vertical axis of the longitudinal connecting beams and of the track rods. In the left diagrams, the excitation frequency of the sine sweep equals 8 Hz, in the right ones 28 Hz.

Diagrams (a), (b), (c) and (d) show the signals of the bending moments in the longitudinal connector beams on the left ($M_{V,le-fr}$, $M_{V,le-mi}$, $M_{V,le-re}$) and right ($M_{V,ri-fr}$, $M_{V,ri-mi}$, $M_{V,ri-re}$) sides of the brake. At both frequencies, bending moments of the left and right connector beams oscillate in phase opposition. Therefore, asymmetric oscillation modes are found for both frequencies.



Figure 2.14: Vibration test of the magnetic track brake

In Figure 2.15 (e), (f), (g) and (h) the bending moments of the front ($M_{S,fr-le,z}$, $M_{S,fr-mi,z}$, $M_{S,fr-ri,z}$) and rear ($M_{S,re-le,z}$, $M_{S,re-mi,z}$, $M_{S,re-ri,z}$) track rods are shown. In all four diagrams, the centre track rod bending moments $M_{S,fr-mi,z}$ and $M_{S,re-mi,z}$ (dash-dotted lines) are nearly zero. The (eccentric) bending moments on the left and right sides oscillate in phase opposition. This proves that the modes are asymmetric. When comparing the phases of the left ($M_{S,fr-le,z}$, $M_{S,re-le,z}$) and right ($M_{S,fr-ri,z}$, $M_{S,re-ri,z}$) bending moments at the two frequencies, two different asymmetric modes can be clearly identified. At 8 Hz, the right-eccentric bending moments $M_{S,fr-ri,z}$ and $M_{S,re-ri,z}$ (dashed lines) of the two track rods oscillate in phase, Diagrams (e) and (g). At 28 Hz, they oscillate in phase opposition, Diagrams (f) and (h). Obviously, the same applies to the left-eccentric bending moments (solid lines). The vertical dashed lines in the 28 Hz diagrams mark a moment in time in which a deflection occurs equal to Figure 2.13. As shown, the measurements are consistent with the calculated modal bending moments.

The signals of the bending moments with respect to the vertical axis measured during the shaker test are similar to those measured during the vehicle test, see Figure 2.6 (d) and (e). Even though the signals are smaller in amplitude in the laboratory test, the signals are equal in phase and frequency. However, the field test measurements are offset due to the quasi-static deformation generated by the brake forces.

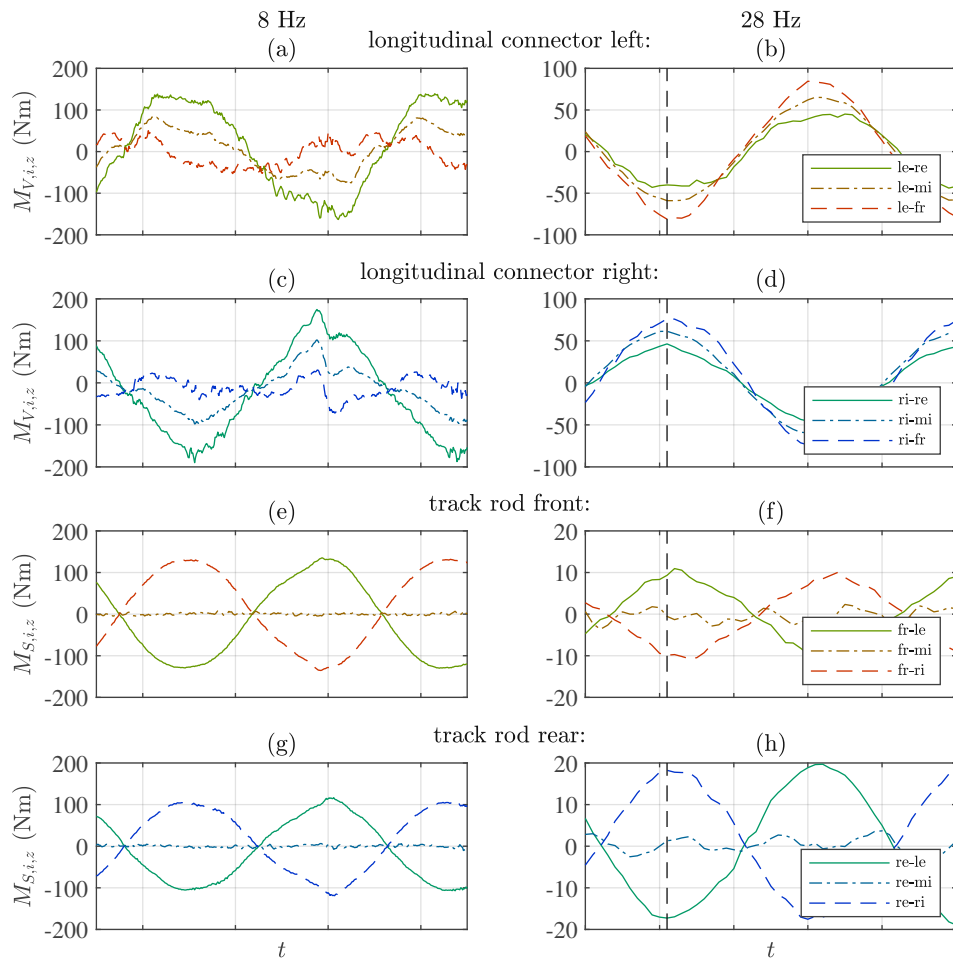


Figure 2.15: Vibration test of the magnetic track brake

2.4 Field tests on the coefficient of friction

As an engineering approach, for this study, the friction characteristics are measured in a field test with a vehicle on a real track. During deceleration of the railway vehicle, a track brake is pressed onto the rail only by the force of the actuation cylinders $F_{cyl,i,z}$ ($i = A, B, C, D$). The vertical force is calculated from the cylinder pressure measured. Neglecting friction in the actuating cylinder, the force of the actuating cylinder $F_{cyl,i,z}$ is a function of p_{cyl} , the piston area A_{cyl} , the combined spring stiffness k_{cyl} , the position of the cylinder $s_{i,z}$ as well as the installation and nominal length of the two springs $l_{s,1}$ and $l_{s,2}$:

$$F_{cyl,i,z} = p_{cyl}A_{cyl} - k_{cyl}(s_{i,z} + l_{s,1} - l_{s,2}) \quad (2.1)$$

Further, the interfacing forces between the track brake and the bogie $F_{B,x,i}$ are measured. The friction coefficient is calculated as the ratio of the two forces:

$$\mu_G(v) = \frac{\sum_i F_{B,i,x}(v)}{\sum_i F_{cyl,i,z}(v)} \quad (2.2)$$

Figure 2.16 shows a diagram of the velocity-dependent friction coefficients obtained. From the signals, a mean μ_G characteristics is determined, as well as an upper and a lower limit, low μ_G and high μ_G , using a function fit (2.3) and parameters according to Table 2.2. During the evaluation, it should be noted that short dips in brake force can occur, which are filtered out if necessary. Reasons for this can be disturbances in the track (e.g. switches and crossings) or local contamination.

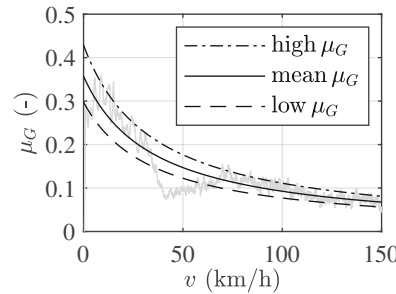


Figure 2.16: Coefficient of friction obtained from vehicle tests

$$k\mu_G(v) = \frac{k_{level}}{a_1 * (v_0 + v) + a_0} \quad \text{with } k = (\text{high, mean, low}) \quad (2.3)$$

k	k_{level} (-)	a_0 (-)	a_1 (h/km)	v_0 (km/h)
high	1.20	2	0.08	10
mean	1.00	2	0.08	10
low	0.833	2	0.08	10

Table 2.2: Parameters of the function fit of the velocity dependent friction characteristics

Modelling the electromagnetic track brake

Several papers have already dealt with the dynamical modelling of electromagnetic track brakes. This includes in particular the transient switch-on process investigated in the x - z plane using electro-magneto-mechanical models, see Jirout et al. [40] and Galardi et al. [44]. These studies clearly show that it is necessary to consider the electrical, magnetic and mechanical domains as coupled subsystems, Figure 3.1. Electro-magnetic coupling occurs in the coil of the electromagnets. Current excites a magnetic field, which induces a magnetic flux through the ferromagnetic core, the rail and the (small) air-gap in between. Vice-versa, voltage is induced in the coil by variations of the magnetic field. Magneto-mechanical coupling occurs in the variable air-gap between the magnet and the rail. Relative motion of the magnet opens or closes the air-gap and changes the magnetic reluctance of the circuit. Magnetic forces between the rail and the magnet act on the structure of the brake magnets.

The measurements from the field tests examined in the previous chapter have shown that oscillation during braking occurs mainly in the x - y plane, which has not been addressed in scientific publications so far. As the aim of this thesis is to understand self-excitation

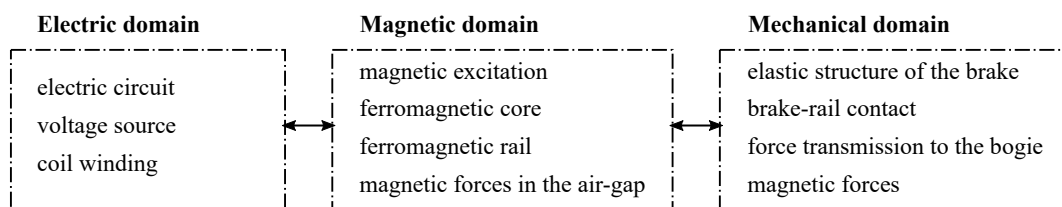


Figure 3.1: Physical domains of a mathematical model of a track brake

mechanisms and to explore ways of weakening or preventing them, dynamical models are required for further analysis. To investigate the stability behaviour in the x - y plane and further in 3D space, mathematical models of different complexity are developed in this chapter.

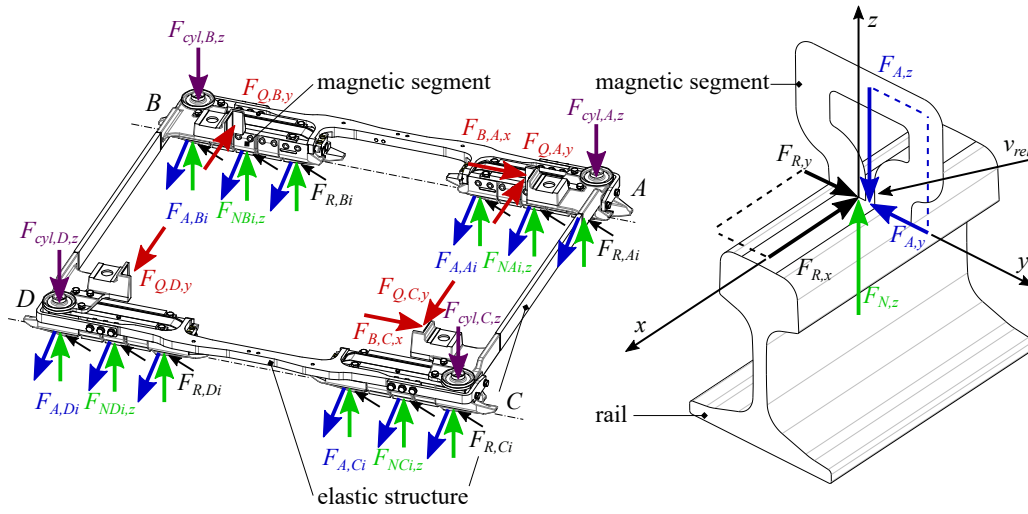
Highly simplified models aim to explore excitation mechanisms and to gain a basic understanding of the influence of individual model parameters in an intuitive way. The models should be simple enough to allow a semi-analytical consideration of the terms of the differential equations and will be addressed in Chapter 4 to investigate the mechanisms that lead to self-excited oscillations using methods of linear system analysis.

With the aim of transferring the knowledge gained to future track brake designs, the modelling complexity is then increased. With a more detailed system model, it should be possible to obtain qualitatively comparable results with field tests and to investigate the trajectories of solutions of the dynamical system with respect to individual design features using methods of multibody dynamics simulation, Chapters 5 and 6. Therefore, for each of the three physical domains, simplified and more complex models are described which are subsequently assembled to overall system models of varying complexity.

3.1 Mechanical submodels of the track brake

The mechanical models of the track brake described in this section cover the structure of its frame, the acting forces as well as the contact conditions between the brake magnets and the rails. Figure 3.2(a) shows the forces acting on the elastic magnetic track brake frame. The four corners of the brake are labelled $j = A, B, C, D$. At the mechanical stops act longitudinal transmission forces $F_{B,A,x}$ and $F_{B,C,x}$ (front corners in the direction of travel) as well as lateral guiding forces $F_{Q,j,y}$. The actuation cylinder forces $F_{cyl,j,z}$ act on all four corners in vertical direction. Normal contact forces and the friction forces act between the pole shoes of the magnets and the rail. Figure 3.2(b) shows a detailed diagram of a magnetic segment. In this context, a magnetic segment may be either an endpiece or an intermediate element of a braking magnet. The normal contact force $F_{N,z}$ acts at the contact point between the rail and the pole shoe. Further, the diagram shows the friction force with the components $F_{R,x}$ and $F_{R,y}$ pointing in opposite direction to the relative sliding velocity v_{rel} as well as the magnetic force with its components $F_{A,z}$ and $F_{A,y}$.

The longitudinal position of friction contact points on the underside of the pole shoes of the brake magnets and the rail depend on the current operating and wear conditions. Figure 3.3 shows a side view of a braking magnet A resting on a rail. In the case shown, only one endpiece (A2) is in contact with the rail because a pick-up welding on the underside of the intermediate element ZG1 lifts the coil body. There is a clear air-gap and between endpiece A1 and the rail. With dynamical load states and variable positions and thicknesses of pick-up weldings, contact points between the magnet and the rail must be considered variable as well.



(a) Forces acting on the brake frame (b) Forces acting on a magnetic segment

Figure 3.2: Forces acting on a magnetic track brake

The mechanical models consider friction forces F_R between the track brake and the rail. In all models described, a Colom friction model with a velocity-dependent coefficient of friction $\mu_G(v_{rel})$ is used. Friction forces are therefore calculated by $F_R = \mu_G(v_{rel})F_{N,z}$.

In this section, mechanical sub-models of the magnetic track brake of varying complexity are presented. Starting with a 1-DoF planar model to investigate basic effects, the level of detail is increased to a 3D multibody dynamics model to explore the influence of design features.

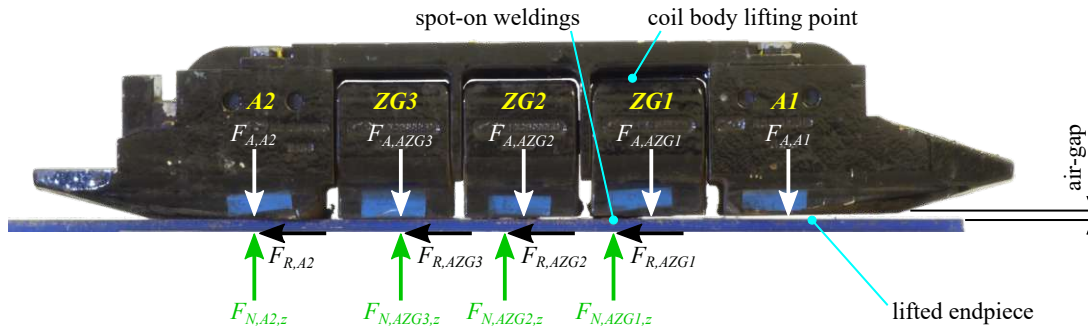


Figure 3.3: Contact points between the braking magnet and the rail

3.1.1 Mechanical model for linear system analysis

For linear system analysis, a planar (x - y) 1-DoF-mechanical model is developed, Figure 3.4. The model represents one quarter of a track brake in the second asymmetric eigenmode of the structure identified by modal analysis, see Section 2.3. To study the behaviour of multiple coupled magnets and to be able to distinguish between symmetrical and asymmetrical deflection modes, the model is subsequently extended by an additional quarter model.

The model consists of a rigid lever with a point-mass m_{MG} and a moment of inertia $I_{MG,0}$ with respect to a moved joint at 0, representing one magnet moving in longitudinal direction x at constant velocity \tilde{v} . The mechanical state variable α describes the deflection of the structure under load. The distance a represents the lateral offset between the line of action (of the longitudinal component) of the friction force F_R and the transmission link at 0. l describes the longitudinal distance of the contact point of the magnet on the rail. At the force application point A, magnetic forces $F_{A,y}$ and $F_{A,z}$, which are derived in the magnetic submodel, and the corresponding friction force F_R are applied. The velocity \tilde{v} is assumed to be large enough to neglect the lateral component of the friction force, $\tilde{v} \gg l\dot{\alpha}$.

The rotational spring stiffness c_{rot} and $I_{MG,0}$ are chosen to match the (undamped) eigenfrequency ω_0 of the second asymmetric mode of the brake frame with

$$\omega_0 = \sqrt{\frac{c_{rot}}{I_{MG,0}}}. \quad (3.1)$$

Using the damping coefficient d_{rot} , the natural damping of the mechanical system is defined with the damping ratio D following from

$$D = \frac{d_{rot}}{2\omega_0}. \quad (3.2)$$

The nonlinear characteristics of the velocity-dependent friction coefficient $\mu_G(v_{rel})$ are linearised with respect to \tilde{v} , $\mu_G(v_{rel}) = \tilde{\mu}_G + k_\mu v_{rel}$ with $v_{rel} = v - \tilde{v}$ and typically

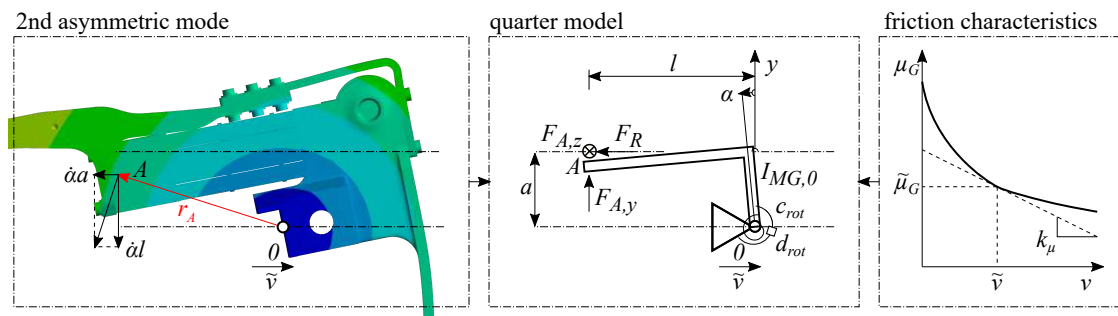


Figure 3.4: Mechanical model

$k_\mu \leq 0$, see Figure 3.4 on the right. \tilde{v} is considered to change slowly enough to yield time-independent system coefficients. For small angles α and small lateral velocities, the equation of motion (3.3) is derived.

$$I_{MG,0}\ddot{\alpha} + d_{rot}\dot{\alpha} + c_{rot}\alpha = aF_{A,z}(\tilde{\mu}_G - k_\mu a\dot{\alpha}) - lF_{A,y} \quad (3.3)$$

An expansion of the one quarter model is the double-magnet model, Figure 3.5. The model is created by mirroring the single magnet model around the longitudinal axis resulting in a mechanical model with the two DoFs α_A and α_B . The lateral levers are extended by the length b to the symmetry axis of the model. Inertially fixed rotational stiffnesses and rotational dampers are replaced by relative stiffnesses (b^2c_x and $c_{rot}/2$) and relative dampers (b^2d_x and $d_{rot}/2$) between the rigid bodies.

The equations of motion of the double-magnet model result in (3.4) and (3.5).

$$I_{MG,0}\ddot{\alpha}_A + \underbrace{\frac{d_{rot}}{2}(\dot{\alpha}_A + \dot{\alpha}_B)}_{\text{sym. damp.}} + \underbrace{b^2d_x(\dot{\alpha}_A - \dot{\alpha}_B)}_{\text{asym. damp.}} + \underbrace{\frac{c_{rot}}{2}(\alpha_A + \alpha_B)}_{\text{sym. stiff.}} + \underbrace{b^2c_x(\alpha_A - \alpha_B)}_{\text{asym. stiff.}} = aF_{A,A,z}(\tilde{\mu}_G - k_\mu a\dot{\alpha}_A) - lF_{A,A,y} \quad (3.4)$$

$$I_{MG,0}\ddot{\alpha}_B + \frac{d_{rot}}{2}(\dot{\alpha}_A + \dot{\alpha}_B) + b^2d_x(\dot{\alpha}_B - \dot{\alpha}_A) + \frac{c_{rot}}{2}(\alpha_A + \alpha_B) + b^2c_x(\alpha_B - \alpha_A) = aF_{A,B,z}(\tilde{\mu}_G - k_\mu a\dot{\alpha}_B) - lF_{A,B,y} \quad (3.5)$$

If $b^2c_x = c_{rot}/2$ and $b^2d_x = d_{rot}/2$, a special case occurs: Then, (3.4) and (3.5) equal the equation of motion of the single magnet model (3.3).

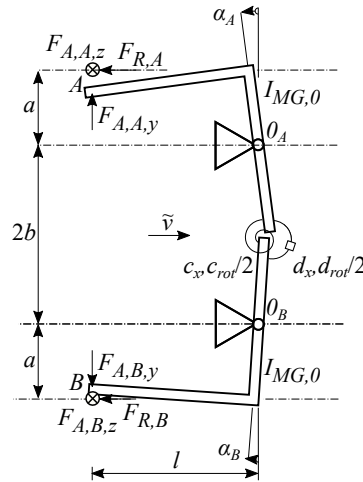


Figure 3.5: Double-magnet mechanical model

3.1.2 Mechanical model for multibody dynamics simulation

The mechanical model for multibody dynamics simulation is created using the multibody dynamics software SIMPACK [53]. The model consists of a rigid body representing the mass of the vehicle m_{DG} and a flexible body (Craig-Bampton method, see [54], [55]) representing the track brake frame, Figure 3.6. m_{DG} is connected to the inertial system by either a rheonomic joint (with $\dot{x}_{DG} = \tilde{v} = \text{const.}$) or a single degree of freedom prismatic joint with the state variable x_{DG} . The elastic structure of the track brake covers the magnets at the four corners (A, B, C, D), the connecting beams on the two sides and the two track rods in the front and the rear and is connected to the inertial system by a 6 DoF joint with state variables $\alpha_{MG}, \beta_{MG}, \gamma_{MG}, x_{MG}, y_{MG}$ and z_{MG} .

At the positions of the mechanical stops, unilateral spring-damper contact elements in longitudinal ($F_{B,A,x}$ and $F_{B,C,x}$) and lateral ($F_{Q,A,y}$ and $F_{Q,C,y}$) directions are defined between the two bodies. An additional braking/transmission force $F_{B,vcl}$ is applied to m_{DG} .

Figure 3.7 shows the side view of corner j of the brake frame in detail with the force elements defined. The longitudinal transmission forces $F_{B,j,x}$ are applied in positive x direction at the height of the mechanical stop of the track brake. The actuating cylinder force $F_{cyl,j,z}$ points in negative z direction at the position of the actuating cylinder mounting point. Magnetic forces calculated in the magnetic submodel (Section 3.2.2) with lateral and vertical components $F_{A,j1,y}$ and $F_{A,j1,z}$ are applied to the outward and inward endpieces.

The track brake-rail contact is simulated by three unilateral spring-damper contact force elements $F_{N,j1,z}, F_{N,j2,z}$ (endpieces) and $F_{N,jZG,z}$ (intermediate element). The position of the intermediate contact point is defined by the longitudinal distance e_x and vertical offset e_z which is discussed in greater detail below.

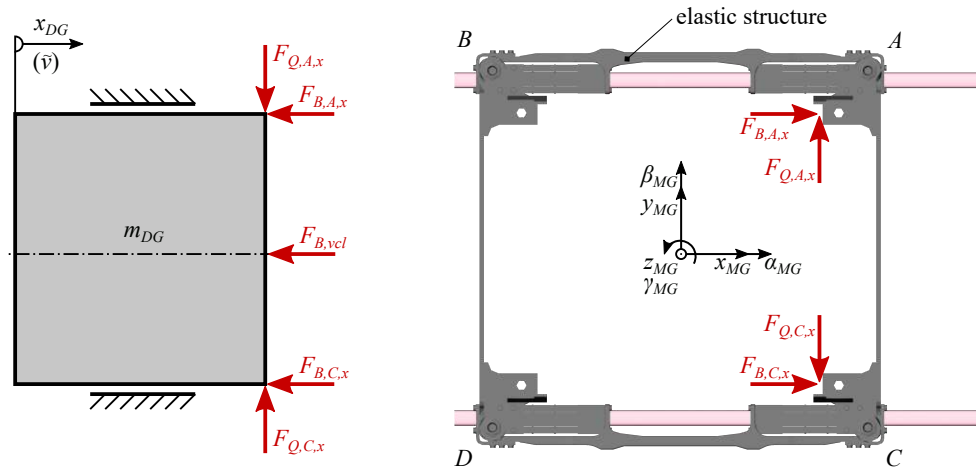


Figure 3.6: SIMPACK model – overview

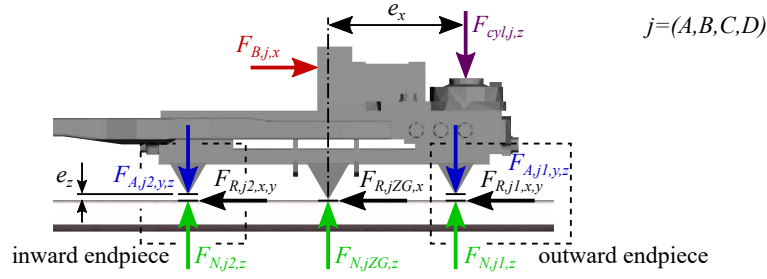


Figure 3.7: SIMPACK model – detail magnet

Friction forces at the endpieces are defined acting at their contact points in x and y directions:

$$F_{R,A1,x} = \frac{v_{A1,x}}{|\mathbf{v}_{A1}|} F_{N,A1,z} \mu_G(|\mathbf{v}_{A1}|) \quad (3.6)$$

$$F_{R,A1,y} = \frac{v_{A1,y}}{|\mathbf{v}_{A1}|} F_{N,A1,z} \mu_G(|\mathbf{v}_{A1}|) \quad (3.7)$$

Here, $\mathbf{v}_{A1} = [v_{A1,x} \ v_{A1,y}]^T$ is the vector of the sliding velocity on the contact plane and $\mu_{G,A1}(|\mathbf{v}_{A1}|)$ the velocity-dependent friction coefficient.

As intermediate elements are able to move freely in the lateral direction in the coil body (within limits), only longitudinal friction forces are considered in the contact points, see (3.8).

$$F_{R,AZG,x} = F_{N,AZG,z} \mu_G(v_{AZG,x}) \quad (3.8)$$

For the velocity dependent friction coefficient $\mu_G(|\mathbf{v}_{A1}|)$ the characteristics (2.3) is used.

3.2 Magnetic submodels of the track brake

The magnetic submodels are used to calculate the magnetic forces between the magnetic track brake and the rail dependent on their relative movement and the electrical excitation of the coil. This results in the requirement to solve a non-stationary magnetic field problem due to time-varying geometry and boundary conditions.

The finite element method (FEM) is currently the most widely developed and used calculation method to solve numerical field problems, Kallenbach [45]. A typical application of the FEM is the calculation of static lifting force characteristics of electromagnets and is also well established in the development of magnetic track brakes [7]. Both stationary and non-stationary problems of arbitrary geometry can be solved with high accuracy. Pötscher [49] describes the model creation and validation of a magnetic track brake including non-linear material behaviour for the stationary case. Comparisons of calculations and test results of magnetic forces show high agreement. The calculation of magnetic field problems with time-variant geometry requires, however, great computational effort [45]. For dynamical multi-domain simulations with multiple degrees of freedom, in-the-loop solving of transient magnetic FE models appears to be too computationally demanding.

The network method for calculating magnetic circuits is based on the physical analogy between magnetic and electric fields. The magnetic circuit is approximated by a network of concentrated elements including coils, constant or variable magnetic reluctances and eddy current loss elements. The decisive disadvantage of this method is that in order to construct the magnetic equivalent circuit, the basic field distribution must be known. Although it is becoming less and less important for the (static) design of electromagnets due to the use of FEM, the network method is still used for the rapid simulation of the dynamical behaviour of electromagnets [45].

Both Jirout et al. [40] and Galardi et al. [44] combine the magnetic network technique and the FEM for the dynamical calculation of magnetic forces. The models consider variable magnetic circuits due to a vertical movement of the track brake with respect to the rail. The ferromagnetic parts of the track brake are represented by a constant reluctance and the air-gap by a variable reluctance. The reluctance of the air-gap varies linearly with the vertical dimension of the air-gap. The magnetic resistances are determined using magnetostatic FEM calculations.

The models discussed in this thesis consider relative movements of the brake magnets and the rail in both vertical and lateral directions. Therefore, the network models described in [40] and [44] are expanded to include a variable lateral displacement of the brake magnet.

3.2.1 Magnetic submodel for linear system analysis

Figure 3.8(a) shows a finite element cross-section model of the magnetic track brake for calculating magnetic forces dependent on the relative coordinates to the centre of the rail y and z . The circuit is excited by the magnetomotive force of the coil $\Theta = Ni$ with the number of turns N and the electric current i . The main magnetic flux ϕ takes the path from the ferromagnetic core through the pole shoes, through the air-gap and the rail head. From results of magnetostatic analyses with the model, discrete values are obtained for the magnetic flux $\phi(y, z)$ and the magnetic forces $F_{A,y}(y, z)$ and $F_{A,z}(y, z)$.

Figure 3.8(b) shows the approximated network model with constant reluctances for the magnetic core of the magnet $R_{m,fe,Mg}$ and the rail $R_{m,fe,Ra}$ as well as a variable reluctance representing the two air-gaps between the rail and the two poles of the magnetic core $R_{m,ls}(y, z)$ and the eddy-current loss element L_m . By applying Ampère's law, the differential equation for the magnetic flux ϕ is found, (3.9).

$$\underbrace{Ni}_{\text{excitation}} = \underbrace{(R_{m,fe,Mg} + R_{m,fe,Ra} + R_{m,ls}(y, z))}_{R_{m,fe}=\text{const.}} \phi + \underbrace{G\dot{\phi}}_{\text{eddy losses}} \quad (3.9)$$

The reluctance of the two combined air-gaps $R_{m,ls}$ depends on the calculated effective air-gap $s(y, z)$; μ_0 represents the vacuum permeability and A the magnetic cross-section of the air-gap (3.10).

$$R_{m,ls}(y, z) = \frac{s(y, z)}{\mu_0 A} \quad (3.10)$$

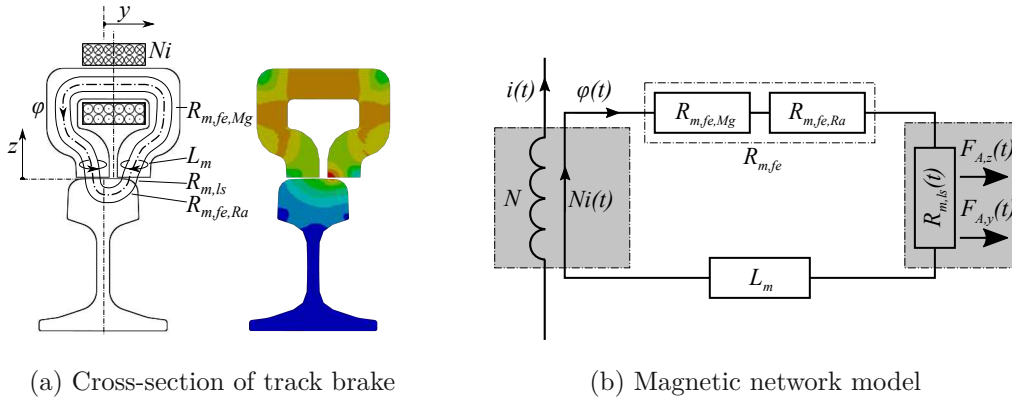


Figure 3.8: Modelling of the magnetic circuit

For the magnetostatic case ($\dot{\phi} = 0$), s can be directly expressed from (3.9) and (3.10) and is chosen as a function of y and z (3.11) to approximate the finite element results of ϕ with the network model (3.9).

$$s(y, z) = \frac{a_{hyp} \sqrt{b_{hyp}^2 + y^2}}{b_{hyp}} + 2z + a_0 \quad (3.11)$$

Figure 3.9(a) shows the evaluated Equation (3.11) for $z = z_0$ with respect to the lateral displacement y (red line). Moreover, the diagram depicts the corresponding magneto-static flux calculated with (3.9) (continuous black line) along with the finite element results (circles). The magnetic flux ϕ relates inversely proportional to the lateral displacement and the air-gap with a maximum when the magnet is centred.

The magnetic forces $F_{A,y}$ and $F_{A,z}$ are defined as the partial derivatives of the magnetic co-energy $W_{m,ls}^*$ [45] with respect to y and z , see (3.12) to (3.14).

$$W_{m,ls}^*(y, z) = \phi \frac{V_m}{2} = \phi^2 \frac{R_{m,ls}(y, z)}{2} = \phi^2 \frac{s(y, z)}{2\mu_0 A} \quad (3.12)$$

$$F_{A,y}(y, z) = \frac{\partial W_{m,ls}^*(y, z)}{\partial y} = \frac{\phi^2}{2\mu_0 A} \frac{\partial s}{\partial y}(y, z) \quad (3.13)$$

$$F_{A,z}(y, z) = \frac{\partial W_{m,ls}^*(y, z)}{\partial z} = \frac{\phi^2}{2\mu_0 A} \frac{\partial s}{\partial z}(y, z) \quad (3.14)$$

Figure 3.9(b) depicts the magnetic forces (3.13) and (3.14) of the network model (3.9) assuming $\phi = 0$ compared to the finite element results. Similar to the magnetic flux ϕ , the vertical force $F_{A,z}$ reaches its maximum when the magnet is centred above the rail. The lateral force $F_{A,y}$ acts opposite to the displacement y and thus has a centring effect.

For the linear system analysis it is assumed that the magnet always rests on the rail. Therefore, the vertical displacement is constant $z = z_0$, s (3.11) thus varies with y only. $z = z_0$ depends on the assumed state of the pole shoes. Pick-up weldings increase z_0 and thus also the effective air-gap s . Appendix B.2 describes a method to determine realistic values of s based on field tests and laboratory tests.

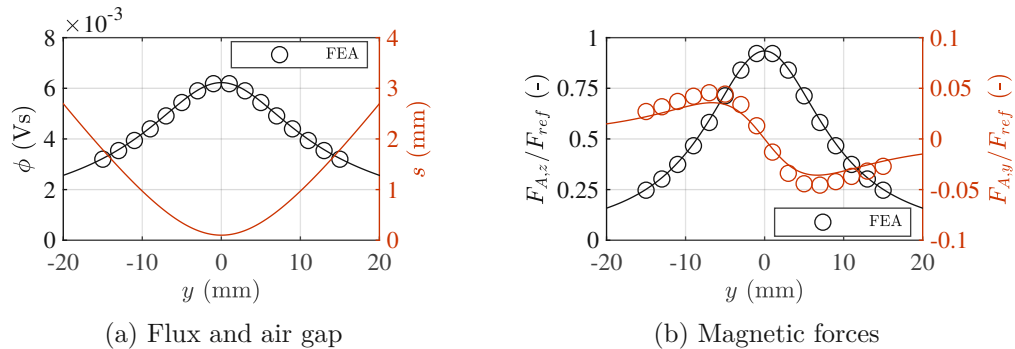


Figure 3.9: Function fit and finite element results

3.2.2 Magnetic submodel for multibody dynamics simulation

For the multibody dynamics model, a distribution of magnetic forces for each of the four brake magnets ($j = A, B, C, D$) along their longitudinal axis is considered. It is assumed that the magnetic forces are concentrated in the endpieces only. The magnetic network model consists of two parallel magnetic circuits which, as in Section 3.2.1, consist of a constant reluctance $R_{m,fe}$ for the iron parts and variable reluctances $R_{m,ls,j1}$ and $R_{m,ls,j2}$ as well as eddy current loss elements $L_{m,j1}$ and $L_{m,j2}$, Figure 3.10.

The coil of brake magnet j with the current i_j excites two parallel magnetic circuits, with the magnetic fluxes ϕ_{j1} and ϕ_{j2} and the combined flux $\phi_j = \phi_{j1} + \phi_{j2}$.

One magnetic circuit jk (with $k = 1, 2$) is represented by (3.15) with the same structure as (3.9) of the linear system model.

$$i_j N = \phi_{jk} (R_{m,fe} + R_{m,ls}(y_{jk}, z_{jk})) + G \dot{\phi}_{jk} \quad (3.15)$$

Since the multibody dynamics model considers lateral but also vertical displacements, the air gap is dependent on y and z . The magnetic forces are then calculated by (3.16) and (3.17), with vacuum permeability μ_0 and magnetic cross-section A .

$$F_{A,A1,y}(\phi_{A1}, y_{A1}, z_{A1}) = \frac{\phi_{A1}^2}{2\mu_0 A} \frac{\partial s_{A1}}{\partial y_{A1}}(y_{A1}, z_{A1}) \quad (3.16)$$

$$F_{A,A1,z}(\phi_{A1}, y_{A1}, z_{A1}) = \frac{\phi_{A1}^2}{2\mu_0 A} \frac{\partial s_{A1}}{\partial z_{A1}}(y_{A1}, z_{A1}) \quad (3.17)$$

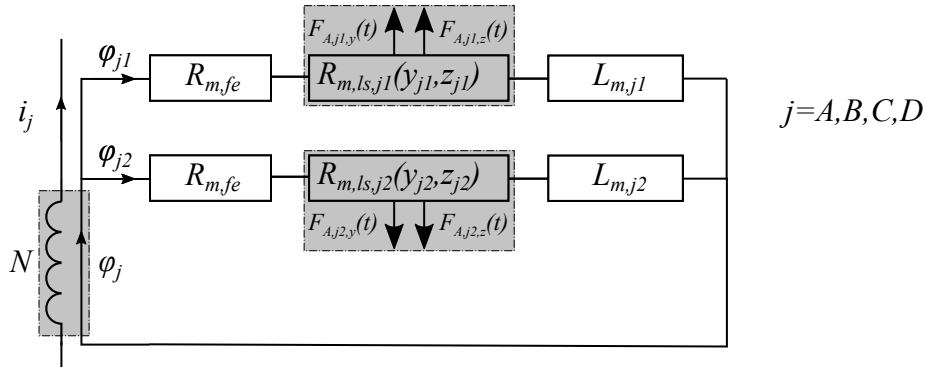


Figure 3.10: Magnetic network model of the multibody dynamics model

3.3 Electrical submodels of the track brake

Magnetic track brakes are electrically supplied by the battery of the vehicle. In the track brake described, two diagonally positioned magnets ($A+D$ and $B+C$) are connected in series. The two pairs are then connected in parallel to the supply voltage. A brake control unit activates the track brake by applying the voltage from the battery to the track brake.

The mathematical models of the magnetic track brake discussed in this thesis contain one, two or four electromagnets. With each multiplication of the number of magnets, the possibilities of parallel and/or in series connection arise – the influence of the type of electrical connection on the system behaviour is investigated in the following Chapter 4 using the electrical submodels presented below.

3.3.1 Electrical submodel for linear system analysis

For the linear system analysis, one coil is considered for the single magnet model and two for the double-magnet model. The electric system of the single magnet model consists of the voltage source u_{src} , an electrical resistance R_{el} and the coil with the number of windings N , see Figure 3.11.

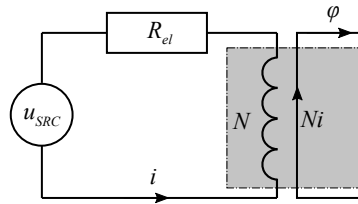


Figure 3.11: Electric single magnet model

The electrical system is described using Kirchhoff's law and Faraday's law:

$$u_{src} = R_{el}i + N\dot{\phi} \quad (3.18)$$

For the double-magnet model, the electrical system is expanded. The two coils of the double-magnet model are electrically connected either in series or in parallel, Figure 3.12 (a) and (b).

With the in series configuration, there are two coils in one loop. The electrical resistance doubles to $2R_{el}$. To generate the same electric current i as in the single magnet model, the source voltage is doubled as well to $2u_{src}$. In (3.19), the derivatives of the magnetic fluxes of both magnets A and B appear - the two magnetic fluxes are coupled over the electric circuit.

$$2u_{src} = i_{AB}2R_{el} + N(\dot{\phi}_A + \dot{\phi}_B) \quad (3.19)$$

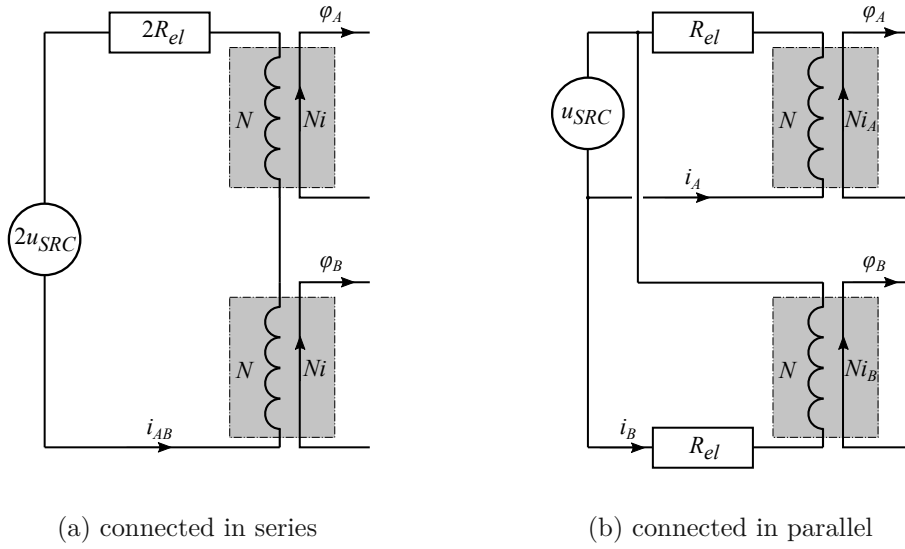


Figure 3.12: Electric double-magnet models

The circuit of the electrical submodel for the in parallel configuration is described by (3.20) to (3.21). It is noted that here the derivatives of the magnetic fluxes from the circuits connected in parallel do not appear.

$$u_{src} = i_A R_{el} + N \dot{\phi}_A \quad (3.20)$$

$$u_{src} = i_B R_{el} + N \dot{\phi}_B \quad (3.21)$$

3.3.2 Electrical submodel for multibody dynamics simulation

The electrical submodel for the multibody dynamics model corresponds to the circuit of the real magnetic track brake, Figure 3.13. The electric source voltage u_{src} supplies two parallel circuits whereas the diagonally located electromagnets $A+D$ and $B+C$ are connected in series, (3.22) and (3.23).

$$u_{src} = i_{AD} R_{el} + N(\dot{\phi}_{A1} + \dot{\phi}_{A2} + \dot{\phi}_{D1} + \dot{\phi}_{D2}) \quad (3.22)$$

$$u_{src} = i_{BC} R_{el} + N(\dot{\phi}_{B1} + \dot{\phi}_{B2} + \dot{\phi}_{C1} + \dot{\phi}_{C2}) \quad (3.23)$$

The time derivatives of the magnetic fluxes of the loops connected to each other in series appear in the equations. There follows that all magnetic fluxes in a loop are coupled over the electrical circuit.

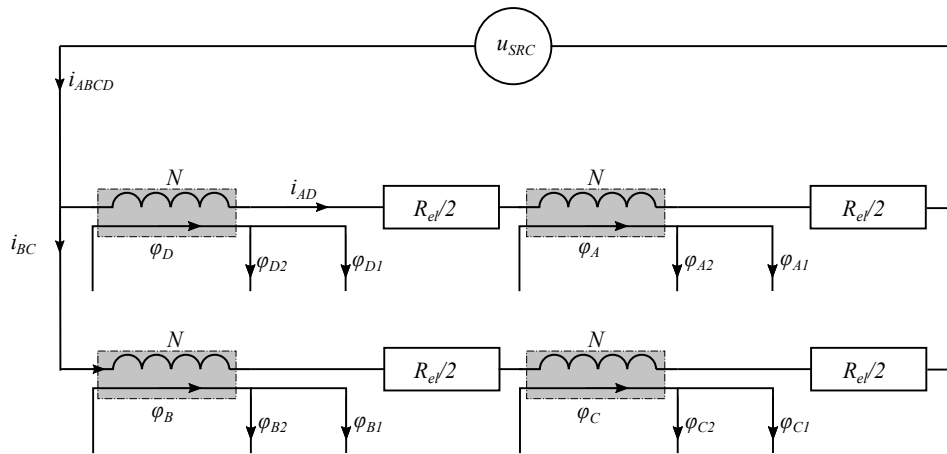


Figure 3.13: Electric circuit for the multibody dynamics model

3.4 Coupled system models

From the mechanical, magnetic and electrical sub-models, three system models of the magnetic track brake are assembled for different research objectives.

3.4.1 Single-magnet system model

To create basic understanding, a minimal system model is assembled from the 1 DoF mechanical submodel from Section 3.1.1, the magnetic submodel presented in Section 3.2.1 and the electrical from Section 3.3.1. Figure 3.14 shows the schematic of the resulting coupled electro-magneto-mechanical system. The coil couples the electric and magnetic subsystems, whereas the magnetic and mechanical subsystems are coupled through the reluctance of the air-gap $R_{m,ls}$.

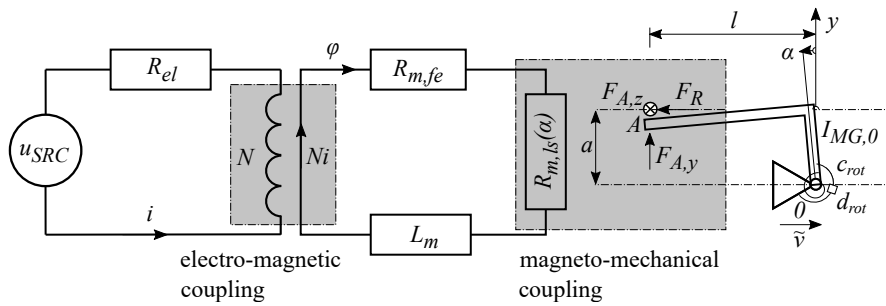


Figure 3.14: Coupled electro-magneto-mechanical system

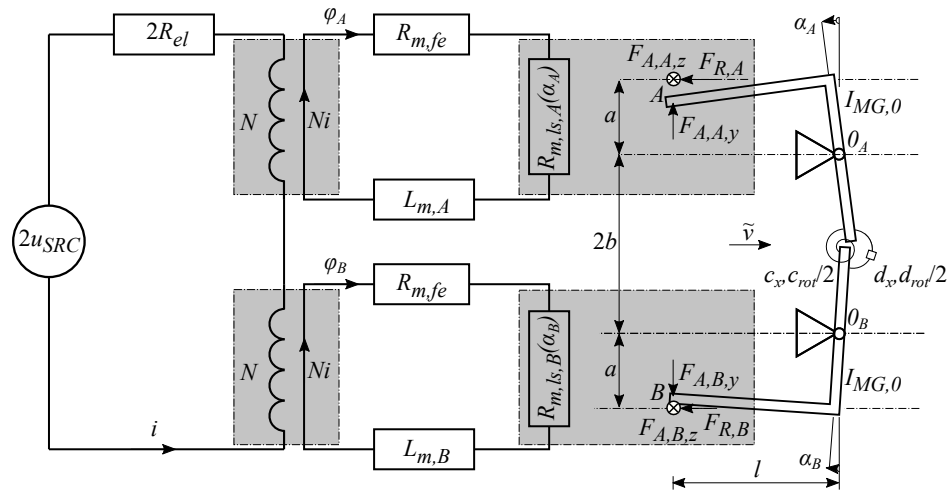
Assuming $y = l\alpha$ for small angles, the coupled non-linear system of equations (3.24)-(3.25) is obtained, by inserting (3.13) and (3.14) to (3.3) and by inserting (3.10) and (3.9) to (3.18).

$$I_{MG,0}\ddot{\alpha} + \left(d_{rot} + \frac{a^2 k_{\mu}}{\mu_0 A} \phi^2\right) \dot{\alpha} + c_{rot} \alpha = \left(\frac{a \tilde{\mu}_G}{2\mu_0 A} \frac{\partial s}{\partial z} - \frac{1}{2\mu_0 A} \frac{\partial s}{\partial \alpha}\right) \phi^2 \quad (3.24)$$

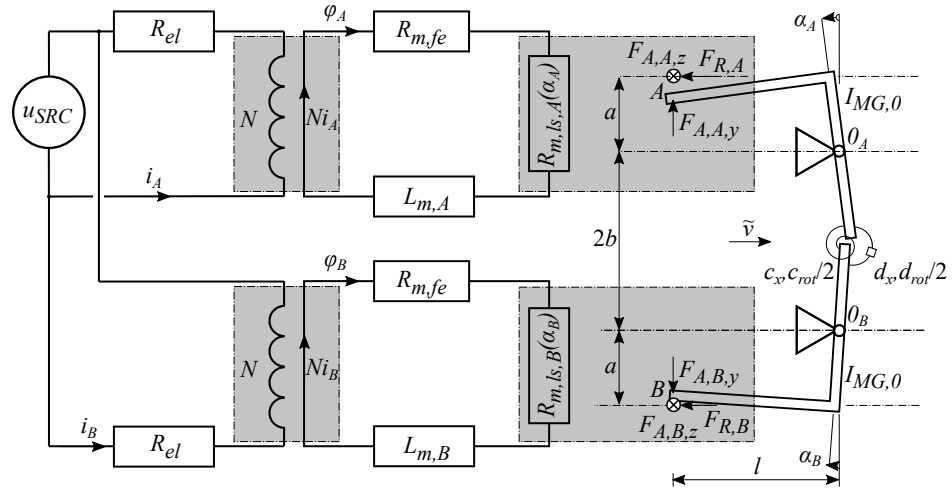
$$\left(\frac{N^2}{R_{el}} + G\right) \dot{\phi} + \left(R_{m,fe} + \underbrace{\frac{s(\alpha, z)}{\mu_0 A}}_{R_{m,ls}}\right) \phi = \frac{N}{R_{el}} u_{src} \quad (3.25)$$

3.4.2 Double-magnet system model

With the double-magnet model, symmetrical and asymmetrical oscillation modes are investigated, as well as the influence of the electrical connection of the magnets on the stability of the system. With the mechanical double-magnet submodel (Section 3.1.1), the magnetic submodel (Section 3.2.1) and the two electrical double-magnet submodels described in Section 3.3.1, two variants of the double-magnet system models are created, Figures 3.15(a) and 3.15(b).



(a) Electrically in series connected



(b) Electrically parallel connected

Figure 3.15: Double-magnet models

As each of the two magnets A and B has one mechanical degree of freedom, the resulting model has two mechanical DoFs α_A and α_B . The states of the magnetic circuits are

defined by the magnetic fluxes ϕ_A and ϕ_B . By inserting (3.13) and (3.14) into (3.4) the mechanical system equation (3.26) for α_A of the double-magnet model is obtained for both electrical configurations. The system equation for α_B is equal, but, with interchanged indices A and B .

$$I_{MG,0}\ddot{\alpha}_A + \frac{a^2 k_\mu}{\mu_0 A} \phi_A^2 \dot{\alpha}_A + \frac{d_{rot}}{2} (\dot{\alpha}_A + \dot{\alpha}_B) + d_x b^2 (\dot{\alpha}_A - \dot{\alpha}_B) + \frac{c_{rot}}{2} (\alpha_A + \alpha_B) + c_x b^2 (\alpha_A - \alpha_B) = \left(\frac{a \tilde{\mu}_G}{2 \mu_0 A} \frac{\partial s_A(\alpha_A, z)}{\partial z} - \frac{1}{2 \mu_0 A} \frac{\partial s_A(\alpha_A, z)}{\partial \alpha_A} \right) \phi_A^2 \quad (3.26)$$

Inserting (3.10) and (3.9) to (3.19) yields the electro-magnetic system equation of ϕ_A (3.19) for the in series configuration. Again, the system equation for ϕ_B is equal, but, with interchanged indices A and B .

$$\dot{\phi}_A \left(\frac{N^2}{R_{el}} + G \right) + \phi_A \left(\frac{N^2}{2GR_{el}} + 1 \right) \left(R_{m,fe} + \frac{s_A(\alpha_A, z)}{\mu_0 A} \right) - \underbrace{\phi_B \frac{N^2}{2GR_{el}} \left(R_{m,fe} + \frac{s_B(\alpha_B, z)}{\mu_0 A} \right)}_{\text{cross-coupling of } \phi_B} = \frac{N}{R_{el}} u_{src} \quad (3.27)$$

The magnetic fluxes ϕ_A and ϕ_B are coupled as ϕ_B appears in (3.27).

Inserting (3.10) and (3.9) to (3.20) yields the electro-magnetic system equation of ϕ_A (3.28) for the in parallel configuration.

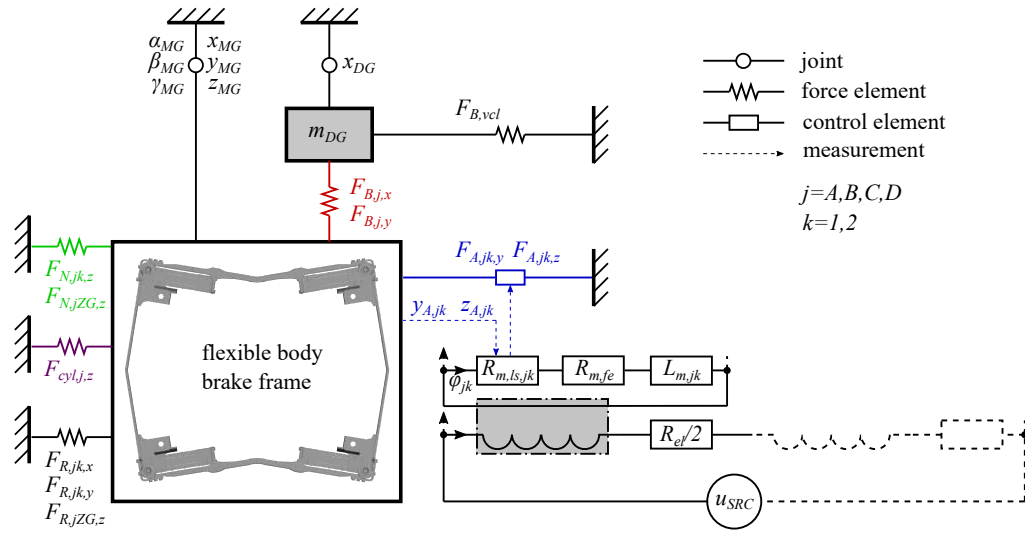
$$\dot{\phi}_A \left(\frac{N^2}{R_{el}} + G \right) + \phi_A \left(R_{m,fe} + \frac{s_A(\alpha_A, z)}{\mu_0 A} \right) = \frac{N}{R_{el}} u_{src} \quad (3.28)$$

In the parallel connected configuration no cross-coupling of the two magnetic fluxes is present. (3.28) is identical to the electromagnetic system equation of the single magnet model (3.25).

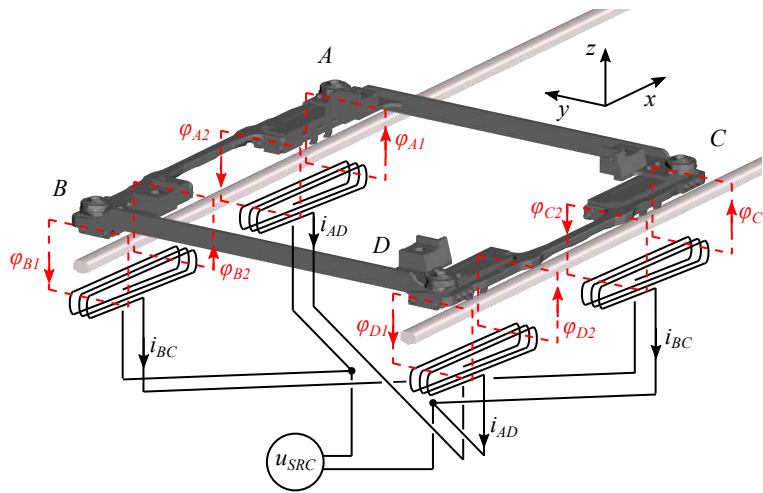
3.4.3 Multibody dynamics model

The multibody dynamics model of the track brake is assembled from the mechanical, magnetic and electrical submodels described in Sections 3.1.2, 3.2.2 and 3.3.2. Figure 3.16(a) shows a schematic of the model tree in SIMPACK with the bogie as a rigid body with mass m_{DG} and the brake frame as a flexible body. The force elements defined between the bodies and the inertial system are depicted. The positions of the brake frame fixed end pieces are transferred to the magnetic sub-model for the calculation of the magnetic forces which are transferred to the structure by control elements. The electrical and magnetic submodels are calculated internally in SIMPACK by means of algebraic expressions and numerical integration.

Figure 3.16(b) shows the electrical connection of the two pairs of diagonal in series connected magnets ($A + D$ and $B + C$). The pairs are then connected in parallel to the source voltage u_{src} . One coil per corner excites two magnetic circuits with the magnetic fluxes $\phi_{j,k}$ with $j = A, B, C, D$ and $k = 1, 2$.



(a) schematic of the model



(b) electrical connection

Figure 3.16: Multibody dynamics model

Linear stability analysis of a magnetic track brake

This chapter investigates mechanisms that can lead to self-excited vibrations of a magnetic track brake. The measurement results presented in Chapter 2 indicate that the vibrations consistently occur at low speeds, but the reason for their occurrence is yet unexplored.

With the simplified system models described in Chapter 3, analytical models of the magnetic track brake are available in order to investigate this question with the help of established methods of linear stability analysis. In order to find out which model parameters have a "stabilising" or self-exciting effect; the stability limit is examined with the linearised single magnet model using the Hurwitz criterion. It is of particular interest to find parameters that can be influenced by design in order to subsequently develop vibration-preventing magnetic track brakes. Closely linked to the reason for the development of vibrations is the question where the energy comes from to maintain the vibrations. For this purpose, the energy balance is calculated for the simplified (non-linear) model in its limit cycle.

Finally, the results with the single-magnet model are compared with the double-magnet model to investigate the influence of the electrical circuit on the stability behaviour.

4.1 Linearisation and stability border

To determine the stability border of the single magnet system model (3.24) and (3.25), the Hurwitz criterion [15] is applied to the linearised system. With $\ddot{\alpha} = \dot{\alpha} = \dot{\phi} = 0$, a steady state for linearisation $\alpha = \tilde{\alpha}$ and $\phi = \tilde{\phi}$ is derived numerically from

$$c_{rot}\tilde{\alpha} = \tilde{\phi}^2 a_{\tilde{\mu}G} \frac{1}{\mu_0 A} - \tilde{\phi}^2 \frac{1}{2\mu_0 A} \frac{\partial s}{\partial \alpha}(\tilde{\alpha}, \tilde{\phi}) \quad (4.1)$$

$$\tilde{\phi} \left(R_{m,fe} + \frac{s(\tilde{\alpha}, \tilde{\phi})}{\mu_0 A} \right) = \frac{N}{R_{el}} \tilde{u}_{src} \quad (4.2)$$

A linear 1.5 DoF system results due to the coupling of a second-order with a first-order system. The system matrix \mathbf{A} of the state-space representation $\dot{\mathbf{x}} = \mathbf{A}\mathbf{x} + \mathbf{b}u$ is established, with $\mathbf{x} = [\Delta\alpha \ \Delta\dot{\alpha} \ \Delta\phi]^T$, input vector \mathbf{b} and the input $u = \Delta u_{src}$. Here, the variations of the state variables around the equilibrium state are prefixed with Δ , e.g. $\Delta\alpha = \alpha - \tilde{\alpha}$.

$$\mathbf{A} = \begin{bmatrix} 0 & 1 & 0 \\ -a_{21} & -a_{22} & -a_{23} \\ -a_{31} & 0 & -a_{33} \end{bmatrix}, \quad \mathbf{b} = \begin{bmatrix} 0 \\ 0 \\ b_3 \end{bmatrix} \quad (4.3)$$

The derived system is similar to the auto-oscillation systems with inertial self-excitation described by Babitsky and Landa [24]. The coefficients a_{ij} and b_i are determined as:

$$\text{stiffness term:} \quad a_{21} = \frac{c_{rot} + \frac{\tilde{\phi}^2}{2\mu_0 A} \frac{\partial^2 s}{\partial \alpha^2} \Big|_0}{I_{MG,0}} > 0 \quad (4.4)$$

$$\text{damping term:} \quad a_{22} = \frac{d_{rot} + \frac{\tilde{\phi}^2 a^2 k_{\mu}}{\mu_0 A}}{I_{MG,0}} \leq 0 \quad (4.5)$$

$$\text{cross-coupling term:} \quad a_{23} = \frac{\frac{\tilde{\phi}}{\mu_0 A} \left(\frac{\partial s}{\partial \alpha} \Big|_0 - 2a_{\tilde{\mu}G} \right)}{I_{MG,0}} \leq 0 \quad (4.6)$$

$$\text{cross-coupling term:} \quad a_{31} = \frac{\frac{\tilde{\phi}}{\mu_0 A} \frac{\partial s}{\partial \alpha} \Big|_0}{\frac{N^2}{R_{el}} + G} > 0 \quad (4.7)$$

$$\text{inertia term:} \quad a_{33} = \frac{R_{m,fe} + \frac{s(\tilde{\alpha}, z_0)}{\mu_0 A}}{\frac{N^2}{R_{el}} + G} > 0 \quad (4.8)$$

$$\text{excitation term:} \quad b_3 = \frac{N}{R_{el}G + N^2} > 0 \quad (4.9)$$

From the factors of the stiffness term a_{21} , the cross-coupling term a_{31} , the inertia term a_{33} and the excitation term b_3 can be seen that these terms are always positive. However,

the damping term a_{22} may become negative:

$$a_{22} < 0 \quad \text{if} \quad d_{rot} < -\frac{\tilde{\phi}^2 a^2 k_\mu}{\mu_0 A} \quad (4.10)$$

Moreover, the cross-coupling term a_{23} may become negative as well:

$$a_{23} < 0 \quad \text{if} \quad \left. \frac{\partial s}{\partial \alpha} \right|_0 < 2a\tilde{\mu}_G \quad (4.11)$$

The linear system (4.3) is stable if all eigenvalues have negative real parts $\text{Re}(\lambda_i) < 0$ which is analysed next by applying first the Stodola criterion [15] and then the Hurwitz criterion. According to the Stodola criterion, for asymptotically stable system behaviour, the coefficients of the characteristic polynomial must be positive (1.7). The characteristic polynomial (4.12) is derived by $\det(\mathbf{A} - \lambda \mathbf{I}) = 0$:

$$\lambda^3 + \underbrace{(a_{22} + a_{33})}_{a_1 \leq 0} \lambda^2 + \underbrace{(a_{33}a_{22} + a_{21})}_{a_2 \leq 0} \lambda + \underbrace{a_{33}a_{21} - a_{31}a_{23}}_{a_3 \leq 0} = 0 \quad (4.12)$$

Depending on the coefficients of the system matrix (4.4) to (4.8) all three coefficients a_1 - a_3 of (4.12) may be either positive or negative.

To determine the stability border, the Hurwitz criterion is applied. Hurwitz matrix is obtained by inserting the coefficients of (4.12) to (1.8):

$$\mathbf{H} = \begin{bmatrix} a_1 & 1 & 0 \\ a_3 & a_2 & a_1 \\ 0 & 0 & a_3 \end{bmatrix} \quad (4.13)$$

with the main principal minors:

$$H_1 = a_1, \quad H_2 = \det \begin{bmatrix} a_1 & 1 \\ a_3 & a_2 \end{bmatrix} \quad (4.14)$$

The critical stability boundary is found, if

$$a_3 H_2 = 0. \quad (4.15)$$

If $a_3 = 0$, the monotone marginal stability is found. If $H_2 = 0$, the oscillatory marginal stability is found. The system is asymptotically stable if both criteria (4.16) and (4.17) are satisfied.

$$a_3 : \quad 0 < \quad a_{21}a_{33} \quad - \quad a_{23}a_{31} \quad (4.16)$$

$$H_2 : \quad 0 < \quad \underbrace{a_{23}a_{31}}_{\text{cross-coupling}} \quad + \quad \underbrace{a_{22}}_{\text{damping}} \quad (a_{21} + a_{22}a_{33} + a_{33}^2) \quad (4.17)$$

The system is oscillatory unstable if (4.17) becomes negative. The first addend is the product of the two cross-coupling terms $a_{23}a_{31}$, whereas the second one is determined by the damping term a_{22} . Thus, two mechanisms that may lead to self-excited vibrations can be identified. These are a negative product of the cross-coupling terms on the one hand and a negative damping term on the other hand.

The damping term becomes negative if condition (4.10) applies. This applies for large values of negative gradients of the friction characteristics k_μ . As a_{23} is always positive (4.6), the product of the cross-coupling terms is negative if condition (4.11) applies.

To determine the stability of steady states with respect to individual model parameters, further investigations are required. However, both the equilibrium conditions (4.1), (4.2) and the coefficients of the linearised system equations (4.4)-(4.8) are non-linear expressions of the model parameters. Therefore, analytical studies of the individual parameters do not appear to be practical. Numerical analysis of the terms will be performed in Section 4.2.

Special cases It has been shown that the stability of steady system states of the simplified model depends on the cross-coupling and on the derivative of the friction coefficient with respect to the relative sliding velocity. To study the two effects separately, two special cases are investigated.

Case 1: The electro-magnetic dynamical behaviour is neglected. Dynamic effects of the electromagnetic differential equation (3.25) is discarded by setting $(\frac{N^2}{R} + G) = 0$. As a result, (3.25) becomes an algebraic equation. Then, the moments due to the magnetic forces $M_{F,Ay}$ and $M_{F,Az}$ vary with $\Delta\alpha$ only. Thus, the magnetic forces correspond to the magneto-static forces as shown in Figure 3.9(b). The linear 1.5-DoF system degenerates to a second order 1-DoF system with the state-space representation $\dot{\mathbf{x}} = \mathbf{A}_{degen}\mathbf{x} + \mathbf{b}_{degen}u$, with $\mathbf{x} = [\Delta\alpha \ \Delta\dot{\alpha}]^T$ and:

$$\mathbf{A}_{degen} = \begin{bmatrix} 0 & 1 \\ -a_{21} + a_{23}\frac{a_{31}}{a_{33}} & -a_{22} \end{bmatrix}, \mathbf{b}_{degen} = \begin{bmatrix} 0 \\ -b_3\frac{a_{23}}{a_{33}} \end{bmatrix} \quad (4.18)$$

The system becomes unstable when a_{22} is negative. This is the case if condition (4.10) applies.

Case 2: Assuming $\mu_G = \text{const.}$, the derivative of the coefficient of friction with respect to the relative velocity vanishes $k_\mu = 0$ and as a result, $a_{22} > 0$ (4.5). The system still becomes oscillatory unstable for sufficiently large (negative) values of the product of the cross-coupling terms $a_{23}a_{31}$ (4.17).

4.2 Numerical stability analysis

To study the influence of individual model parameters, the stability of steady states of the simplified system (3.24)-(3.25) presented in Section 3.4.1 is explored further numerically. The aim is on the one hand to be able to predict self-excited vibrations depending on the model parameters and on the other hand to identify parameters that can be influenced by design to manipulate the stability behaviour.

With the model parameters from Table 4.1, the eigenvalues of the linearised system (4.3) are evaluated in the steady state (4.1)-(4.2). Three roots are found: one pure real eigenvalue λ_1 and one pair of conjugate complex eigenvalues $\lambda_{21}, \lambda_{22}$. Figure 4.1 shows the roots of the system in the complex plane. The real eigenvalue is negative whereas the conjugate complex pair has positive real parts. With the parameters chosen, the system therefore is unstable.

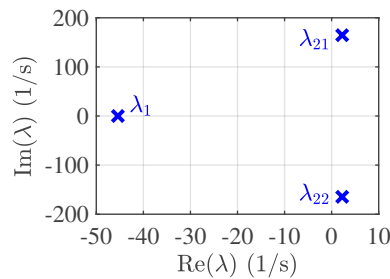


Figure 4.1: Roots of the linear system model

Important influencing variables that occur in the coefficients of the system matrix a_{ij} (4.4)-(4.8) are evaluated numerically. Assuming that the mechanical stiffness can be modified, the investigated variables are plotted as a function of the latter. Figure 4.2 shows the variables with respect to the relative stiffness $C_{rot} = c_{rot}/c_{rot,0}$. The damping ratio D of the mechanical system is assumed constant, therefore d_{rot} varies with c_{rot} (4.19). Here, ω_0 (4.20) is the undamped natural frequency of the mechanical sub-system.

$$d_{rot} = 2\omega_0 D \quad (4.19)$$

$$\omega_0 = \sqrt{\frac{c_{rot}}{I_{MG,0}}} \quad (4.20)$$

Figure 4.2 (a) and (b) show the steady state system variables $\tilde{\alpha}$ and $\tilde{\phi}$ with respect to C_{rot} . With increasing stiffness, the steady state deflection $\tilde{\alpha}$ decreases. As a result, the reluctance of the air-gap gets smaller and the magnetic flux $\tilde{\phi}$ increases slightly.

Diagram (c) and (d) depict the air-gap s and the variation of the air-gap with respect to the deflection $\frac{\partial s}{\partial \alpha}$. Due to the decrease in $\tilde{\alpha}$, the air-gap s closes. The air-gap influences

the inertia term a_{33} (4.8). The variation of the air-gap $\frac{\partial s}{\partial \alpha}$ is of great interest as it appears in both cross-coupling terms a_{23} and a_{31} . As seen, its value is positive and decreases with increasing stiffness.

Diagram (e) of Figure 4.2 shows the mechanical damping coefficient d_{rot} . As discussed before, the damping ratio D is held constant in this analysis. Therefore, d_{rot} increases with C_{rot} .

Diagram (f) shows the criterion for monotone stability (4.16) and Diagram (g) the criterion for oscillatory stability (4.17). (4.16) is > 0 for the whole parameter range and therefore the criterion for monotone stability is satisfied. The fulfilment of the criterion for oscillatory stability depends on the mechanical stiffness. (4.17) changes its sign with negative values for relative stiffnesses smaller than 1.64 and positive values above. The system can therefore be stabilised by increasing the stiffness.

Next, the coefficients of the linear system equations a_{ij} (4.4)-(4.8) are analysed along with the stability criteria (4.16) and (4.17). Figure 4.3 shows the coefficients as well as the addends of the monotone and oscillatory stability criteria with respect to C_{rot} . Diagram (a) shows that the stiffness term a_{21} increases with C_{rot} .

The damping term a_{22} (4.5) is plotted in Diagram (b). a_{22} increases with the relative stiffness as the damping ratio is held constant, see (4.19) and (4.20). For small values of $C_{rot} < 0.62$, a_{22} is negative due to the negative friction slope k_μ .

Diagram (c) and (d) show the cross-coupling terms a_{23} (4.6) and a_{31} which are of particular interest as their product occurs in both the criteria for monotone stability (4.16) and for oscillatory stability (4.17). For the parameters chosen, a_{23} is negative with increasing absolute value with increasing stiffness whereas a_{31} is positive and decreasing.

Figure 4.3(e) depicts the inertia term (4.8) which is approximately constant.

In Diagram (f) the products $a_{21}a_{33}$ and $-a_{23}a_{31}$ are plotted which are added in the criterion for monotone stability (4.16), Figure 4.2. As both addends are positive the criterion is satisfied.

Figure 4.3(g) shows the product $a_{23}a_{31}$ and the expression $a_{22}(a_{21} + a_{22}a_{33} + a_{33}^2)$ which are added in the criterion for oscillatory stability (4.17). The product of the cross-coupling terms $a_{23}a_{31}$ is negative which causes the criteria of oscillatory stability to fail for values of $C_{rot} < 1.64$, see Figure 4.2(g).

Stability maps It has been shown that the gradient of the coefficient of friction with respect to the sliding velocity k_μ is a key parameter occurring in the criterion of oscillatory stability (4.17). A high negative value of k_μ may cause the damping term a_{22} to vanish or even become negative, see (4.10). This is especially relevant for low velocities when friction coefficients steeply increase, see Figure 2.16. Next, the stability of steady states is analysed with respect to k_μ and additional parameters using stability maps, as shown in Figure 4.4. In the diagrams, the green area represents stable system behaviour, whereas

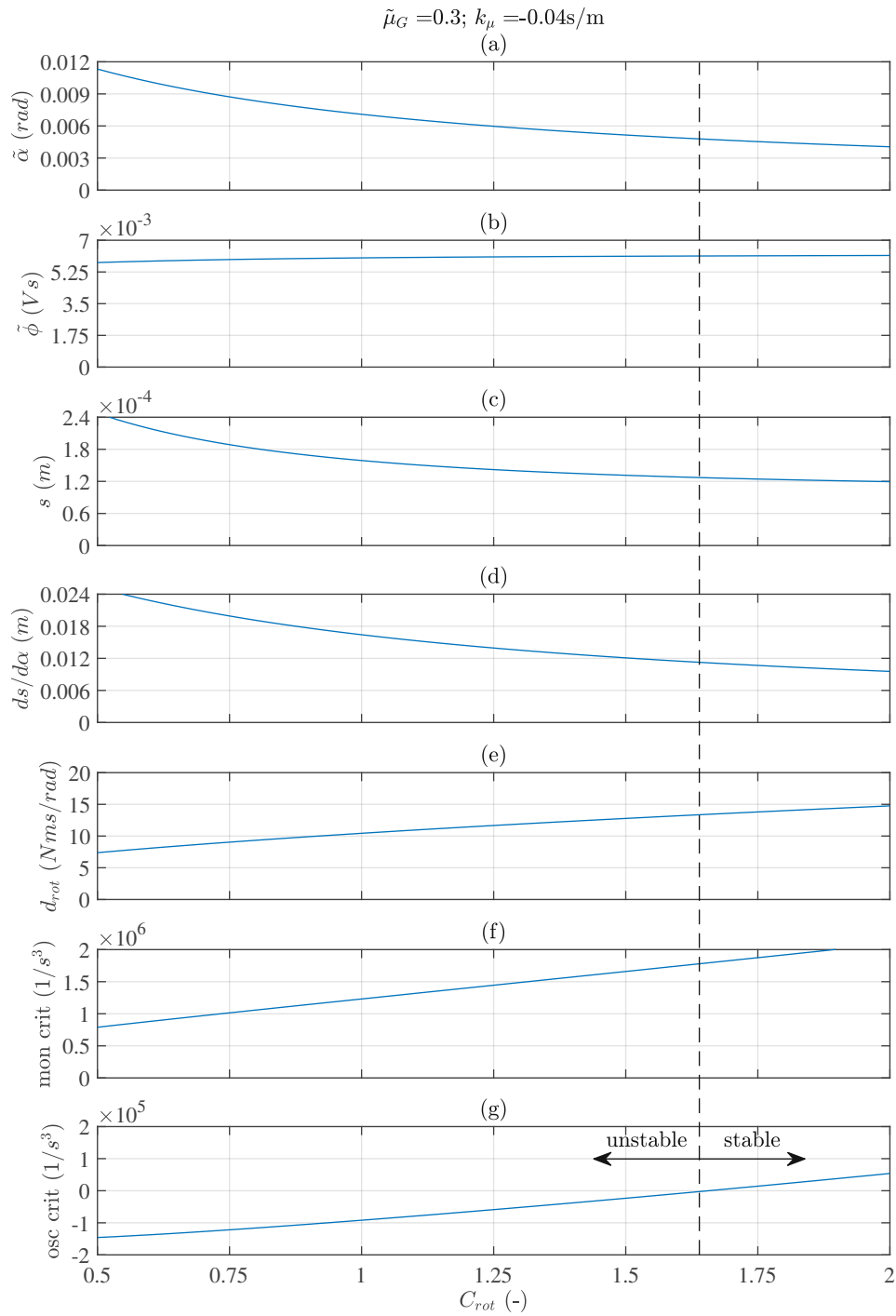


Figure 4.2: Influencing factors with respect to the relative stiffness

4. LINEAR STABILITY ANALYSIS OF A MAGNETIC TRACK BRAKE

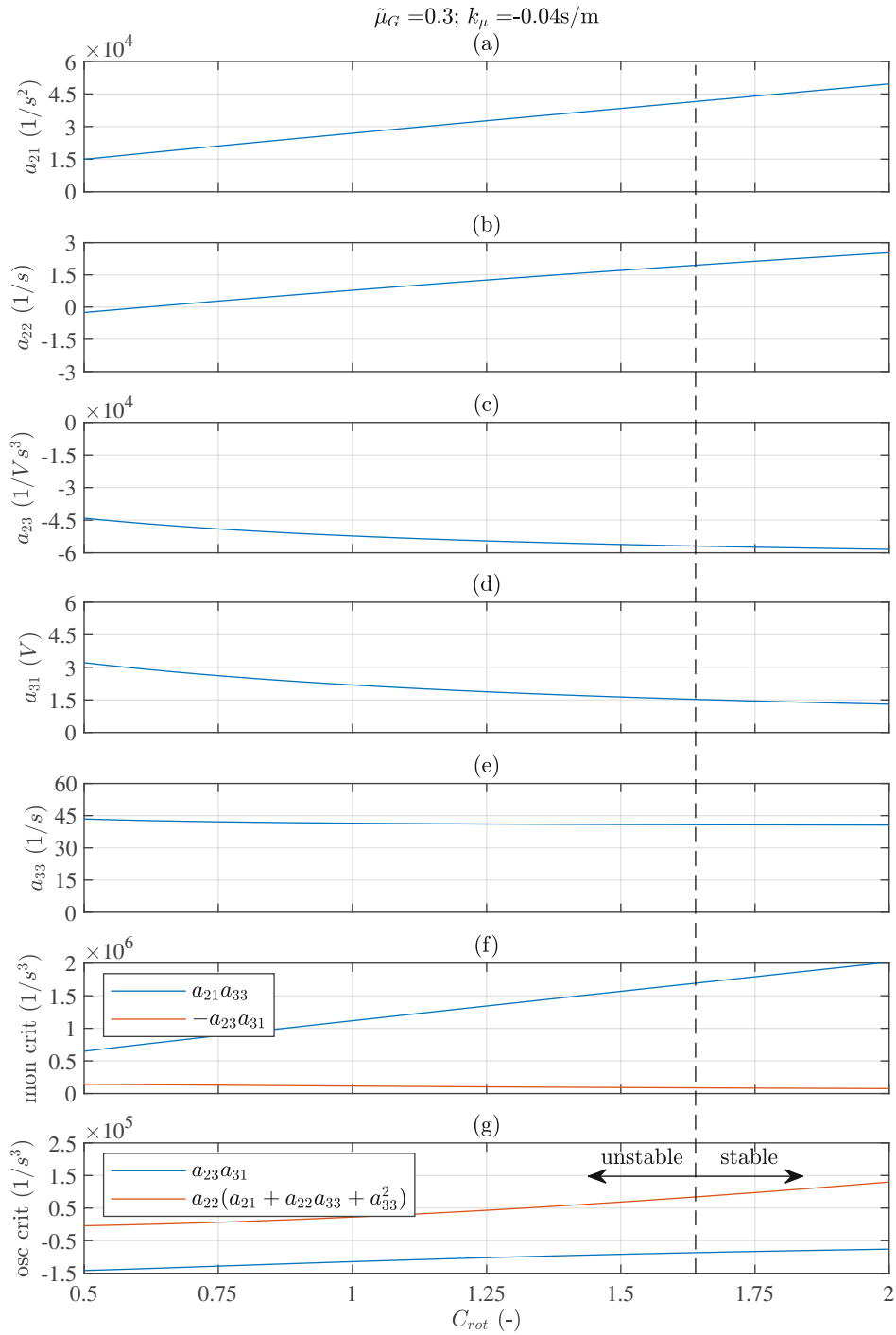


Figure 4.3: Coefficients a_{ij} and stability criteria with respect to the relative stiffness

the red area marks unstable behaviour. The continuous vertical line in the diagrams represents the standard values of the parameters as listed in Table 4.1.

Between k_μ and d_{rot} , a linear relationship can be observed, Figure 4.4(a). As expected, the stability map shows that small damping coefficients or negative values of friction slope may cause the stability criterion to fail.

Figure 4.4(b) shows the stability border with respect to k_μ and the relative stiffness. The system is stabilised by increasing the stiffness.

A strong non-linear behaviour is observed between the geometrical parameter l and k_μ , Figure 4.4(c). The longitudinal coordinate l defines the position of the contact point, Figure 3.4. In a vicinity of the standard value of l (see Table 4.1), a shift of the contact point closer to the rotation centre stabilises the system.

The parameter a defines the lateral distance of the rotation centre to the rail. Furthermore, the moment of inertia of the mechanical system $I_{MG,0}$ varies with a . Figure 4.4(d) shows that a small value of a stabilises the system.

Figure 4.4(e) shows the marginal stability with respect to the constant part of the coefficient of friction $\tilde{\mu}_G$. The cross-coupling coefficient a_{23} varies with $\tilde{\mu}_G$ (4.6). The diagram shows that both highly negative k_μ and also high values $\tilde{\mu}_G$ lead to unstable behaviour; for different reasons: As discussed, negative values of k_μ cause a reduction (or even negative values) of the damping term a_{22} (4.5), whereas high values of $\tilde{\mu}_G$ increase the cross-coupling effects.

In Diagram (e), the velocity dependent friction characteristics is plotted (dashed line), described by Cruceanu and Craciun [42]. At the beginning of a braking manoeuvre, μ_G and also the derivative with respect to the vehicle velocity $\frac{\partial \mu_G}{\partial v}$, start at a low level, see the left (stable) area of the diagram. During braking, μ_G increases and $\frac{\partial \mu_G}{\partial v}$ becomes more negative with decreasing velocity. The intersection point of the friction characteristics and the stability border marks the critical velocity where the system behaviour changes from stable to unstable.

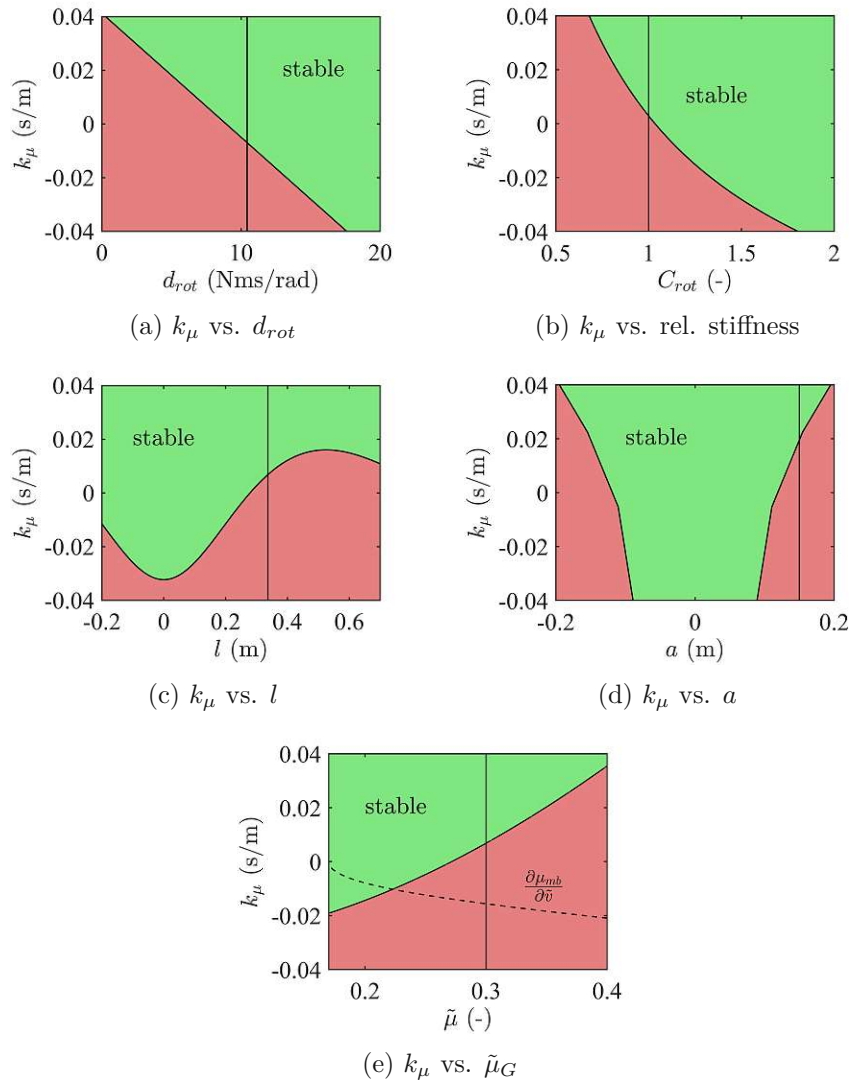


Figure 4.4: Stability maps

Parameter	Symbol (Unit)	Value
Eddy current loss factor	$G \left(\frac{1}{\Omega}\right)$	3000
Electric resistance	$R_{el} (\Omega)$	10
Number of windings	$N (-)$	300
Lateral distance	$a \text{ (m)}$	0.15
Friction gradient w.r.t. rel. vel.	$k_{\mu} \left(\frac{\text{s}}{\text{m}}\right)$	-0.02
Const. magnetic reluctance	$R_{m,0} \left(\frac{\text{A}}{\text{Vs}}\right)$	455000
Rotational spring constant	$c_{rot,0} \text{ (Nm/rad)}$	50000
Relative stiffness	$C_{rot} (-)$	1
Longitudinal distance	$l \text{ (m)}$	0.33667
Const. kinetic friction coefficient	$\tilde{\mu}_G (-)$	0.3
Coefficient of the magnetic air-gap model	$a_{hyp} \text{ (m)}$	0.0021
Coefficient of the magnetic air-gap model	$b_{hyp} \text{ (m)}$	0.01
Offset of the magnetic air-gap model	$a_{hyp,0} \text{ (m)}$	-0.002
Source voltage	$u_{src} \text{ (V)}$	100
Magnetic cross-section	$A \text{ (m}^2\text{)}$	0.003
Vacuum permeability	$\mu_0 \left(\frac{\text{N}}{\text{A}^2}\right)$	1.2566e-6
moment of inertia of the 1/4 track brake	$I_{MG,0} \text{ (kgm}^2\text{)}$	2.25
Damping ratio	$D (-)$	0.025
Const. velocity	$\tilde{v} \left(\frac{\text{m}}{\text{s}}\right)$	2

Table 4.1: Model parameters

4.3 Analysis in the time domain and energy considerations

The previous analyses have shown that the solutions of the linearised system can be oscillatory unstable. However, it is unclear how non-linear effects influence the vibration amplitudes of the state variables in a time series. Furthermore, it is of interest where energy is fed into the system to excite and maintain the vibrations.

In this section, time integrations are performed and discussed. The non-linear system equations (3.24)-(3.25) are implemented and solved in MATLAB/Simulink [56]. The mechanism of self-excitation is analysed in the time domain using simulated time signals of the state variables as well as system output variables. To illustrate the energy paths within the system, energy variables are calculated from the time signals and balanced over a period of a limit cycle.

4.3.1 Time integration results

A braking manoeuvre is simulated including the activation of the track brake by numerically solving the non-linear system equations (3.24)-(3.25) of the single magnet system model. The time integration starts at an initial state with no voltage applied $u_{src} = 0$ V and with all state variables equal to zero $\alpha = \dot{\alpha} = \phi = 0$. At $t = 0.3$ s, voltage is applied to the system.

Figure 4.5 shows variables of interest evaluated during time integration. Diagrams (a), (b) and (c) show the state variables α , $\dot{\alpha}$ and ϕ . Diagrams (d), (e) and (f) show the friction force F_R , the magnetic restoring force $F_{A,y}$ as well as the actual brake force $F_{B,x}$ in the bogie-track brake interface, Figure 4.9. Figure 4.5 (g) shows the electric current i .

After the track brake is activated, all variables shown in the diagrams increase and reach a quasi-static state. Then, oscillations evolve around the steady state and, after a section of rising amplitudes, the increase flattens until the system approaches a limit cycle.

The time frame of increasing amplitudes is of particular interest, as here the self-excitation mechanism becomes apparent by studying the state variables and forces involved, Figure 4.6. A phase shift between the state variables becomes visible with ϕ leading in phase with respect to α . The leading in phase is also observed in the friction force F_R which varies with the coefficient of friction and the magnetic attractive force $F_R = \mu_G(\dot{\alpha})F_{A,z}(\phi, \alpha)$. The phase shift of F_R with respect to α allows energy to be transferred from the friction contact to the oscillating system.

The magnetic restoring force $F_{A,y}$ is nearly in phase with α , Figure 4.6 (e).

Diagram (f), again, shows the actual brake force between the track brake and the bogie F_B . The oscillation amplitudes are large with respect to those of the friction force F_R . The signal is approximately in phase with α and therefore with the elastic deformation of the structure. Similar behaviour can be observed from the measurements of the field tests, see Figure 2.6. Bending moments measured at the longitudinal connector beams

$M_{V,j,z}$ and the track rods $M_{S,j,z}$ are proportional to the deflection of the structure. The brake forces $F_{B,j,x}$ are as well in phase with the bending moments.

In the last diagram, the oscillation of the current i is shown. The amplitudes are very small with respect to its steady state value which is also the case for the measurements in the vehicle tests.

Figure 4.7(a) shows a phase trajectory of the three state variables α , $\dot{\alpha}$ and ϕ . The diagrams show projections of the phase space in the $\dot{\alpha}-\phi$, $\alpha-\phi$ and $\alpha-\dot{\alpha}$ planes as well as a 3D view. The trajectory shows increasing amplitudes in all state variables after the electrical activation. In the diagrams, the phase shift between α and ϕ becomes even more apparent.

The trajectories approach a stable limit cycle which appears as a closed trajectory in the phase space diagrams, Figure 4.7(b). An equilibrium is reached between the energy fed into the system and the energy dissipated which is studied below.

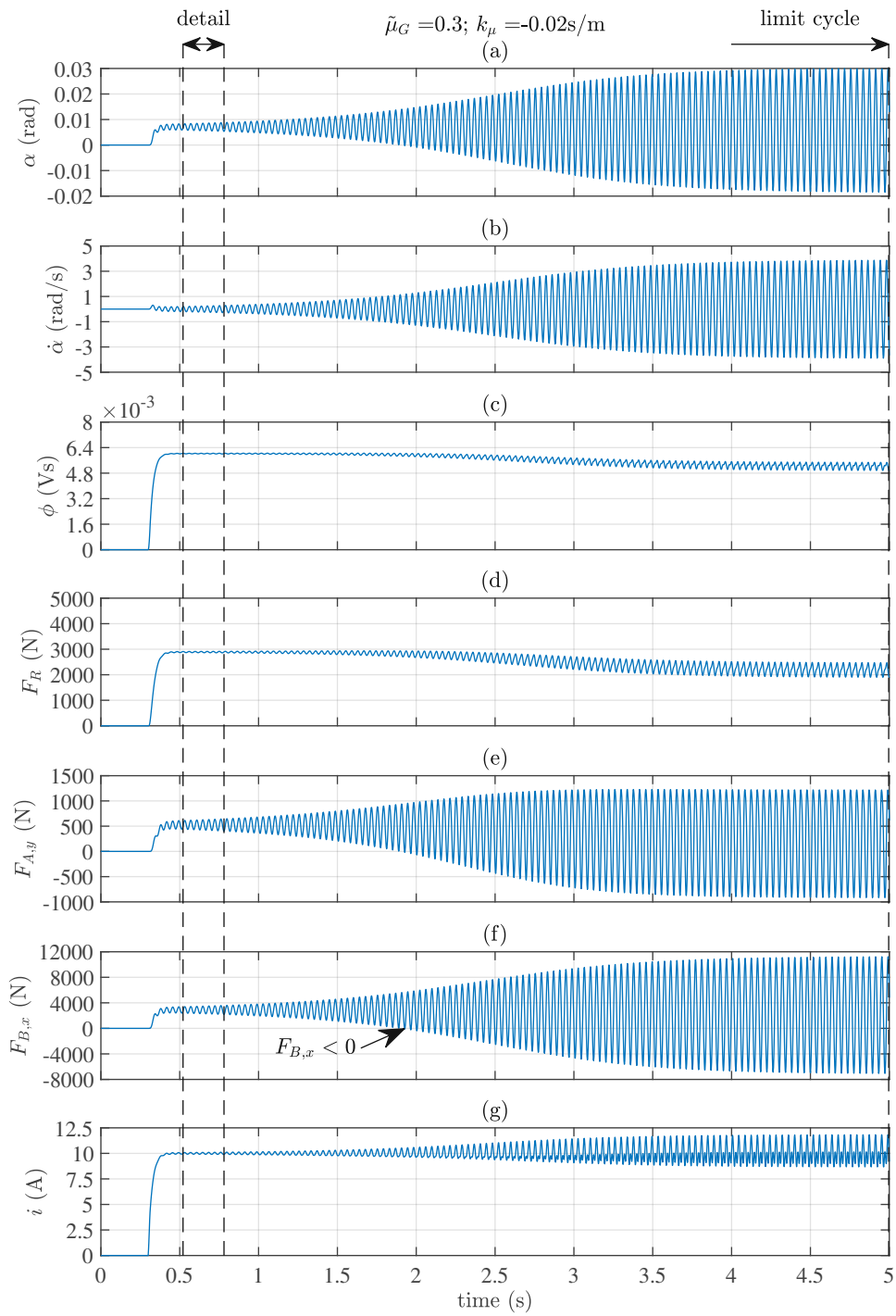


Figure 4.5: Time integration results of the linear model

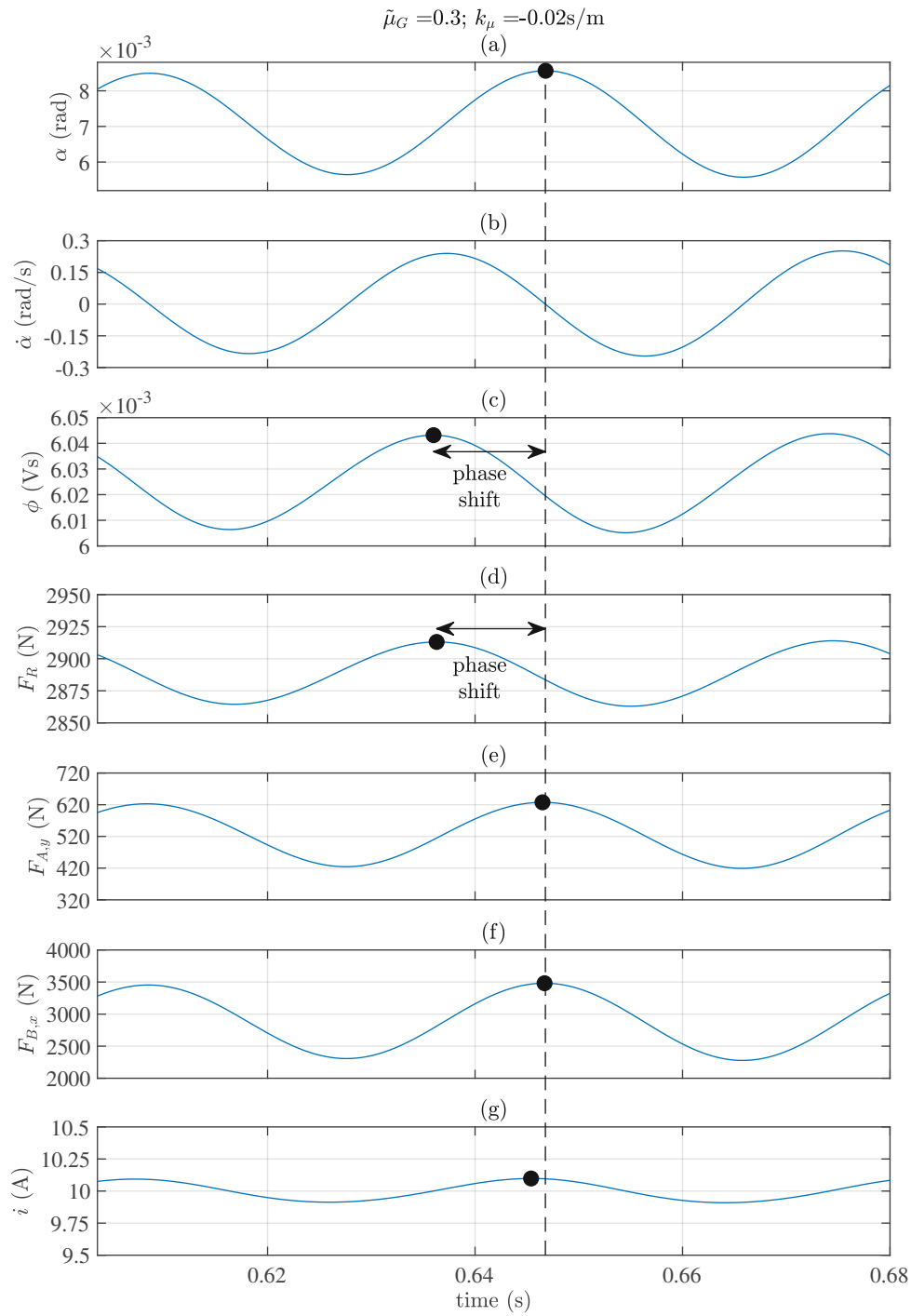
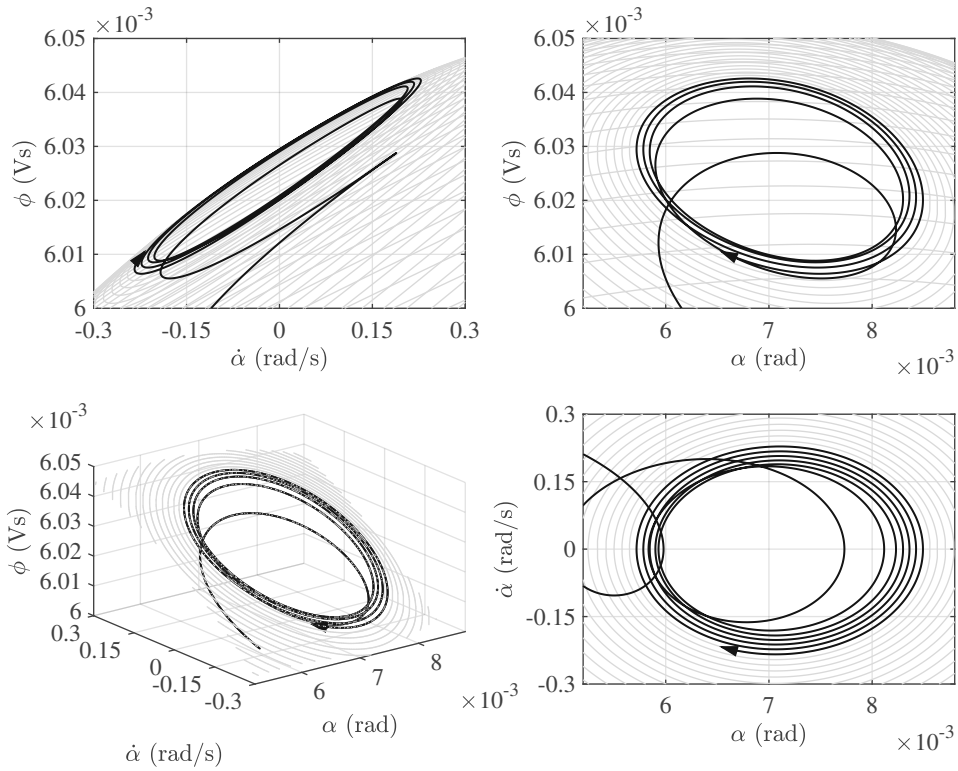
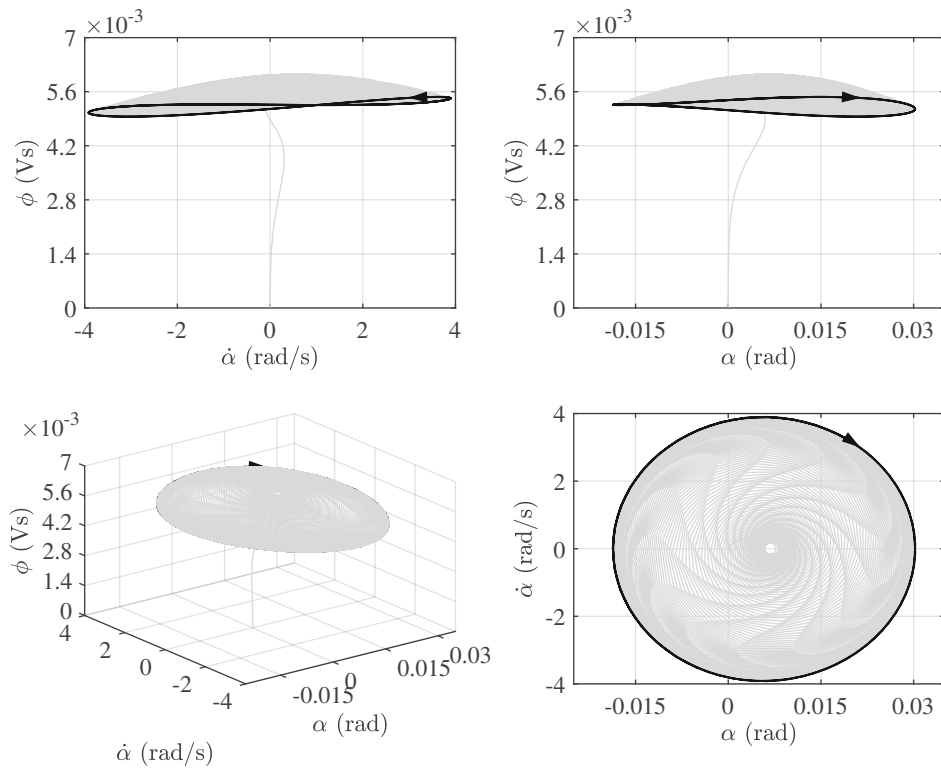


Figure 4.6: Detailed view on time integration results of the linear model



(a) increasing amplitudes



(b) limit cycle

Figure 4.7: Phase space trajectory of α , $\dot{\alpha}$ and ϕ

4.3.2 Energy balance of the limit cycle

The energy balance of a limit cycle is analysed to determine energy paths through the system. The system (3.24)-(3.25) consists of elements that either conserve energy, transfer energy between the subsystems or inject or dissipate energy through the system boundaries. Figure 4.8 shows an energy flow chart for the three subsystems.

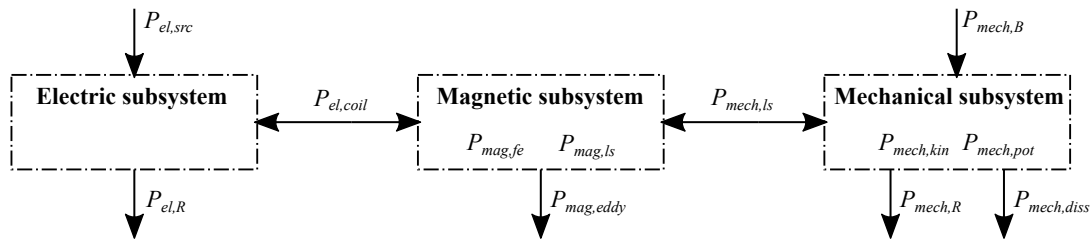


Figure 4.8: Energy flow in the coupled system

In the electric subsystem, electric energy is fed by the voltage source at the rate $P_{el,src}$ and is dissipated through the system boundary by the resistor at a rate of $P_{el,R}$. Moreover, energy can be transferred to the magnetic subsystem by the electro-magnetic converter at the rate $P_{el,coil}$.

In the magnetic subsystem, magnetic field energy is conserved by the magnetic reluctances of the steel parts and the air-gap. A change of magnetic field energy is indicated by $P_{mag,fe}$ and $P_{mag,ls}$. Further, energy is dissipated by the eddy current loss element at a rate of $P_{mag,eddy}$. Finally, mechanical work is performed inside the air-gap by the magnetic restoring force at a rate of $P_{mech,ls}$.

In the mechanical subsystem, power of the brake force $P_{mech,B}$ feeds mechanical energy to the system over time as the system is moved at a constant velocity \tilde{v} . Kinetic energy of the mass of the brake and potential energy of the rotational spring is conserved. Their energy flow rates are indicated by $P_{mech,kin}$ and $P_{mech,pot}$. Energy is dissipated by the friction force at a rate of $P_{mech,R}$ and the rotational damper at a rate of $P_{mech,diss}$.

Mechanical subsystem

The energy balance of the mechanical subsystem is analysed in greater detail. Figure 4.9 shows the free-body diagram of the mechanical system. As the rotational centre of the mechanical subsystem is driven by the velocity \tilde{v} , the external forces $F_{B,x}$ and F_R transfer energy by means of mechanical work through the system boundaries. The magnetic restoring force $F_{A,y}$ acts in the opening and closing directions of the air-gap. As a result, energy is transferred between the magnetic and the mechanical subsystems.

In the mechanical subsystem, energy is conserved in the form of kinetic energy of the track brake E_{kin} and potential energy of the rotational spring E_{pot} . The rotational damper d_{rot} dissipates energy from the mechanical subsystem. The magnetic attraction

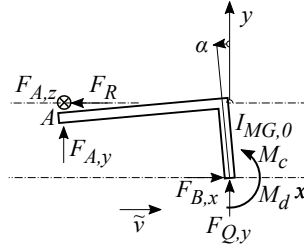


Figure 4.9: Free-body diagram of the mechanical system

force $F_{A,z}$ as well as the lateral transmission force $F_{Q,y}$ do not contribute to the energy balance.

The energy balance of the mechanical system over one period of the limit cycle τ is derived by the time integral over the power-energy equation (4.21).

$$\begin{aligned}
 0 = & \underbrace{\int_{\tau} P_{mech,B} dt}_{\Delta E_{mech,B}} + \underbrace{\int_{\tau} P_{mech,R} dt}_{\Delta E_{mech,R}} + \underbrace{\int_{\tau} P_{mech,ls} dt}_{\Delta E_{mech,ls}} + \underbrace{\int_{\tau} P_{mech,diss} dt}_{\Delta E_{mech,diss}} \\
 & + \underbrace{\int_{\tau} P_{mech,kin} dt}_{\Delta E_{kin}=0} + \underbrace{\int_{\tau} P_{mech,pot} dt}_{\Delta E_{pot}=0}
 \end{aligned} \quad (4.21)$$

Here, $P_{mech,B}$ represents the power of the transmitting force, $P_{mech,R}$ the power of the friction force, $P_{mech,ls}$ the power of the magnetic restoring force acting on the air-gap, $P_{mech,diss}$ the power of the rotational damping moment, $P_{mech,kin}$ the rate of kinetic energy of the mass and $P_{mech,pot}$ the potential energy rate of the rotational spring.

$$P_{mech,B} = \mathbf{F}_{B,x}^T \tilde{\mathbf{v}} = \begin{bmatrix} \mu_G F_A + am_{MG} \ddot{\alpha} & 0 & 0 \end{bmatrix} \begin{bmatrix} \tilde{v} \\ 0 \\ 0 \end{bmatrix} \quad (4.22)$$

$$P_{mech,R} = \mathbf{F}_R^T \mathbf{v}_{rel} = \begin{bmatrix} \mu_G F_A \ddot{\alpha} & 0 & 0 \end{bmatrix} \left(\begin{bmatrix} \tilde{v} \\ 0 \\ 0 \end{bmatrix} + \begin{bmatrix} 0 & -\dot{\alpha} & 0 \\ \dot{\alpha} & 0 & 0 \\ 0 & 0 & 0 \end{bmatrix} \begin{bmatrix} -l \\ a \\ 0 \end{bmatrix} \right) \quad (4.23)$$

$$P_{mech,ls} = \mathbf{F}_{A,y}^T \mathbf{v}_{A,rel} = \begin{bmatrix} 0 & -F_{A,y} & 0 \end{bmatrix} \begin{bmatrix} 0 & -\dot{\alpha} & 0 \\ \dot{\alpha} & 0 & 0 \\ 0 & 0 & 0 \end{bmatrix} \begin{bmatrix} -l \\ a - \alpha l \\ 0 \end{bmatrix} \quad (4.24)$$

$$P_{mech,diss} = d_{rot} \boldsymbol{\omega}^T \boldsymbol{\omega} = \begin{bmatrix} d_{rot} \dot{\alpha} & 0 & 0 \end{bmatrix} \begin{bmatrix} \dot{\alpha} \\ 0 \\ 0 \end{bmatrix} \quad (4.25)$$

For one period of the limit cycle τ , the change in kinetic ΔE_{pot} and potential energy ΔE_{pot} equals zero. Figure 4.10(a) shows the evaluated energy balance over τ from the time integration. On the left side, the energy is injected to the mechanical system, on the right side the energy dissipated and transferred to other subsystems. It can be seen that all the work injected to the mechanical system is provided by the transmission force $F_{B,x}$. Most of the energy is dissipated by the friction force F_R and the rotational damping moment $d_{rot}\dot{\alpha}$. However, Figure 4.10(b) shows that a small part of the mechanical work is transferred to the magnetic subsystem by the magnetic restoring force $F_{A,y}$.

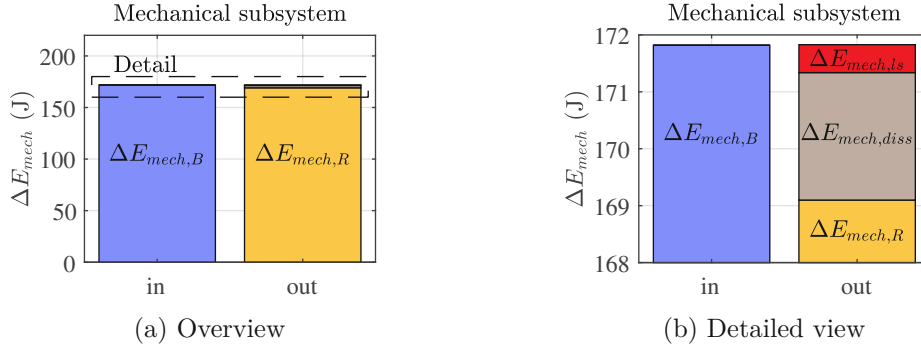


Figure 4.10: Energy balance of the mechanical subsystem for one period of the limit cycle

Magnetic subsystem

The magnetic reluctances of the iron core $R_{m,fe}$ and the air-gap $R_{m,ls}$ store energy by means of magnetic field energy. Further, mechanical work at the air-gap, produced by the restoring force $F_{A,y}$, causes a transfer of energy between the mechanical and the magnetic subsystems. Moreover, the coil acts as an energy converter between the electric and the magnetic systems. Finally, eddy current losses dissipate energy inside the magnetic circuit. The energy balance over one period of the limit cycle is derived by integration over τ of the electric power transferred by the coil $P_{el,coil}$, the derivatives of the magnetic field energy of the iron parts $P_{mag,fe}$ and the air-gap $P_{mag,ls}$, the power of the mechanical force in the air-gap $P_{mech,ls}$ and the power dissipated through eddy current losses $P_{mag,eddy}$:

$$0 = \underbrace{\int_{\tau} P_{el,coil} dt}_{\Delta E_{el,coil}} + \underbrace{\int_{\tau} P_{mag,fe} dt}_{\Delta E_{mag,fe}=0} + \underbrace{\int_{\tau} P_{mag,ls} dt}_{\Delta E_{mag,ls}=0} + \underbrace{\int_{\tau} P_{mech,ls} dt}_{\Delta E_{mech,ls}} + \underbrace{\int_{\tau} P_{mag,eddy} dt}_{\Delta E_{mag,eddy}} \quad (4.26)$$

with:

$$P_{el,coil} = Ni\dot{\phi} \quad (4.27)$$

$$P_{mag,fe} = \frac{d}{dt} E_{mag,fe} = \frac{d}{dt} \frac{R_{m,fe}}{2} \phi^2 = R_{m,0} \phi \dot{\phi} \quad (4.28)$$

$$P_{mag,ls} = \frac{d}{dt} E_{mag,ls} = \frac{d}{dt} \frac{R_{m,ls}}{2} \phi^2 = R_{m,ls} \phi \dot{\phi} \quad (4.29)$$

$$P_{mag,eddy} = G_{eddy} \dot{\phi}^2 \quad (4.30)$$

Over one period of a limit cycle, the change of the magnetic field energy over one period equals zero, $\Delta E_{mag,fe} = \Delta E_{mag,ls} = 0$, see (4.26). Figure 4.11 shows the energy balance of the injected and dissipated energies from the time integration. The mechanical force $F_{A,y}$ injects energy $\Delta E_{mech,ls}$ to the subsystem. One part is dissipated through eddy current losses $\Delta E_{mag,eddy}$ and another part transferred to the electrical subsystem through the coil $\Delta E_{el,coil}$.

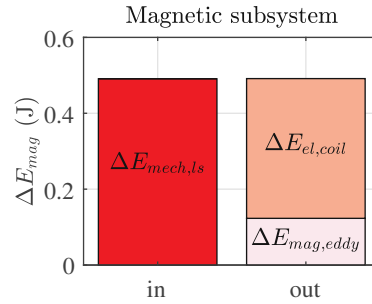


Figure 4.11: Energy balance of the magnetic subsystem for one period of the limit cycle

Electric subsystem

The electric subsystem includes a voltage source, a resistor and a coil which acts as an electromagnetic converter, Figure 3.8(b). The voltage source injects energy to the system and the resistor dissipates electric energy. As in the magnetic subsystem, the coil acts as an electro-magnetic converter. The energy balance for the limit cycle is derived by integrating the power balance over τ :

$$0 = \underbrace{\int_{\tau} P_{el,src} dt}_{\Delta E_{el,src}} + \underbrace{\int_{\tau} P_{el,R} dt}_{\Delta E_{el,R}} + \underbrace{\int_{\tau} P_{el,coil} dt}_{\Delta E_{el,coil}} \quad (4.31)$$

In (4.31), P_{src} equals the power induced by the voltage source, $P_{el,R}$ the power dissipated by the resistor and $P_{el,coil}$ the power transferred through the coil to or from the magnetic subsystem, see (4.32) to (4.27).

$$P_{el,src} = u_{src} i \quad (4.32)$$

$$P_{el,R} = R_{el}i^2 \quad (4.33)$$

Figure 4.12 shows the energy balance evaluated: Most of the energy injected to the electric subsystem is provided by the voltage source. However, in the limit cycle, a small amount of energy is transferred through the coil from the magnetic subsystem.

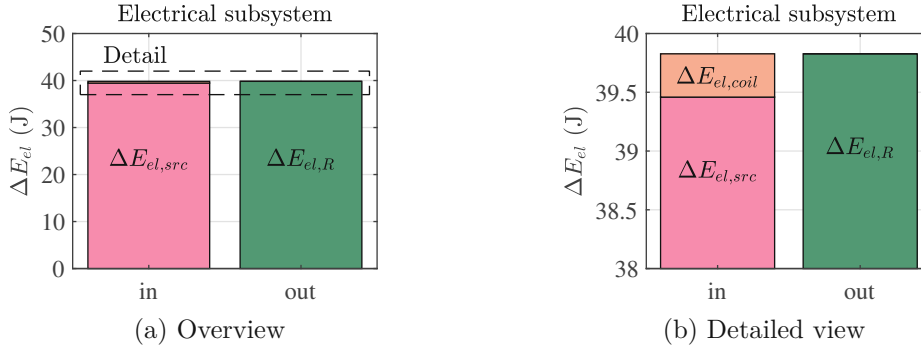


Figure 4.12: Energy balance of the electric subsystem for one period of the limit cycle

Coupled system

The energy balance of the full coupled model derives from the energy balances of the subsystems. Removing the zero energy terms in Equations (4.21), (4.26) and (4.31), the energy balance over one period of the limit cycle is obtained:

$$0 = \underbrace{\int_{\tau} P_{mech,B} dt}_{\Delta E_{mech,B}} + \underbrace{\int_{\tau} P_{mech,R} dt}_{\Delta E_{mech,R}} + \underbrace{\int_{\tau} P_{mech,diss} dt}_{\Delta E_{mech,diss}} + \underbrace{\int_{\tau} P_{mag,eddy} dt}_{\Delta E_{mag,eddy}} + \underbrace{\int_{\tau} P_{el,src} dt}_{\Delta E_{el,src}} + \underbrace{\int_{\tau} P_{el,R} dt}_{\Delta E_{el,R}} \quad (4.34)$$

Figure 4.13 shows the evaluated total energy injected and dissipated. Electric energy from the voltage source $\Delta E_{el,src}$ and mechanical work from the interfacing force between track brake and bogie $\Delta E_{mech,B}$ is injected to the system. Most of the energy is dissipated in the electric resistance $\Delta E_{el,R}$ and the mechanical friction $\Delta E_{mech,R}$. Small amounts of energy are as well dissipated through the rotational damper $\Delta E_{mech,diss}$ and the eddy currents $\Delta E_{mag,eddy}$.

Obviously, two energy sources maintain the self-excited vibrations of the model. On the one hand kinetic energy of the train: As long as the train is in motion, the interfacing force between the track brake and the bogie constantly feeds energy to the mechanical system through the system boundary. On the other hand, the electric voltage source continuously feeds the electric circuit. It is now quantifiable how energy that is fed into the system is dissipated or converted during a braking manoeuvre with self-excited vibrations.

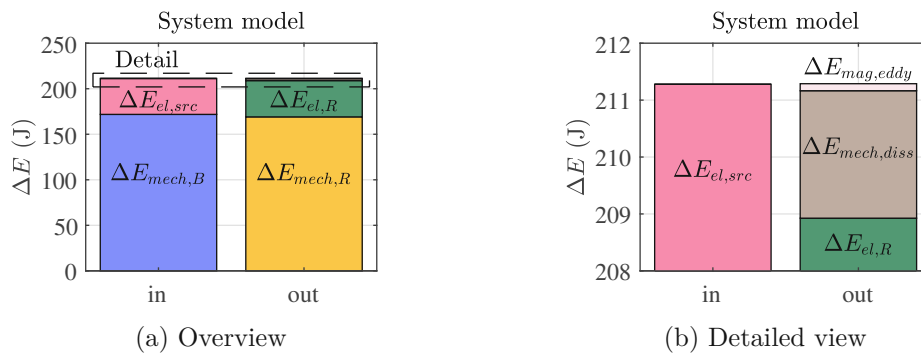


Figure 4.13: Energy balance of the coupled system model for one period of the limit cycle.

4.4 Linear analysis of the double-magnet model

To study the influence of the electrical connection of multiple magnets on the stability of the system, this section analyses the double-magnet model in two configurations: The electrical in series and in parallel connection. The models (3.26)-(3.27) and (3.26)-(3.28) are linearised at the steady state $[\alpha_A = \alpha_B = \tilde{\alpha}; \phi_A = \phi_B = \tilde{\phi}]^T$ and eigenvalues calculated with respect to stiffness parameters. For both configurations, stability criteria for steady system states are established and evaluated by applying the Hurwitz criterion.

The state space representation of the electrically in series connected double-magnet model is defined by $\dot{\mathbf{x}}_d = \mathbf{A}_{d,s}\mathbf{x}_d + \mathbf{b}_d u$ with the system matrix $\mathbf{A}_{d,s}$ (4.35), the state-vector \mathbf{x}_d and the input vector \mathbf{b}_d (4.36).

$$\mathbf{A}_{d,s} = \begin{bmatrix} 0 & 1 & 0 & 0 & 0 & 0 \\ -a_{21} + \frac{c_{rot} - 2c_x b^2}{2m_{MG} a^2} & -a_{22} + \frac{d_{rot} - 2d_x b^2}{2m_{MG} a^2} & -a_{23} & \frac{-c_{rot} + 2c_x b^2}{2m_{MG} a^2} & \frac{-d_{rot} + 2d_x b^2}{2m_{MG} a^2} & 0 \\ -a_{31}(1+e) & 0 & -a_{33}(1+e) & a_{31}e & 0 & a_{33}e \\ 0 & 0 & 0 & 0 & 1 & 0 \\ \frac{-c_{rot} + 2c_x b^2}{2m_{MG} a^2} & \frac{-d_{rot} + 2d_x b^2}{2m_{MG} a^2} & 0 & -a_{21} + \frac{c_{rot} - 2c_x b^2}{2m_{MG} a^2} & -a_{22} + \frac{d_{rot} - 2d_x b^2}{2m_{MG} a^2} & -a_{23} \\ a_{31}e & 0 & a_{33}e & -a_{31}(1+e) & 0 & -a_{33}(1+e) \end{bmatrix} \quad (4.35)$$

$$\mathbf{b}_d = \begin{bmatrix} 0 \\ 0 \\ b_3 \\ 0 \\ 0 \\ b_3 \end{bmatrix}; \quad \mathbf{x}_d = \begin{bmatrix} \Delta\alpha_A \\ \Delta\dot{\alpha}_A \\ \Delta\phi_A \\ \Delta\alpha_B \\ \Delta\dot{\alpha}_B \\ \Delta\phi_B \end{bmatrix} \quad (4.36)$$

The coefficients a_{ij} and b_i are identical to those of the single magnet model, (4.4)–(4.9). In (4.35), the magnetic fluxes $\Delta\phi_A$ and $\Delta\phi_B$ are coupled by the coefficient e (4.37).

$$e = \frac{N^2}{2GR_{el}} > 0 \quad (4.37)$$

The state space model $\dot{\mathbf{x}}_d = \mathbf{A}_{d,p}\mathbf{x}_d + \mathbf{b}_d u$ represents the linearised in parallel connected

system with the system matrix $\mathbf{A}_{d,p}$:

$$\mathbf{A}_{d,p} = \begin{bmatrix} 0 & 1 & 0 & 0 & 0 & 0 \\ -a_{21} + \frac{c_{rot} - 2c_x b^2}{2m_{MG}a^2} & -a_{22} + \frac{d_{rot} - 2d_x b^2}{2m_{MG}a^2} & -a_{23} & \frac{-c_{rot} + 2c_x b^2}{2m_{MG}a^2} & \frac{-d_{rot} + 2d_x b^2}{2m_{MG}a^2} & 0 \\ -a_{31} & 0 & -a_{33} & 0 & 0 & 0 \\ 0 & 0 & 0 & 0 & 1 & 0 \\ \frac{-c_{rot} + 2c_x b^2}{2m_{MG}a^2} & \frac{-d_{rot} + 2d_x b^2}{2m_{MG}a^2} & 0 & -a_{21} + \frac{c_{rot} - 2c_x b^2}{2m_{MG}a^2} & -a_{22} + \frac{d_{rot} - 2d_x b^2}{2m_{MG}a^2} & -a_{23} \\ 0 & 0 & 0 & -a_{31} & 0 & -a_{33} \end{bmatrix} \quad (4.38)$$

The system matrices $\mathbf{A}_{d,s}$ (4.35) and $\mathbf{A}_{d,p}$ (4.38) are identical except for the coupling coefficient e which does not appear in $\mathbf{A}_{d,p}$. Magnetic fluxes $\Delta\phi_A$ and $\Delta\phi_B$ are coupled for the in series configuration but not for the in parallel configuration.

Eigenvalues The eigenvalues λ_i of the two system matrices $\mathbf{A}_{d,s}$ and $\mathbf{A}_{d,p}$ are calculated with varying values of the asymmetrical stiffness $b^2 c_x$ (3.4). With $c_{rot} = \text{constant}$, the ratio of the asymmetrical and the symmetrical stiffnesses $2c_x b^2 / c_{rot}$ is varied between 0.5-2. Figures 4.14(a) and 4.14(c) show the root loci of the in series and the in parallel configurations. Both systems have two pure real negative eigenvalues (λ_1, λ_3) and two pairs of conjugate complex eigenvalues ($\lambda_{21,2}$ and $\lambda_{41,2}$). The associated mode shapes are symmetrical for $\lambda_{21,2}$ and asymmetrical for $\lambda_{41,2}$, Figure 4.15. The real parts of the conjugate complex eigenvalues $\text{Re}(\lambda_i)$ are shown in Figures 4.14(b) (in series) and 4.14(d) (in parallel). By connecting the magnets in series (instead of in parallel), the real parts of the eigenvalues with associated asymmetric eigenmodes are increased.

Stability The Hurwitz stability criterion is applied to the system matrices (4.35) and (4.38), assuming $2c_x b^2 / c_{rot} = 1$. For the electrically in series connected configuration, the decisive criteria (4.39) and (4.40) for stability are obtained. For the in parallel configuration, the criteria (4.41) and (4.42) are determined. Obviously, the stability criteria of the in parallel configuration may also be derived by setting the coupling coefficient e to zero. (4.41) and (4.42) are identical to the stability criteria of the single magnet (4.16) and (4.17).

in series:

$$0 < (2e + 1)(a_{21}a_{33} - a_{23}a_{31}) \quad (4.39)$$

$$0 < a_{23}a_{31} + a_{22}(a_{21} + a_{22}a_{33} + a_{33}^2) + 4a_{22}a_{33}^2 e^2 + (2a_{31}a_{23} + 2a_{22}^2 a_{33} + 4a_{22}a_{33}^2)e \quad (4.40)$$

in parallel:

$$0 < a_{21}a_{33} - a_{23}a_{31} \quad (4.41)$$

$$0 < a_{23}a_{31} + a_{22}(a_{21} + a_{22}a_{33} + a_{33}^2) \quad (4.42)$$

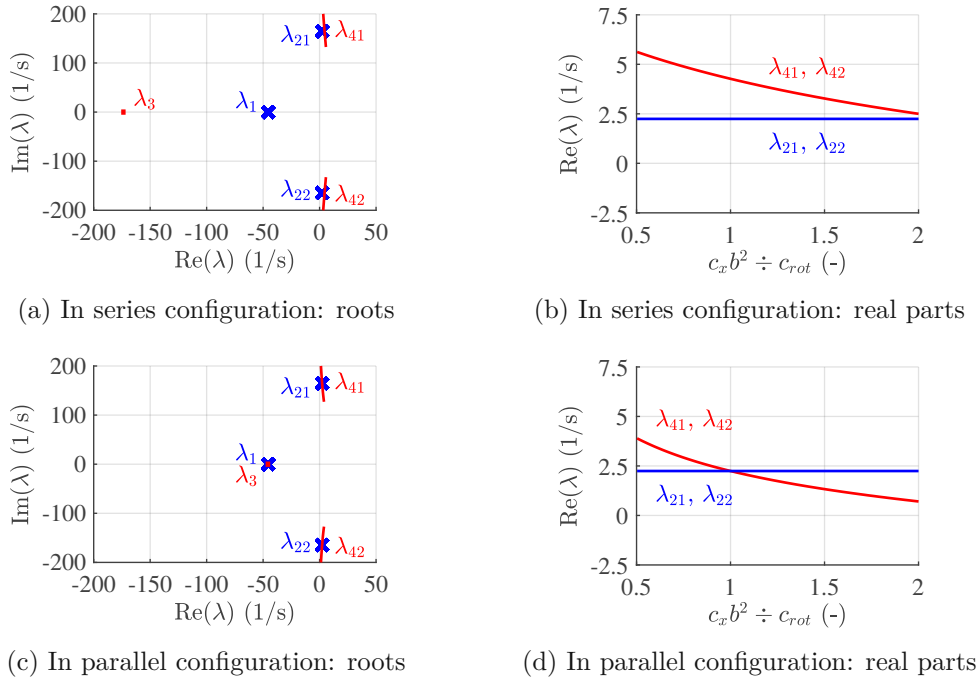


Figure 4.14: Eigenvalue analysis of the double-magnet model

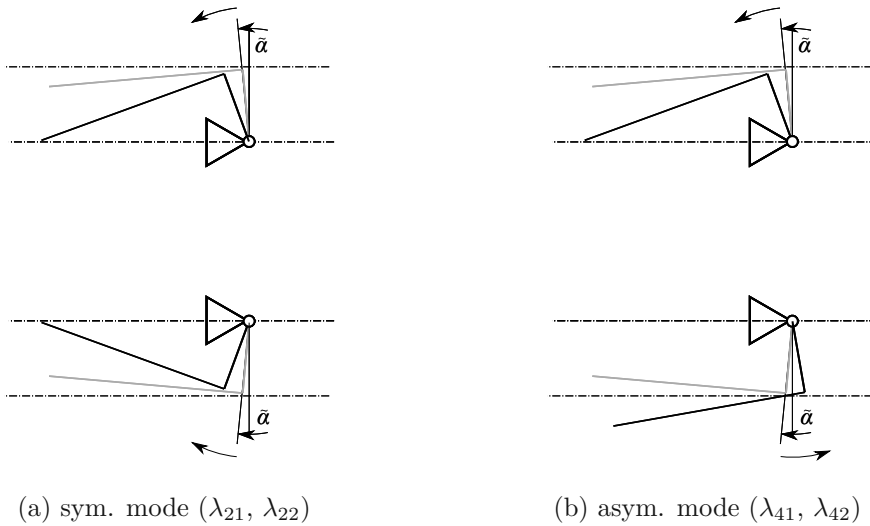


Figure 4.15: Eigenmodes corresponding to the complex eigenvalues

Similarly to Section 4.2, steady state system variables and stability criteria are further studied numerically with respect to the relative stiffness parameter C_{rot} . With $2c_x b^2 / c_{rot} = 1$, Figure 4.16 shows diagrams of the steady state values of $\tilde{\alpha}$ and $\tilde{\phi}$, the coupling coefficient e , real parts of the conjugate complex eigenvalues $\lambda_{21,2}$ and $\lambda_{41,2}$ as well as the criteria for oscillatory instability.

Diagrams (a) and (b) show the steady state variables $\tilde{\alpha}$ and $\tilde{\phi}$ which are identical to those of the single magnet model (Figure 4.3). Diagram (c) shows a constant value of the cross-coupling coefficient of the magnetic fluxes e .

Diagram (d) shows the real parts of the eigenvalues $\lambda_{21,2}$ (associated to the symmetrical mode) and $\lambda_{41,2}$ (associated to the asymmetrical mode) of both system matrices $\mathbf{A}_{d,s}$ (in series) and $\mathbf{A}_{d,p}$ (in parallel). The real parts of $\lambda_{21,2}$ of both matrices and of $\lambda_{41,2}$ of the in parallel configuration are identical with negative values for $C_{rot} > 1.66$. The real parts of $\lambda_{41,2}$ of the in series configuration are negative for $C_{rot} > 2.38$.

Diagram (e) shows the values of the right-hand sides of the inequalities of (4.40) for the in series configuration and of (4.42) for the in parallel configuration. For the parameter range analysed, the values for the in series configuration are smaller than those of the in parallel configuration. Both configurations may be stabilised by increasing the stiffness. However, a higher stiffness is required to stabilise the magnets connected in series ($C_{rot} > 2.38$) than to stabilise the magnets connected in parallel ($C_{red} > 1.66$).

The in series connection of the left and right magnets leads to a coupling of the two magnetic fluxes ϕ_A and ϕ_B . For the in parallel connection of the two magnets, this coupling is not present. In the asymmetric oscillatory mode, the coupling of fluxes reinforces the self-exciting mechanisms. As a result, the in series connection de-stabilises the asymmetric mode. For the symmetric oscillatory mode, the type of electrical connection is not relevant.

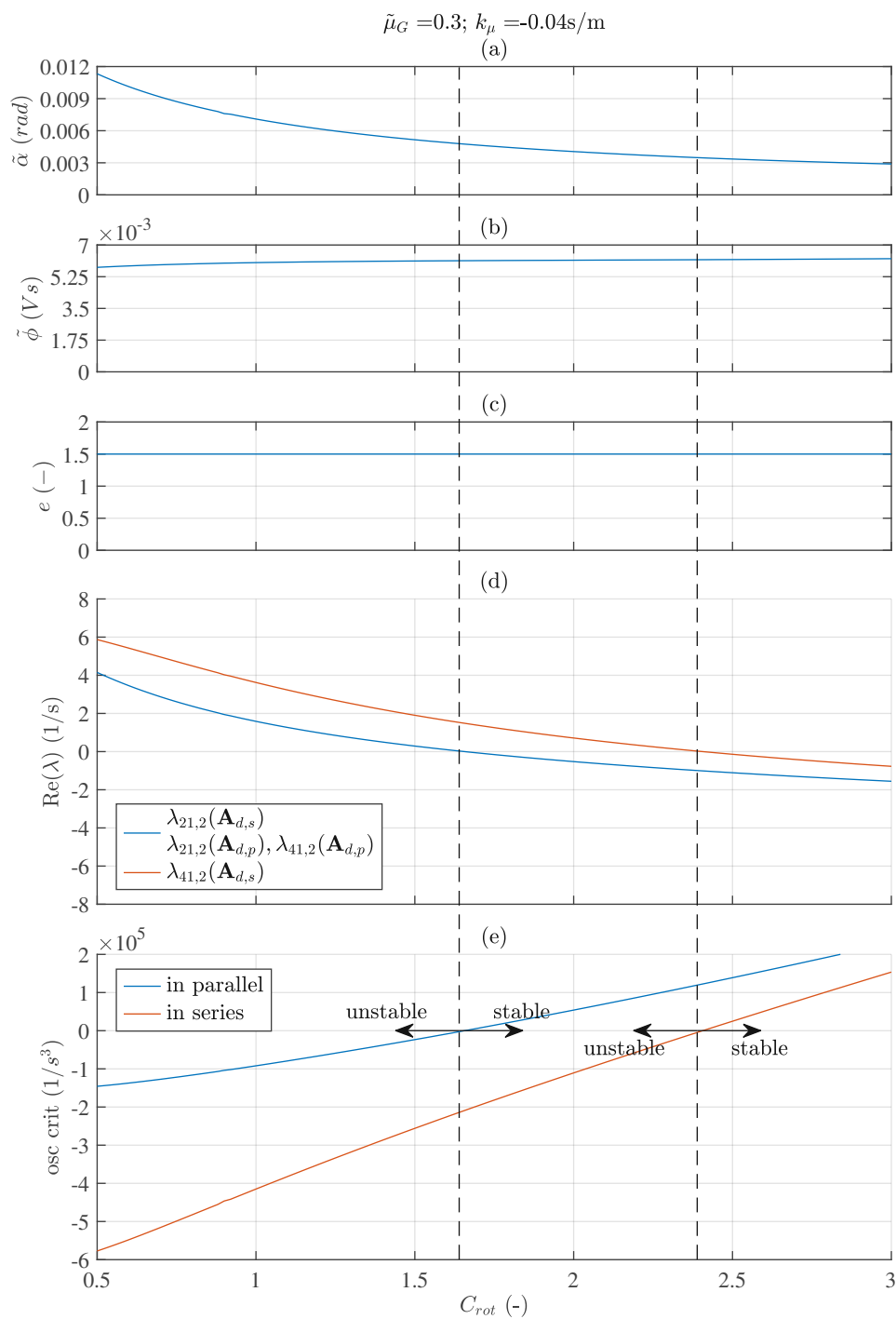


Figure 4.16: Stability criteria of the double-magnet models with respect to the relative stiffness

Analysis of the multibody dynamics model of the track brake

Using simplified models, possible self-excitation mechanisms of the magnetic track brake were identified in the previous chapter. Compared to the simplified models, the multibody dynamics model has a significantly increased degree of detail. This applies in particular to the elastic structure of the brake frame, which allows deformations in all three dimensions, the magnet-rail friction contact model, and the extension to four magnets with two magnetic circuits each. This chapter now aims to determine whether the conclusions drawn from the simplified models can be transferred to the multibody dynamics model to subsequently obtain qualitatively comparable results to vehicle tests.

To study the stability of steady system states, eigenvalue analyses of the locally linearised system are conducted, dependent on the vehicle velocity \bar{v} and corresponding coefficient of friction. Time integration is used to simulate a braking manoeuvre which is then compared with data of vehicle tests.

5.1 Brake-rail contact and steady state analysis

Linearisation points are required to perform eigenvalue analyses with the nonlinear multibody dynamics model of the magnetic track brake. Particular knowledge of the contact status is needed for each contact force element (at the positions $j1$, $j2$ and jZG for $j = A, B, C, D$) between the braking magnets and the rails, Figure 3.7. Due to increasing friction coefficients $\tilde{\mu}_G(\tilde{v})$, the loads on the brake frame change with decreasing \tilde{v} , which can lead to changes in the contact status. Also, the placement of the centre contact point jZG by the coordinates e_x and e_z influences the deformation of the frame.

With $\tilde{\mu}_G = 0.08-0.32$ (see Figure 2.16) and $e_z = 0-1$ mm (see Appendix B.1), steady state analyses are performed. Steady state values are marked by "~". Parameters used for the model are listed in Table 5.1.

Parameter	Symbol (Unit)	Value
Electric resistance	R_{el} (Ω)	10
Number of windings	N (-)	300
Const. magnetic reluctance	$R_{m,0}$ ($\frac{A}{Vs}$)	380000
Coefficient of the magnetic air-gap model 1	a_{hyp} (m)	0.0021
Coefficient of the magnetic air-gap model 2	b_{hyp} (m)	0.01
Offset of the magnetic air-gap model	$a_{hyp,0}$ (m)	-0.002
Source voltage	u_{src} (V)	120
Magnetic cross-section	A (m^2)	0.0036
Vacuum permeability	μ_0 ($\frac{N}{A^2}$)	1.2566e-6
Actuation cylinder force	F_{Cyl} (N)	3000
Longitudinal position of the centre contact point	e_x (cm)	31
Vertical position of the centre contact point	e_z (mm)	0-1
Coefficient of friction	$\tilde{\mu}_G$ (-)	0.08-0.32

Table 5.1: Model parameters for the steady state analyses

Figure 5.1 shows the change of contact status with respect to $\tilde{\mu}_G$ and e_z . Diagram (a) depicts the number of force elements with *closed contact* (=contact force elements are in contact) status per side. The associated contact points for one side (left) are listed in Table 5.2. For a fixed value of e_z , the number of closed contacts can change during braking when $\tilde{\mu}_G$ increases, see the two horizontal lines $e_z = 0.80$ mm and $e_z = 0.47$ mm. For $e_z = 0.80$ mm and small values of $\tilde{\mu}_G$, four contacts per side $j1$ and jZG ($j = A \dots D$) are closed. With $\tilde{\mu}_G > 0.3$, the contact of the centre contact points of the forerunning magnets (AZG , CZG) is opened. For $e_z = 0.47$ mm, the number of closed contacts per side decreases from six to four with a transition zone at $\tilde{\mu}_G = 0.16-0.22$ as contacts of the inside endpieces ($j2$) open.

Diagram (b) of Figure 5.1 shows the overall vertical force for one side $\tilde{F}_{N,z} = \sum \tilde{F}_{N,jk,z}$ ($j = A, B$) with respect to the coefficient of friction $\tilde{\mu}_G$ for $e_z = 0.47$ mm and $e_z = 0.80$ mm. For $e_z = 0.47$ mm, $\tilde{F}_{N,z}$ decreases when $\tilde{\mu}_G$ rises.

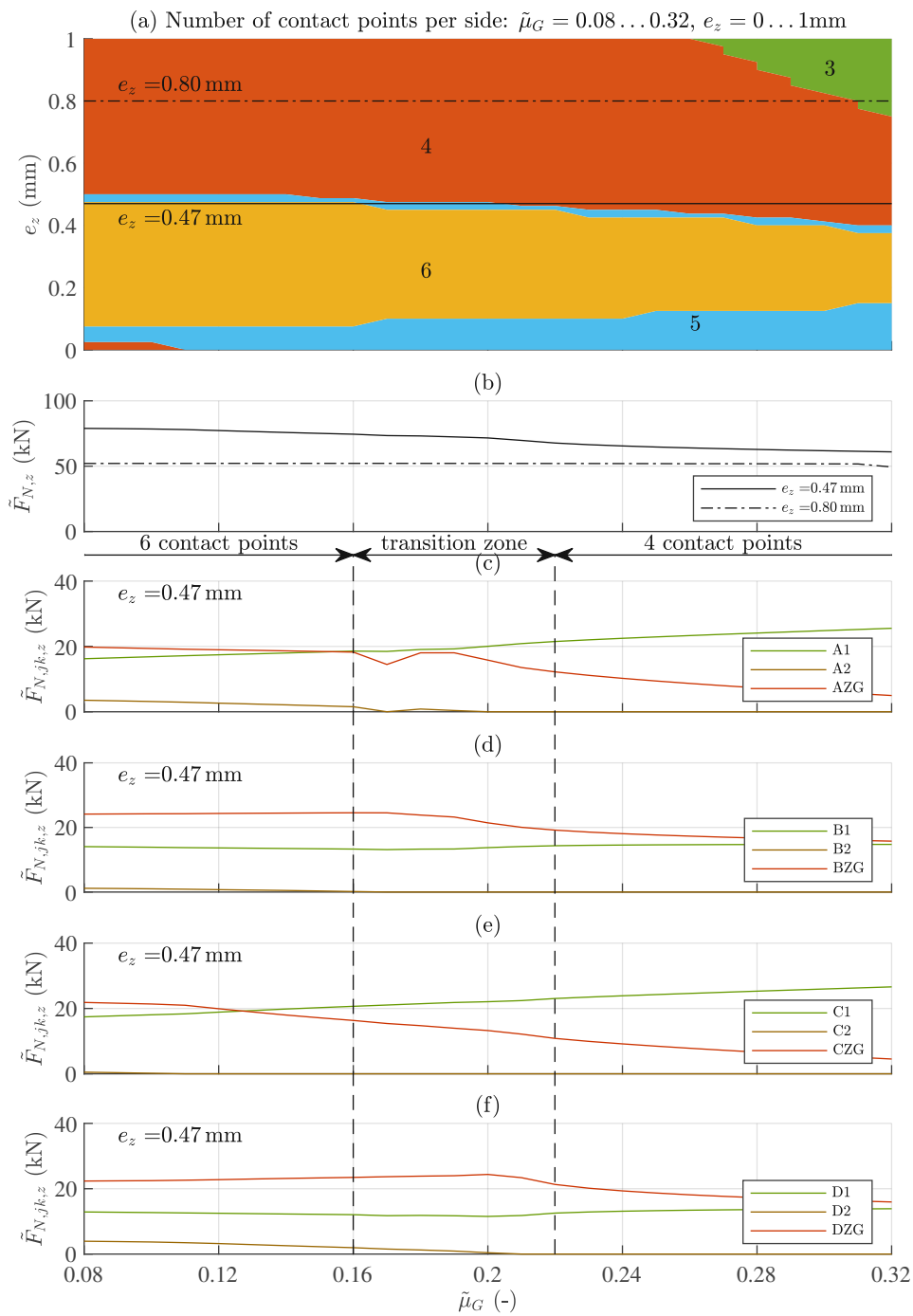


Figure 5.1: Steady state analysis of the brake-rail contact points

Area	Contacts (per side)	Contact points left	Contact points right
yellow	6	A1, A2, AZG, B1, B2, BZG	C1, C2, CZG, D1, D2, DZG
blue	5	A1, AZG, B1, B2, BZG	C1, CZG, D1, D2, DZG
orange	4	A1, AZG, B1, BZG	C1, CZG, D1, DZG
green	3	A1, B1, BZG	C1, D1, DZG

Table 5.2: Contact points with respect to $\tilde{\mu}_G$ and e_z

This is plausible as the magnet moves in lateral direction under load due to the elastic deformation of the brake frame leading to a widening of the effective air-gap \tilde{s} . As a result, the magnetic attractive forces $\tilde{F}_{A,i,z}$ decrease, resulting in decreasing normal forces. For $e_z = 0.80$ mm, attractive forces $\tilde{F}_{A,z}$ are smaller than for $e_z = 0.47$ mm and approximately constant.

Diagrams (c) to (f) in Figure 5.1 give a more detailed view on the contact forces between the magnets and the rails for $e_z = 0.47$ mm. The diagrams show the normal forces of all four corners A, B, C, D . With $\tilde{\mu}_G$ increasing, normal forces in the magnet-rail contact $\tilde{F}_{N,jk,z}$ distribute from the centre outwards. In the transition zone, normal forces $\tilde{F}_{N,j2,z}$ become zero as the contact of the inside endpieces opens. Open contacts lead to a vertical distance between the magnet segments and the rail, which reduces the magnetic forces.

5.2 Stability analysis

Since the vehicle tests have shown a strong relation between vibrations and velocity, the study of its influence on the stability of solutions of the dynamical system is particularly relevant.

The (linear) stability of steady states of the system is determined by analysing the real parts of its eigenvalues. Considering friction-dependent linearisation points (Section 5.1), modal analyses at vehicle velocities \tilde{v} between 100 km/h and 0 km/h are performed with the model parameters from Table 5.3. The mode shapes associated to the relevant eigenvalues λ_1 - λ_4 are depicted in Figure 5.2. The first mode shape (of λ_1) describes a lateral rigid body motion, the others correspond to the first asymmetric (λ_2), the first symmetric (λ_3) and the second asymmetric (λ_4) deflection mode of the structure.

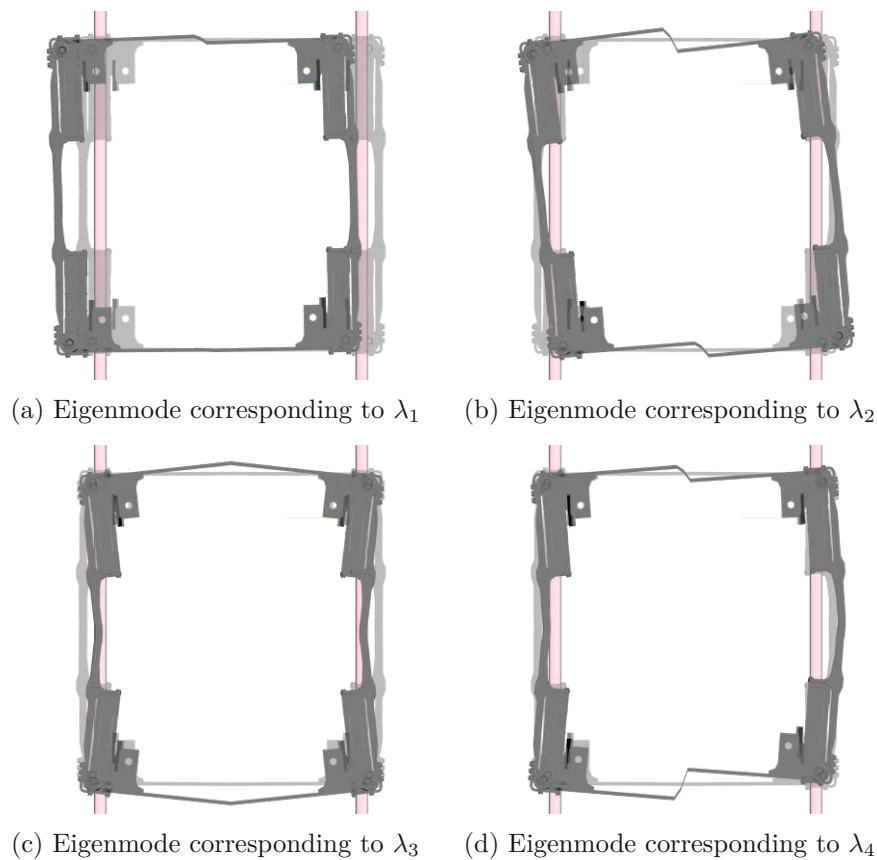


Figure 5.2: Characteristic eigenmodes of the multibody dynamics model

Figure 5.3 shows plots of results of the analyses with respect to \tilde{v} . Diagram (a) shows the applied friction characteristics (2.3) and its derivative with respect to \tilde{v} , \tilde{k}_μ . Diagram (b) depicts the frequencies and Diagram (c) the real parts of the first four pairs of conjugate complex eigenvalues λ_1 - λ_4 . As seen from the diagram, the frequencies are nearly constant

Parameter	Symbol (Unit)	Value
Eddy current loss factor	$G \left(\frac{1}{\Omega}\right)$	1500
Friction characteristics	$\tilde{\mu}_G (-)$	mean μ_G
Damping ratio	$D (-)$	0.01
Vehicle velocity	\tilde{v} (km/h)	100-0
Vertical position of the centre contact point	e_z (mm)	0.47

Table 5.3: Additional model parameters for the stability analyses

for a broad velocity range, directly before standstill, however, the frequencies of λ_1 and λ_2 drop. With decreasing velocity, λ_4 has the largest real parts (compared to λ_1 - λ_3) with positive values $\text{Re}(\lambda_4) > 0$ for $\tilde{v} < 70$ km/h. $\text{Re}(\lambda_4)$ increases until a maximum is reached at approximately 20 km/h. At this velocity, severe vibrations were detected in the second asymmetric deflection mode (Figure 5.2(d)) during the vehicle tests (Section 2.2). For velocities below 10 km/h, $\text{Re}(\lambda_4)$ decreases and becomes negative again. Also $\text{Re}(\lambda_3)$ increases with decreasing velocity and becomes positive for $\tilde{v} < 35$ km/h. At speeds $\tilde{v} < 8$ km/h values reach a maximum with $\text{Re}(\lambda_3) > \text{Re}(\lambda_4)$. It can be assumed that at such low speeds self-excited vibrations also occur in the symmetrical deflection mode (Figure 5.2(c)). However, as the magnetic track brake was deactivated during vehicle tests at 10 km/h, these did not evolve.

Diagrams (d) to (g) of Figure 5.3 show plots of the contact forces for the contact points between the track brake and the rails. The diagrams are very similar to those discussed in the steady state analysis, see Figure 5.1.

Stability maps In addition to the vehicle velocity, the characteristics of the coefficient of friction in the magnet-rail contact is of key importance for the analysis of stability behaviour. Since friction is velocity-dependent, a simultaneous study of the friction characteristics and velocity seems appropriate. Figure 5.4 shows stability maps and $\text{Re}(\lambda_4)$ (positive values in red, negative values in green) with respect to steady system states of the (locally linearised) multibody dynamics model (for $e_x = 310$ mm and $e_z = 0.47$ mm) and parameters $\tilde{\mu}_G$ and \tilde{k}_μ for six velocities \tilde{v} .

It becomes clear that the area of stable steady states expands with decreasing velocity. This is plausible as dampening effects due to friction forces in lateral direction increase with decreasing velocity. Further, two friction characteristics, high μ_G and low μ_G (see Figure 2.16) are depicted. The point on the respective friction characteristics that corresponds to the actually considered velocity is marked by a distinctive dot. The sequence of subplots for different actual velocities illustrates that this dot moves from the upper left corner (small values of $\tilde{\mu}$ and \tilde{k}_μ) to the bottom right when velocity decreases with braking. The braking manoeuvre is started in the green area with all eigenvalues negative, indicating asymptotic stability of first order of the steady state solutions. Then the real parts of the eigenvalues increase with decreasing velocities, with transition to the unstable (red shaded) areas until about 6 m/s, when real parts start to decrease again.

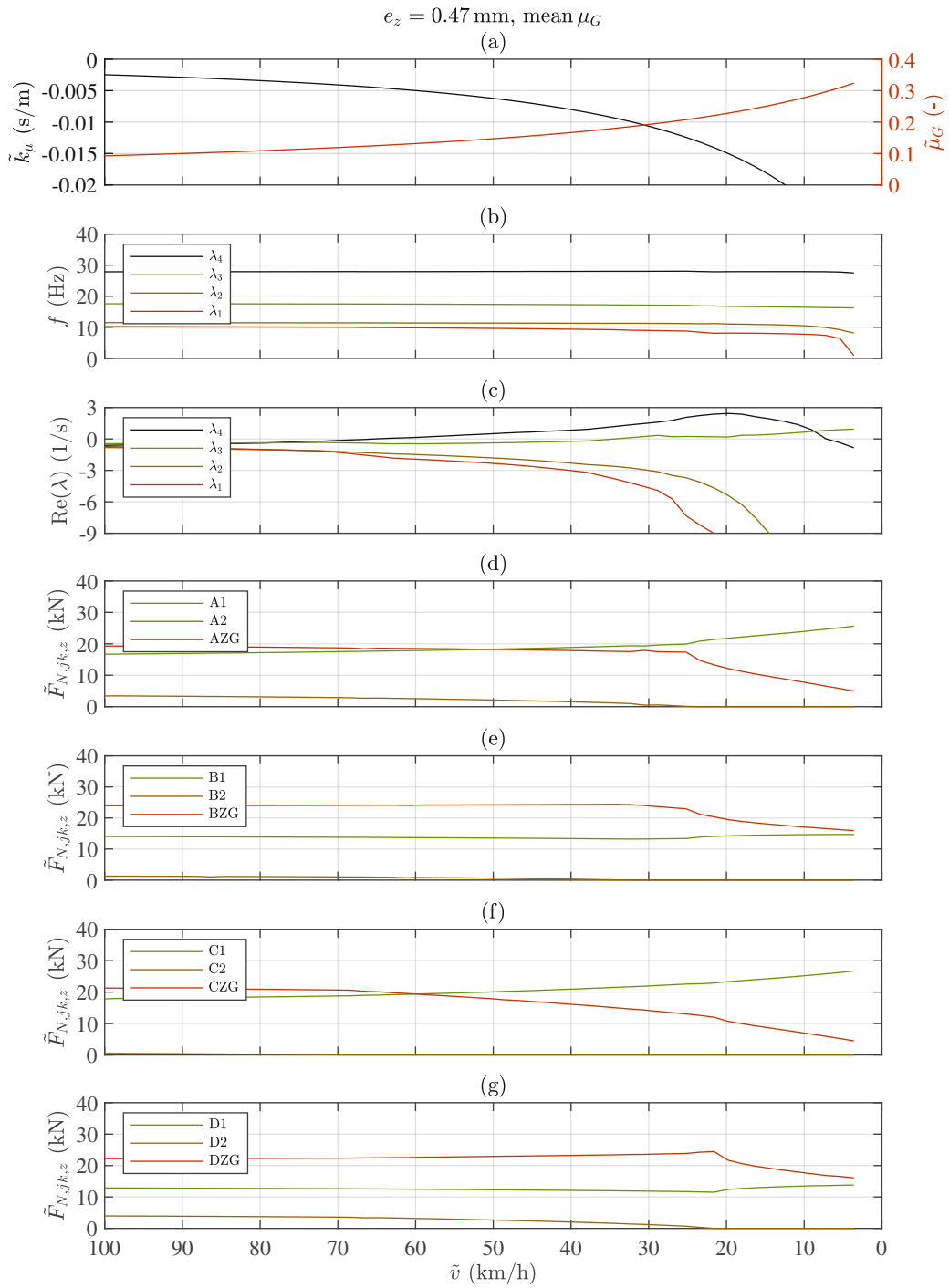


Figure 5.3: Modal analysis with respect to the steady state velocity

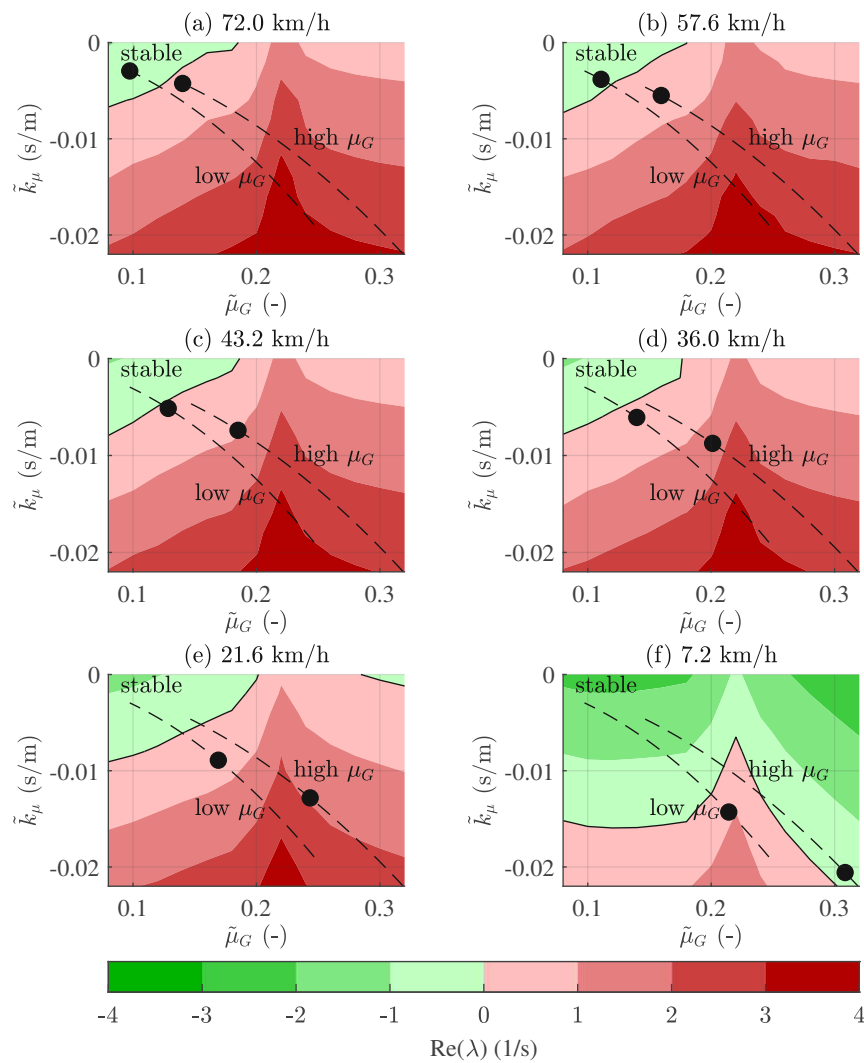


Figure 5.4: Stability maps of the multibody dynamics model with respect to the friction parameters

Considering high μ_G characteristics and $\tilde{\mu}_G < 0.22$, real parts of eigenvalues increase with increasing $\tilde{\mu}_G$. This corresponds to the results of the simplified system model, Figure 4.4(e). The higher $\tilde{\mu}_G$ and the more negative \tilde{k}_μ , the more likely unstable self-excited vibrations may appear. For $\tilde{\mu}_G > 0.22$, the inward endpieces lose contact with the rail. Notice the corresponding spikes in all subplots of Figure 5.4. With respect to the simplified system model, this behaviour may be interpreted as a displacement in the contact point to the front and therefore as a decrease of distance l . Then the stable area expands as well, Figure 4.4(c). For small velocities and large friction coefficients, friction in lateral direction adds considerable damping to the system, and vibrations may be attenuated.

5.3 Analysis in the time domain

To further examine the dynamical behaviour around the unstable equilibrium states, as well as during braking, time integrations are performed. Complete braking manoeuvres are simulated, starting with the electrical activation of the brake until the vehicle reaches full stop. For an initial velocity of $v_0 = 43.2$ km/h, Figure 5.5 shows results of a time integration. Diagram (a) shows the approximately linear decrease in velocity from v_0 until 0 km/h over a simulation time of 7.5 s. During the braking manoeuvre, the friction coefficient μ_G continually increases (red coloured plot in the diagram). The track brake is activated at 0.5 s which is indicated by the signals of the actuating cylinder force F_{cyl} and the current i_{AD} , Diagram (b). With the activation of the brake, the brake forces $F_{B,A,x}$ and $F_{B,C,x}$ increase, Diagram (c). Diagrams (d) to (g) in Figure 5.5 show the values of the normal contact forces $F_{N,jk,z}$ for each corner ($j = A, B, C, D$) and contact point ($k = 1, 2, ZG$) separately.

It can be seen from the signals of the brake forces $F_{B,jk,x}$ that vibrations begin to evolve at a time of $t \approx 4$ s a vehicle velocity of roughly $v_{vcl} \approx 20$ km/h and a sliding friction coefficient of $\mu_G \approx 0.22$. Simultaneously, the inner end pieces lose contact with the rail. This behaviour is consistent with the analysis of contact points in the steady state, see Figure 5.1.

Figure 5.6 depicts the time frame between 4.5 s and 5.5 s, when the vibration amplitudes of the brake forces $F_{B,A,x}$ and $F_{B,C,x}$ reach their maxima. Diagram (c) clearly displays the asymmetric vibration of the left and right brake forces. As the brake force transmission link between the bogie and the track brake is designed as a mechanical stop, only positive brake forces can be transmitted. This is observed by a periodic loss of contact with the bogie, see marker $F_B = 0$.

For a simulation time $t > 6$ s and a velocity of $v_{vcl} < 10$ km/h, the vibration amplitudes in Figure 5.5 become smaller, which may be attributed to the dampening effect of the increasing lateral friction force component. At $t = 7$ s, the track brake is deactivated in the simulation and the signals of F_{cyl} and i_{AD} return to zero, Diagram (b).

5. ANALYSIS OF THE MULTIBODY DYNAMICS MODEL OF THE TRACK BRAKE

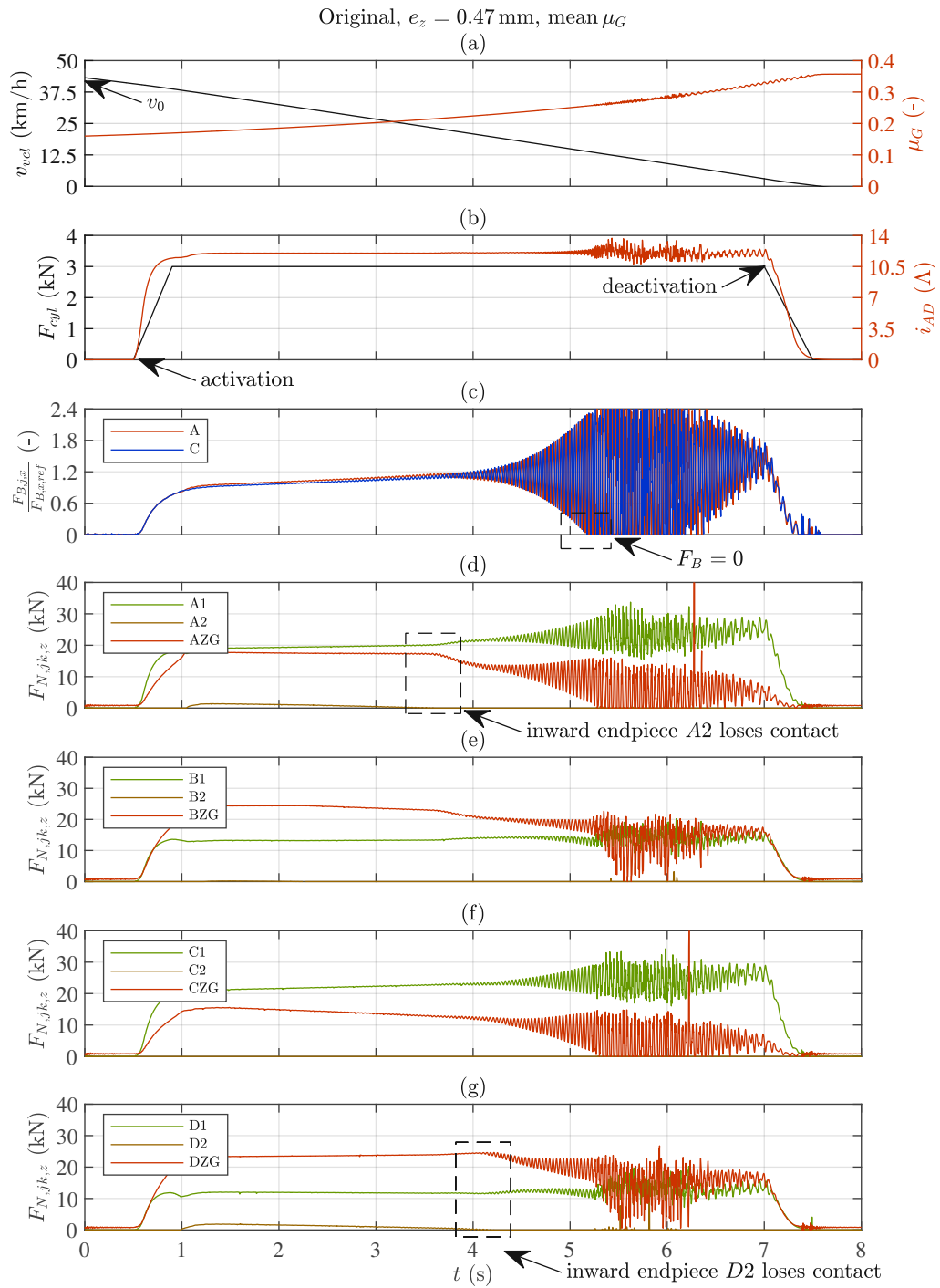


Figure 5.5: Simulated braking manoeuvre – overview

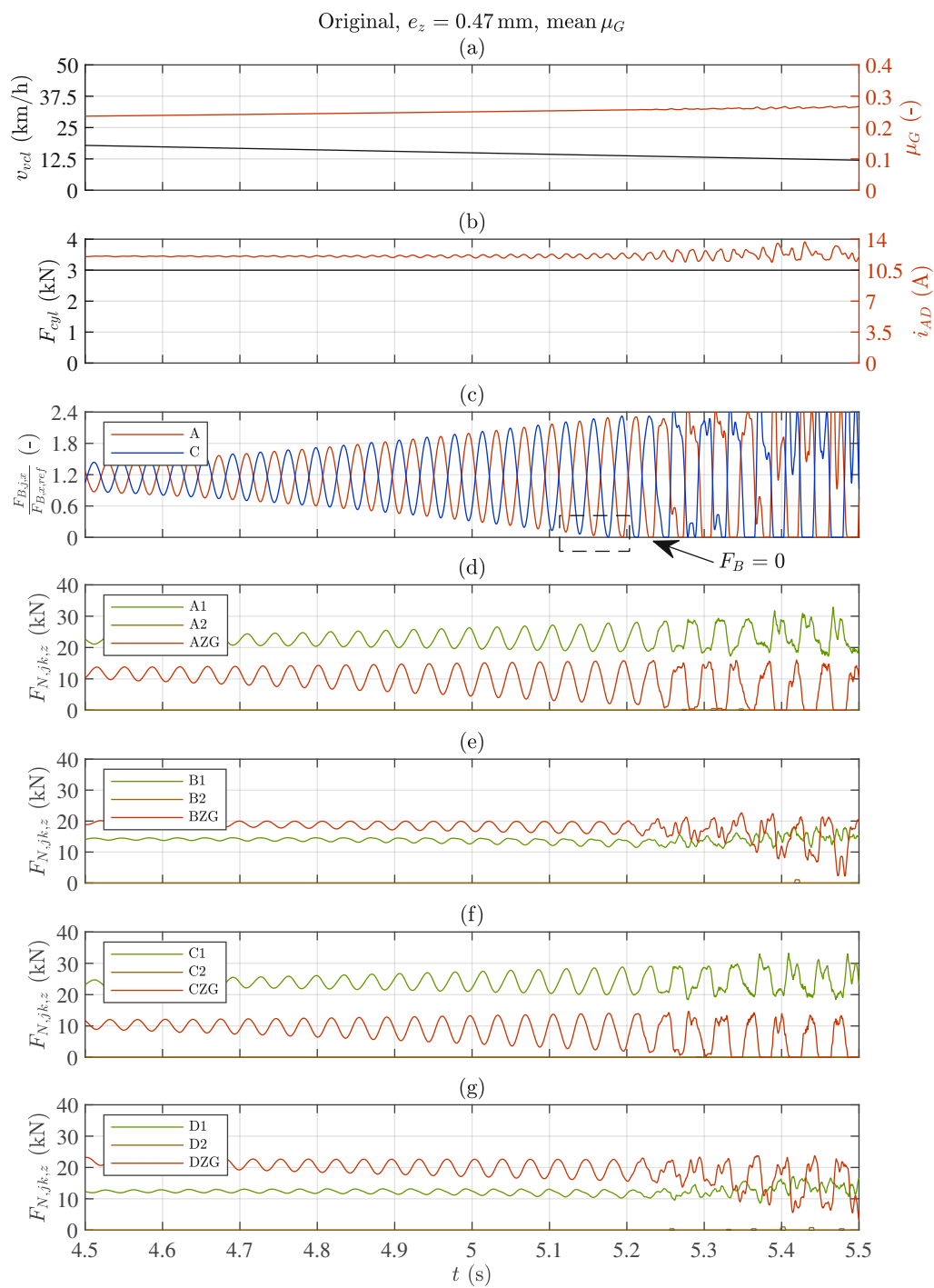


Figure 5.6: Simulated braking manoeuvre – detail

Influence of the friction characteristics and comparison with vehicle tests To determine if the multibody dynamics simulations are qualitatively comparable to the vehicle tests, simulations of a braking manoeuvre are performed and compared with vehicle test data. Since the actual friction forces in the magnet-rail contact are unknown during the measurements, simulations with different friction coefficient characteristics are performed and their influence on the vibration amplitudes examined.

The basis of this analysis is a representative measurement of a braking manoeuvre from the vehicle tests (*V1008*) with an initial velocity of $v_{vcl} \approx 35$ km/h. Figure 5.7 (a) and (b) show the measured velocity v_{vcl} , the current i_{AD} as well as the brake forces $F_{B,A,x}$ and $F_{B,C,x}$.

Simulation results with the different levels of friction show a significant influence on both the average brake force and the amplitudes of the vibrations, Diagrams (c) and (d). While vibrations at large amplitudes develop with high μ_G , the simulation with low μ_G enters a limit cycle with very small amplitudes. Although the measured brake forces generally show similar behaviour to the simulations, variations in the amplitudes are clearly visible. The differences may be attributed to not modelled, varying contact conditions between magnet and rail.

The differences between measurements and simulations can be reduced by adjusting the friction coefficient characteristics, as shown in Diagrams (e)-(f). The characteristics ALT μ_G is generated (freely chosen) by oscillation of the friction value around the characteristics mean μ_G within the boundaries of low μ_G and high μ_G , Figure 5.7(f). Qualitatively comparable results with vehicle tests can be obtained using the model, however better knowledge of the magnet-rail contact conditions is required.

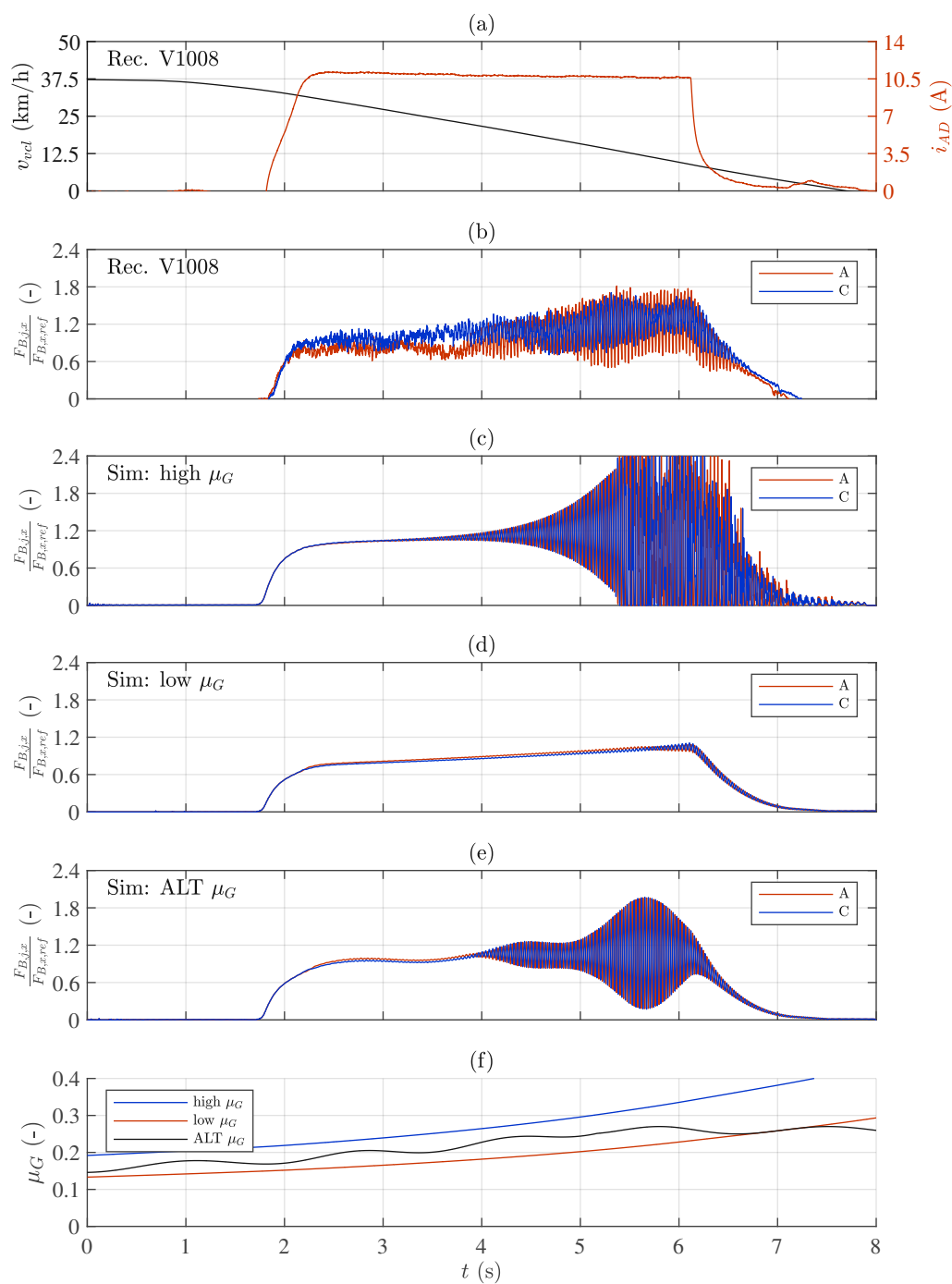


Figure 5.7: Comparison of time integration results with field test measurements

CHAPTER **6** 

Mitigation of self-excited vibrations

To reduce the mechanical loads on components of the magnetic track brake and the bogie, the aim of this chapter is to propose designs in which self-excited vibrations of the track brake frame do not occur or are mitigated. Simultaneously, the optimisation of the achievable brake forces is considered an important secondary target. Based on the findings of the previous chapters, new design concepts are developed. Based on the findings of the linear stability analysis of the simplified models, specific design features of the Original Design are modified to improve the stability behaviour of the system. To validate the quality of the proposed designs, assessments of the brake force, stability analyses and time integrations are performed in accordance with Chapter 5.

6.1 Alternative design concepts

Based on the results of the stability analyses with the linear system models in Chapter 4, design proposals for future magnetic track brakes are developed. The following observations made from the study of the criteria for oscillatory stability of the single magnet model (4.17) and the double-magnet model (4.40) contribute to the development of these proposals:

- The electro-magneto-mechanical coupling and negative values of the damping term are the cause of the self-excited vibrations.
- The analysis of the electrical circuits of double-magnet models has shown that in series connection of magnets increases this coupling for asymmetric oscillation modes (4.40), Section 4.4.
- Increasing the mechanical stiffness "stabilises" the simplified system model.

These findings are revisited in the following three track brake designs which are subsequently presented:

Design 1: Increased stiffness

Increasing the stiffness of the track brake frame has already been taken up as an intuitive measure for the simplified models. The numerical evaluation of the criterion for oscillatory stability has shown that this countermeasure has a positive effect on the stability behaviour, Section 4.2.

The stiffness, however, is limited by external constraints such as mass limitations, available installation space and normative requirements. Economic considerations require light weight designs of brake components, excluding large cross sections [57]. The European standard for magnetic track brakes EN16207 [2] includes load cases with enforced displacements applied to the brake frame, which favours flexible structures. For the following analyses, it is assumed that the stiffness of the brake frame can be increased by 20% at constant mass. The increase of stiffness is implemented by scaling the stiffness matrix of the finite element model of the brake frame.

Design 2: Repositioned track brake-bogie interface

Reducing the lateral distance a between the force transmission and the rail was identified as an effective measure to stabilise the system for the simplified model, Figure 4.4(d). This is plausible because the geometric parameter a influences the coupling terms of the mechanical and electro-magnetic system equations. Repositioning the mechanical stops outwards, as seen in Figure 6.1, reduces the bending moment in the longitudinal connectors during braking. The resulting reduced deflection of the brake frame is expected to decrease the coupling of the mechanical and the electro-magnetic system.

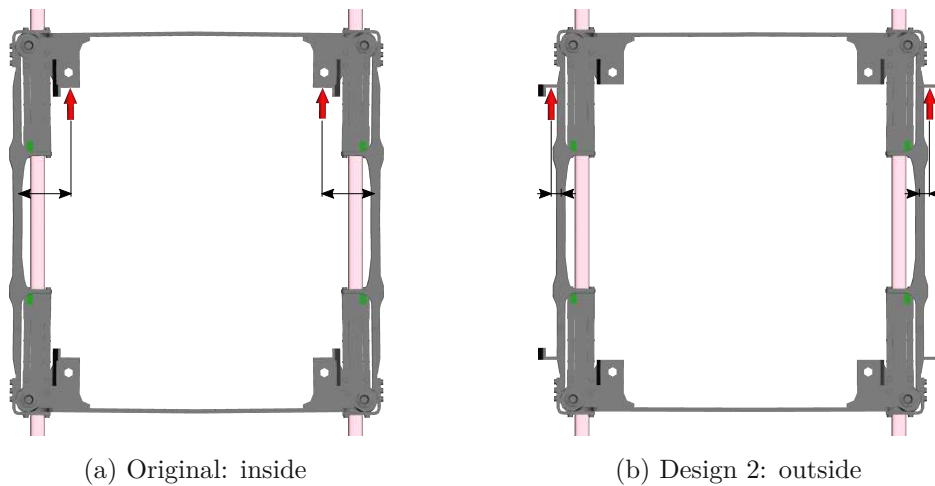


Figure 6.1: Repositioning the track brake-bogie interface

Design 3: Interchanged electrical connections

In Section 4.4, the influence of the electrical connection on the stability behaviour of the double-magnet model has been studied. It has been shown that in the asymmetrical oscillation mode, the electro-magneto-mechanical coupling of two magnets is increased by their in series connection. The electro-magneto-mechanical coupling of the symmetrical oscillation mode remains unchanged compared to a single magnet model. This can result in the symmetrical mode being stable while the asymmetrical mode is unstable, Figure 4.16.

The magnetic track brake studied consists of two pairs of magnets electrically connected in series. In the original configuration, the diagonally located magnets ($A+D$ and $B+C$) are connected in series, Figure 3.13. In the second asymmetric oscillation mode, the diagonally located magnets perform an opposed relative motion to the rail, see Figure 5.2(d). It is assumed that the in series connection of the diagonally located magnets in the asymmetric vibration mode creates an amplification of the electro-magneto-mechanical coupling.

The magnets located behind each other perform a symmetric motion relative to the rail. Assuming that the coupling can be mitigated, the magnets located behind each other ($A+B$ and $C+D$) are therefore connected in series in Design 3, Figure 6.2.

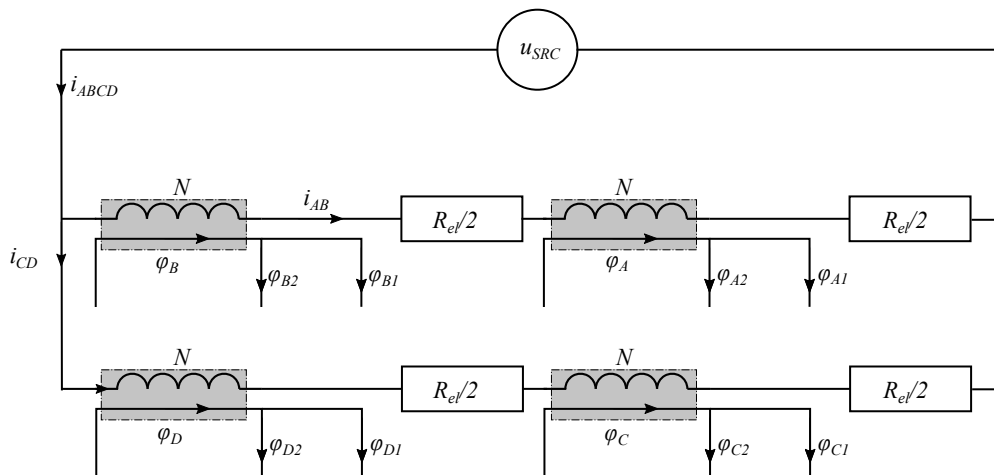


Figure 6.2: Design 3: Interchanged electric connections

6.2 Comparison of the designs

All proposed design variants must be robust regarding different operational and environmental conditions. Vibrations should be suppressed in a wide range of operational parameters. This includes variable coefficients of friction in the brake-rail contact, as well as pole shoe wear or contaminated friction surfaces due to pick-up weldings. Besides, braking performance must not be influenced negatively. Steady state normal forces are investigated to compare the achievable brake force of the Original Design and the three new design proposals. Stability maps of the designs are determined from real parts of all eigenvalues of the locally linearised systems. To investigate the influence of the design variants on structural loads, braking manoeuvres are simulated in the time domain.

6.2.1 Comparison of brake forces

To determine the influence of the designs on the brake force, steady state normal forces between the brake magnets and the rail are calculated. The summarised normal forces $\sum \tilde{F}_{N,j,z}$ are compared for a velocity range below 72 km/h. With decreasing velocity \tilde{v} , the coefficient of friction $\tilde{\mu}_G$ increases, with (2.16) and the mean μ_G characteristics. To consider different degrees of pole shoe contamination due to pick-up weldings, the parameter e_z is varied from 0-1 mm, Figure 6.3.

Figure 6.3 (a) to (d) shows $\sum \tilde{F}_{N,j,z}$ for the Original Design and for Designs 1, 2 and 3 with respect to \tilde{v} and e_z as a colour map. It can be seen that the normal force is particularly dependent on e_z . In the range of $e_z = 0.4-0.6$ mm a steep decrease of the normal contact force is noticeable. This is attributed to the loss of contact of the inner end pieces, compare Figure 5.1. The increased stiffness of the brake frame in Design 1 causes a poorer vertical alignment of the magnets to the rail. When e_z is increased, this leads to an earlier loss of contact and lower normal forces than with the Original Design.

With deceleration, rising coefficient of friction $\tilde{\mu}_G$ and thus higher lateral deflection of the magnets, a decrease of $\sum \tilde{F}_{N,j,z}$ is observed from diagrams (a), (b) and (d). This is due to the reduction of the magnetic attraction forces $\tilde{F}_{A,j,z}$ with lateral deflection, compare Figure 3.9(b). This reduction is not observed with Design 2, as the lateral deflection is lower than with the Original Design and Design 1.

The type of electrical connection does not lead to any change in the steady state of the system. The quasi-static normal forces of the Original Design and Design 3 are identical, Diagrams (a) and (d).

The results are compared for velocities 64.8 km/h, 46.8 km/h, 28.8 km/h and 10.8 km/h as indicated in the diagram. Assuming $\tilde{\mu}_G$ equal for all design variants, Figure 6.4 shows the relative brake forces of the three design variants with respect to the Original Design and e_z . Thus, the Original Design (O) as well as Design 3 (D3) have a constant value of 1. Design 2 (D2) yields to the highest relative brake forces in the considered parameter range. Design 1 (D1) leads to reduced brake forces, except for low speeds and $e_z < 0.4$ mm.

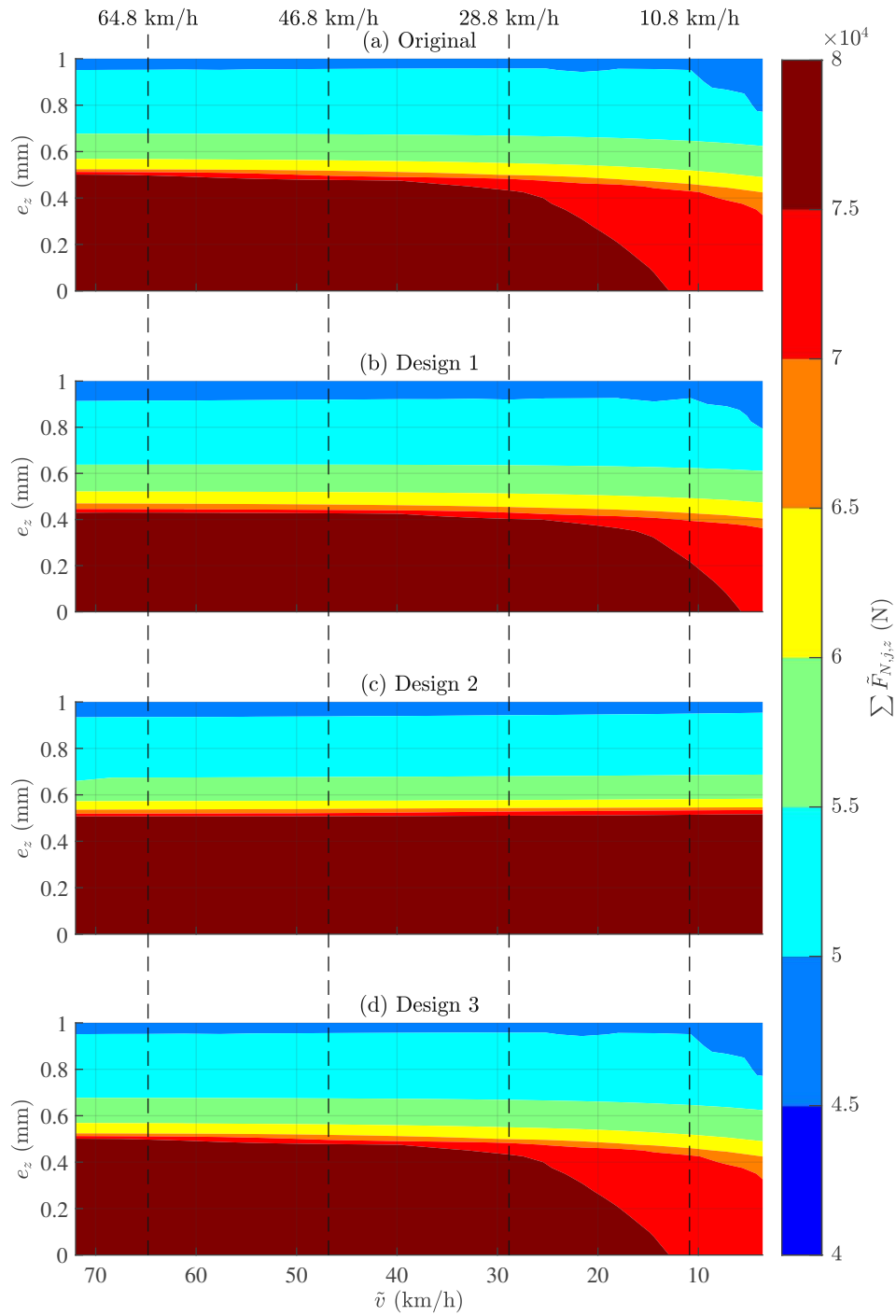


Figure 6.3: Comparison of normal contact forces

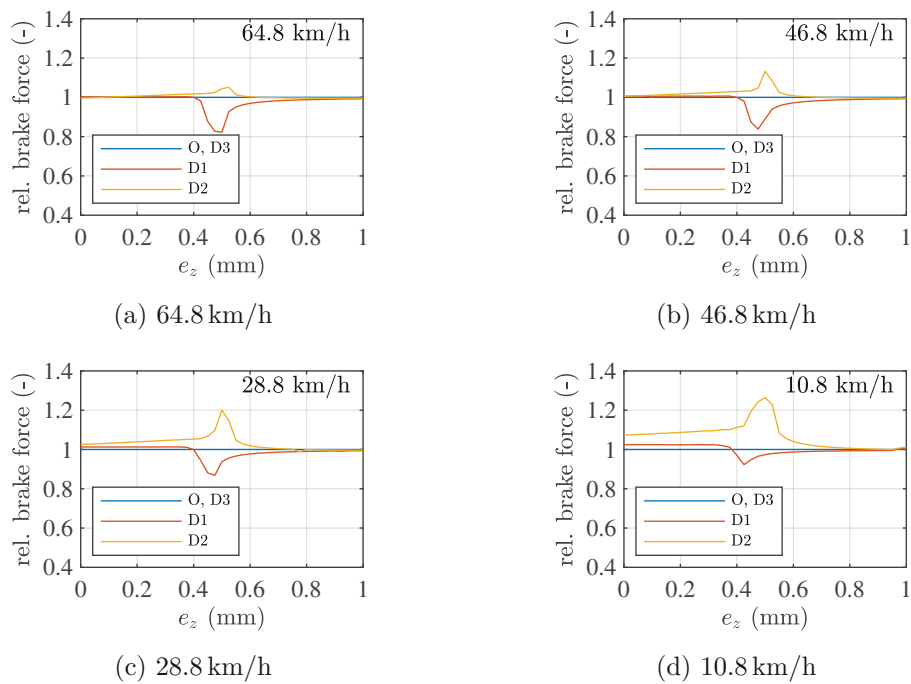


Figure 6.4: Relative brake force for the alternative designs

6.2.2 Comparison of the stability behaviour

To examine the influence of the three design proposals on the stability behaviour, stability maps are compared for the same parameter range as in Section 6.2.1 ($e_z = 0-1$ mm and $\tilde{v} = 72-0$ km/h). As in Chapter 5, the stability maps are based on the analysis of the real parts of the eigenvalues of the locally linearised models in their steady states. Figure 6.5 shows the maximum real parts of the first four conjugate complex eigenvalues $\max(\text{Re}(\lambda_i))$ ($i = 1-4$) for the Original Design and Designs 1, 2 and 3 with respect to vehicle velocity \tilde{v} and the vertical position of the contact point e_z . The stability maps correspond to those presented in Section 5.2, Figure 5.4, green shading represents negative real parts, red shading positive real parts. The transition between green and red represents the stability border. Figure 6.5 shows stability maps for steady states of a braking manoeuvre with varying \tilde{v} and e_z , assuming the mean μ_G friction characteristics (2.3).

For the Original Design as well as Designs 1, 2 and 3, the eigenmodes associated to the first four eigenvalues correspond to those shown in Figure 5.2:

- λ_1 : lateral rigid body motion
- λ_2 : first asymmetric deflection mode of the structure
- λ_3 : first symmetric deflection mode of the structure
- λ_4 : second asymmetric deflection mode of the structure

For the Original Design, there is a large non-stable region with maximum real parts at $e_z = 0.45$ mm, Figure 6.5 (a). For this value, Figure 6.7 shows the analysed eigenvalues in detail with associated frequencies $f(\lambda_i)$ nearly constant across the velocity range. For all velocities considered, λ_4 ($f(\lambda_4) = 28$ Hz) has positive real parts. Also, the real part of λ_3 ($f(\lambda_3) = 18$ Hz) becomes positive at low velocities. The eigenvalues λ_1 and λ_2 have only negative real parts.

The stability map of Design 1 (increased stiffness) demonstrates similar system behaviour as the Original Design but with a smaller unstable parameter region and maximum real parts at $e_z = 0.375$ mm, Figure 6.5 (b). The detailed eigenvalue results seen in Figure 6.7 also show similar results, albeit at larger frequencies for λ_2 - λ_4 . This result corresponds with the studies on stability in Section 4.2, which demonstrated that increasing the stiffness can stabilise the (simplified) system, Figures 4.2 and 4.4(b).

For Design 2 (repositioned track brake-bogie interface), all eigenvalues calculated have negative real parts, Figure 6.5 (c). The detailed results for $e_z = 0.45$ mm presented in Figure 6.8 show increased frequencies and negative real parts of λ_3 and λ_4 . This indicates stable system behaviour across the entire parameter range analysed.

For Design 3 (interchanged electrical connections), the area of positive real parts is significantly smaller than for the Original Design, Figure 6.5 (d). Still, for $e_z > 0.4$ mm and $\tilde{v} < 25$ km/h an area with small positive real parts remains. In the detailed analysis it is most noticeable that the real part of λ_4 (asymmetrical mode) is reduced significantly (compared with the Original Design) and becomes negative, Figure 6.9. The real part

of λ_3 (symmetrical mode) remains unchanged. This behaviour is comparable to the findings in the analysis of the double-magnet models electrically connected in series and in parallel, Figure 4.14 (b) and (d).

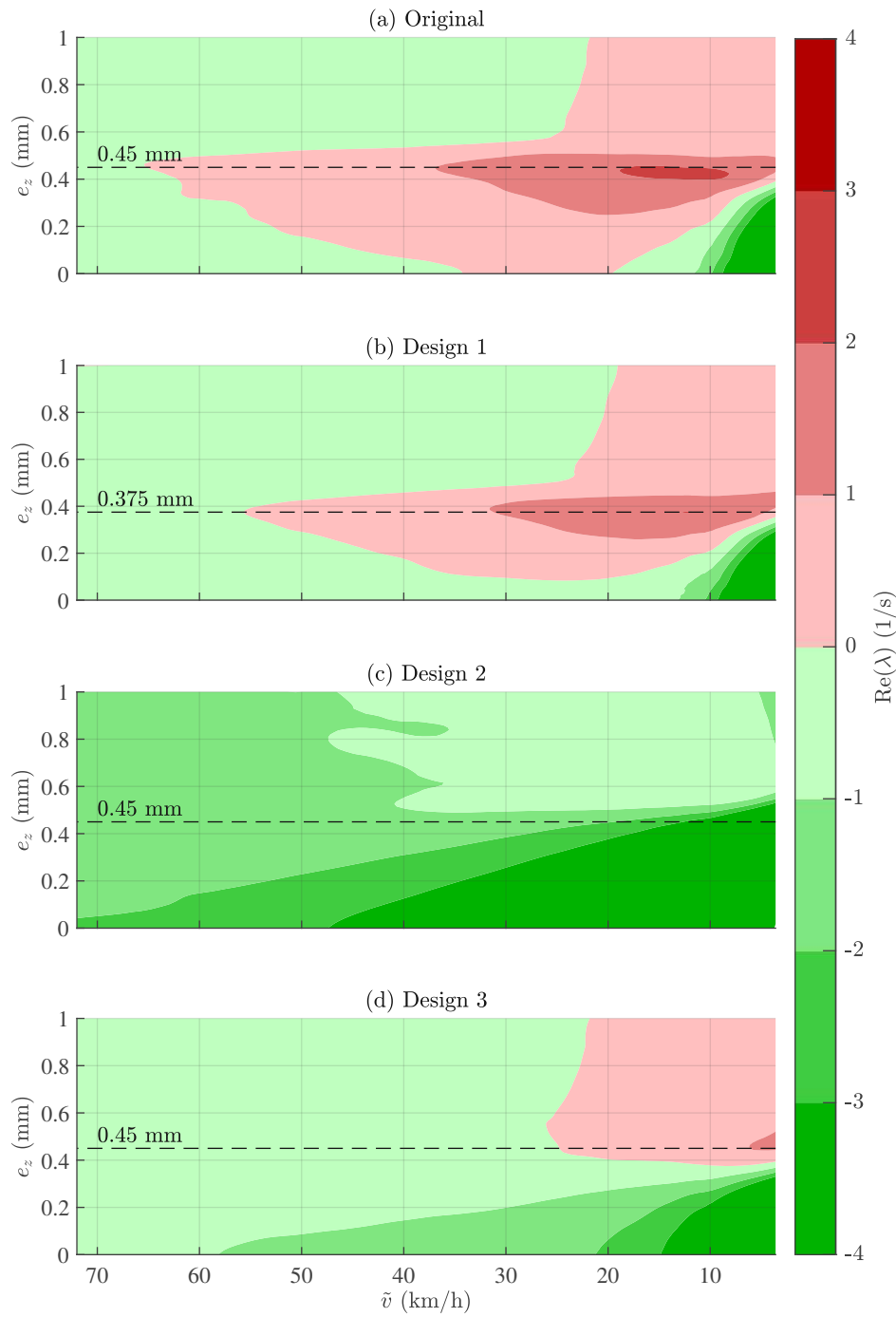


Figure 6.5: Stability maps of the proposed designs with respect to \tilde{v} and e_z

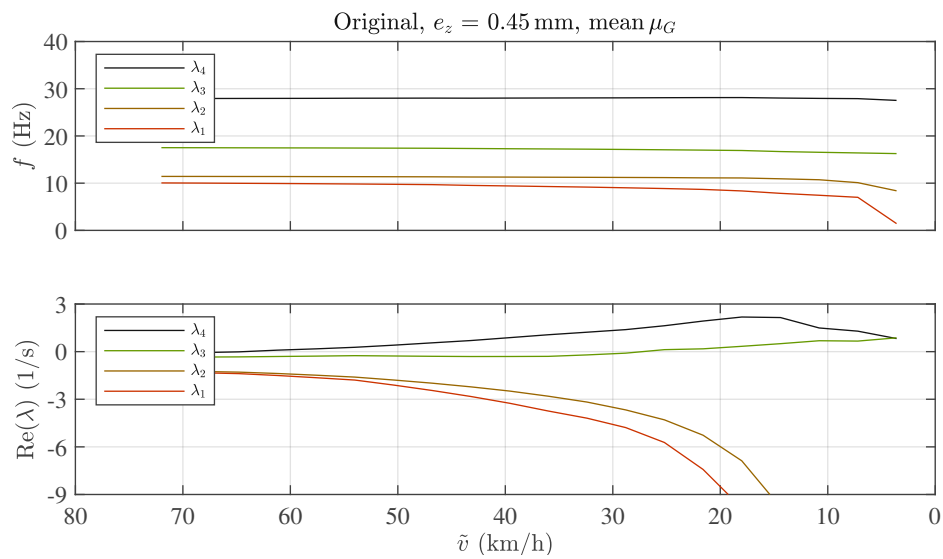


Figure 6.6: Eigenvalues: Original Design

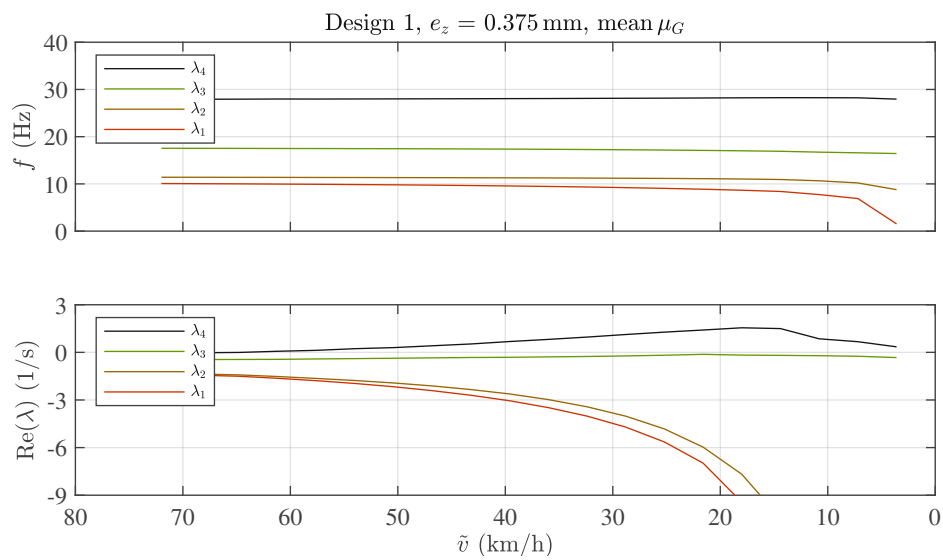


Figure 6.7: Eigenvalues: Design 1

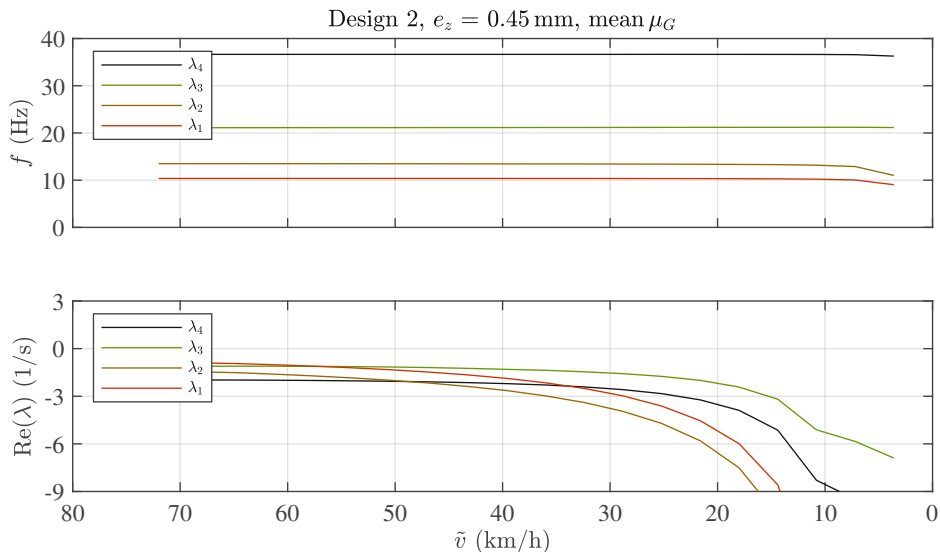


Figure 6.8: Eigenvalues: Design 2

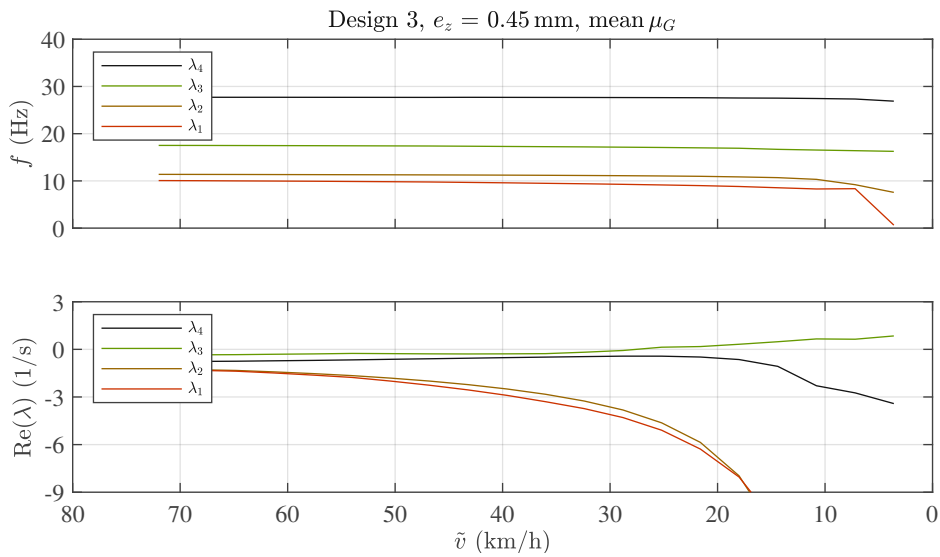


Figure 6.9: Eigenvalues: Design 3

6.2.3 Comparison of the designs in the time domain

The quasi-static analysis has shown that the proposed designs may affect brake forces (positively or negatively), Section 6.2.1. The modal analysis has shown that the design changes discussed may be able to stabilise the system, Section 6.2.2. To investigate how the designs affect vibration amplitudes of the magnetic track brake during a braking manoeuvre, time integration results are compared.

For parameters $e_z = 0.45$ mm (Original Design and Designs 2 and 3) and $e_z = 0.375$ mm (Design 1), time integrations of braking manoeuvres are performed, Figure 6.10. For these values of e_z , the maximum real parts of eigenvalues were determined before, Figure 6.5. Over a simulation time of 8 s the model is decelerated from an initial velocity of $v_{vcl} = 43.2$ km/h until full stop, Figure 6.10 (a). The track brake is activated at a simulation time of $t = 0.5$ s and deactivated at $t = 7$ s at $v_{vcl} = 3$ km/h. During the deceleration, the coefficient of friction μ_G increases continuously. Figure 6.10 (b)-(e) show the longitudinal transmission forces $F_{B,j,x}$, with $j = A, C$. The results are referenced with respect to the equivalent brake force (1.19) of the Original model.

The results obtained for the Original Design and $e_z = 0.45$ mm are similar to those reported in Chapter 5.3 and show severe vibrations at low velocities, Diagram (b). At 12 km/h the mechanical stops of the brake frame and the bogie lose contact in longitudinal direction, which leads to impact loads between the bogie and the magnetic track brake.

Diagram (c) depicts the time integration results for Design 1 with asymmetric oscillations of $F_{B,j,x}$ evolving. At $t = 6.5$ s and $v_{vcl} = 5$ km/h however, a limit cycle is reached. For $v < 5$ km/h, amplitudes of $F_{B,j,x}$ decrease again.

Design 2 is superior with stable behaviour over the entire braking manoeuvre and increased brake forces, Diagram (d).

Although in the locally linearised model of Design 3, λ_3 has positive real parts $\text{Re}(\lambda_3) > 0$ at low velocities $v_{vcl} < 25$ km/h, no vibration amplitudes are visible in Diagram (e). This is because a limit cycle with only very small amplitudes arises in the time integration, which are irrelevant for the loads on the structure. Thus, Design 3 also represents a technically preferable variant compared to the Original Design, which can be easily implemented.

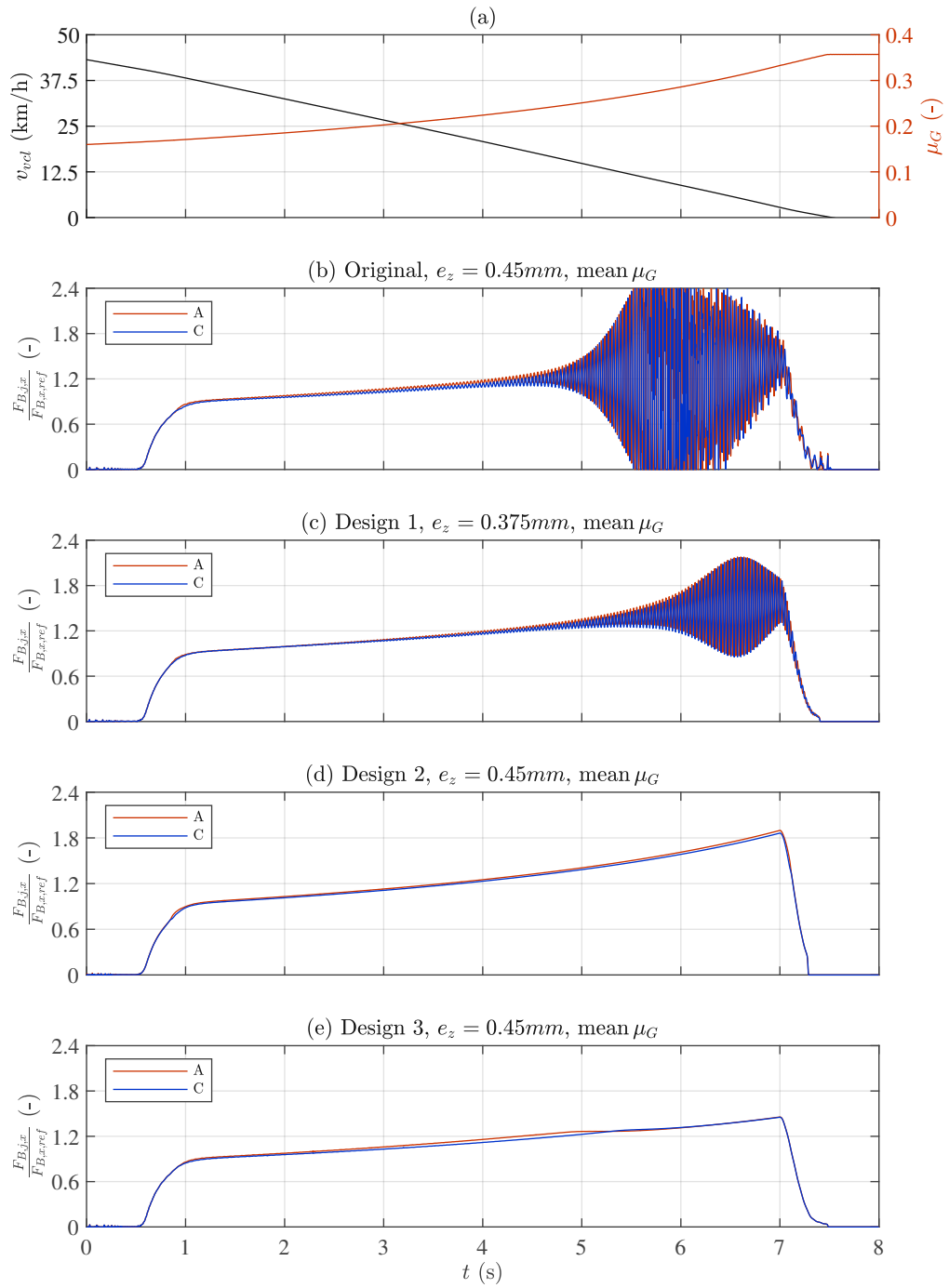


Figure 6.10: Comparison of time integration results

Conclusions and Outlook

7.1 Conclusions

To reduce mechanical loads on magnetic track brakes at low velocities and subsequently apply them also in the low velocity range, the aim of this thesis was to investigate self-excited vibrations of magnetic track brakes and how to reduce them in future designs. To develop efficient methods of mitigation, research was focused on the underlying self-excitation mechanisms and to identify the source of energy which maintains the vibrations of the brake frame. Engineering measures based on the findings of this thesis should help to avoid vibrations in future track brakes.

During vehicle tests, severe self-excited structural vibrations of a magnetic track brake were measured at low vehicle velocities. The analysis of measurement data in Chapter 2 showed that the vibrations correspond to an asymmetric deflection mode of the brake frame at a constant frequency, and high vibration amplitudes correlate with high brake forces. Since the analysis of data could not explain the origin of the self-excited vibrations, the following chapters focused on the modelling and simulation of self-excited vibrations of a magnetic track brake.

Because previous mathematical models of magnetic track brakes from the literature [40] and [46] are unsuitable to examine the stability behaviour, new electric, magnetic and mechanical sub-models were developed and subsequently assembled to system models, Chapter 3. For the study of the self-excitation mechanisms, simplified analytical planar models were developed considering the lateral deformation of the magnetic track brake frame. To obtain simulation results that are qualitatively comparable with vehicle tests, a 3D multibody dynamics model of the magnetic track brake including a flexible brake frame and multiple brake magnets was developed.

The stability of the simplified and locally linearised models was analysed in Chapter 4 by applying the Hurwitz criterion. The evaluation of the criterion for oscillatory stability

showed that, on the one hand, the rising coefficient of friction during braking leads to small (or negative) damping terms which de-stabilises the system. This self-excitation mechanism corresponds to the type of friction-induced self-excited vibrations discussed in [20] and [21]. On the other hand, it was found that the coupling of the equation of motion and the electro-magnetic differential equation results in a 1.5 DoF system which is capable of self-excitation. This mechanism is similar to the inertial self-excitation type described in [24]. For multiple magnet configurations, the coupling is amplified with the electrical in series connection of two magnets for asymmetric deflection modes. By analysing stability maps, design parameters were identified which can be modified to improve stability.

Obviously, the system is fed by two energy sources:

On the one hand, a permanent supply of electrical energy from the voltage source is provided to the electrical circuit. On the other hand, the moving train provides kinetic energy to the mechanical sub-system.

Over one period of the limit cycle, the energy flow of the electrical, magnetic and mechanical sub-models, as well as the overall system model, was studied. Time signals show a phase shift between the magnetic attraction force as well as the friction force and the relative lateral motion of the magnet and the rail which allows energy to be transferred from the friction contact to the oscillating system. The magnetic restoring force acting in the lateral direction performs work at the air-gap and transfers energy from the mechanical system to the magnetic system. Kinetic energy of the train allows the work of braking, the work in the air-gap and to overcome the dissipative losses in the mechanical and magnetic systems.

With the more complex multibody dynamics model, it was shown in Chapter 5 that self-excited vibrations are not only dependent on the design, but also on operational parameters and environmental influences. It was demonstrated that the contact points between the pole shoes and the rail are variable during braking and depend on the size of pick-up weldings and the coefficient of friction. The increase in the coefficient of friction at low velocities can result in abrupt changes in the contact status between the magnet and the rail and in the stability behaviour. Stability analyses showed that the stability depends on both friction and velocity. A comparison with vehicle test data showed that time-integration results obtained with the multibody dynamics model are qualitatively comparable with vehicle tests.

Aiming at the reduction of the electromagnetic-mechanical coupling, three design proposals were developed to mitigate self-excited vibrations, Chapter 6. In Design 1, the stiffness of the brake frame was increased by 20% which leads to smaller vibration amplitudes but also to a reduction in brake force due to a less adaptable brake frame. In Design 2, the mechanical stops between the track brake and the bogie were relocated in order to minimise bending moments induced by transmission forces. As a result, self-excited vibrations were eliminated, and brake forces increased. Mitigation of vibrations with minimal design changes was achieved in Design 3, where the electrical connections of the magnets were changed.

7.2 Outlook


During the progress of this thesis, major research questions on self-excited vibrations of magnetic track brakes have been addressed. However, new questions and further ideas arose which have not been examined in this thesis. Since the area of interest is relatively new, there is a wide field of activity for further research.

Measures presented so far to prevent vibrations are exclusively of a passive type. The development of active systems such as anti-vibration controllers will be considered in a following research project. Intuitively, the electrical voltage or current, but also the pressure applied to the actuating cylinders, could be used as control variables. Feedback controllers with electrical control variables require a more detailed modelling of the electrical power supply present on trains. If the actuation cylinder pressure is used, the model must be extended by a pneumatic sub-model.

With the locally linearised basic and more detailed multibody dynamics models, parameter areas of asymptotically stable equilibrium positions were determined. A next step to deepen the understanding would be non-linear stability analyses of the discussed models. To specify regions of perturbations in which trajectories tend towards stable solutions, bifurcation analyses [16] can be performed using continuation algorithms. The study of structural changes of non-linear solutions as a function of input parameters such as vehicle speed and source voltage, will describe the behaviour of the system beyond the present findings. This includes the detection of Hopf bifurcations and the evaluation of amplitudes of the resulting (stable) limit cycles. This is particularly relevant as in the development of engineering solutions with the aim of reducing loads, periodic vibrations with limited amplitudes can also represent permissible operating states.

Velocity-dependent friction has so far been considered phenomenologically. The underlying contact mechanical problem however, has not been considered in detail and is also a starting point for further studies. This includes the analysis and modelling of the local three-dimensional pole shoe-rail contact area and the calculation of the normal forces, as well as the friction law, considering multi-physical influences such as third-body layers, adhesion and contamination.

The dynamical coupling between magnetic forces, frictional forces and the relative motion between the magnet and the rail is responsible for the "inertial" self-excitation mechanism. The study of so far neglected effects such as non-linear, hysteretic ferromagnetic behaviour, as well as dynamical characteristics of the sliding friction contact between pole shoes and rail, will advance the understanding of this mechanism.

Magnetic track brakes are components of railway vehicles that are under high mechanical loads, often indispensable for operation and safety-relevant. The design, development and optimisation of magnetic track brakes therefore requires a high degree of accuracy and a precise understanding of their behaviour in operation. Continuing application-oriented basic research on magnetic track brakes is relevant, useful and highly recommended to advance technical progress in the field of braking systems for .

Measurement channels

The physical quantities are measured by sensors applied to the brake, the bogie or the carbody. Depending on the measuring principle, the signals are acquired by bridge and differential amplifiers or bus (NMEA, CAN) and recorded by three synchronised data loggers, Figure A.1. Table A.1 gives an overview of the signals measured during the vehicle tests, compare Figure 2.1.

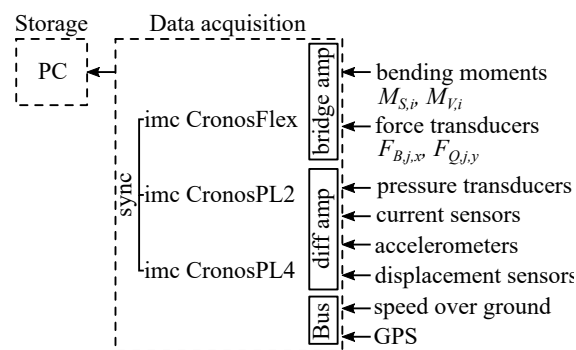


Figure A.1: Data acquisition

Table A.1: List of measurement channels

Pos.	Symbol	Sensor type	Long name	DAQ
1	$F_{B,A,x}$	full bridge	brake force left, front	bridge
2	$F_{B,B,x}$	full bridge	brake force left, rear	bridge
3	$F_{B,C,x}$	full bridge	brake force right, front	bridge
4	$F_{B,D,x}$	full bridge	brake force right, rear	bridge
5	$F_{Q,A,x}$	full bridge	lateral force left, front	bridge
6	$F_{Q,B,x}$	full bridge	lateral force left, rear	bridge
7	$F_{Q,C,x}$	full bridge	lateral force right, front	bridge
8	$F_{Q,D,x}$	full bridge	lateral force right, rear	bridge
5	$M_{V,le-fr,y}$	half bridge	connector bending y left, front	bridge
6	$M_{V,le-re,y}$	half bridge	connector bending y left, rear	bridge
7	$M_{V,ri-fr,y}$	half bridge	connector bending y right, front	bridge
8	$M_{V,ri-re,y}$	half bridge	connector bending y right, rear	bridge
9	$M_{V,le-fr,z}$	half bridge	connector bending z left, front	bridge
10	$M_{V,le-mi,z}$	half bridge	connector bending z left, centre	bridge
11	$M_{V,le-re,z}$	half bridge	connector bending z left, rear	bridge
12	$M_{V,ri-fr,z}$	half bridge	connector bending z right, front	bridge
13	$M_{V,ri-mi,z}$	half bridge	connector bending z right, centre	bridge
14	$M_{V,ri-re,z}$	half bridge	connector bending z right, rear	bridge
15	$M_{S,fr-le,x}$	half bridge	track rod bending x front, left	bridge
16	$M_{S,fr-mi,x}$	half bridge	track rod bending x front, centre	bridge
17	$M_{S,fr-ri,x}$	half bridge	track rod bending x front, right	bridge
18	$M_{S,re-le,x}$	half bridge	track rod bending x rear, left	bridge
19	$M_{S,re-mi,x}$	half bridge	track rod bending x rear, centre	bridge
20	$M_{S,re-ri,x}$	half bridge	track rod bending x rear, right	bridge
21	$M_{S,fr-le,z}$	half bridge	track rod bending z front, left	bridge
22	$M_{S,fr-mi,z}$	half bridge	track rod bending z front, centre	bridge
23	$M_{S,fr-ri,z}$	half bridge	track rod bending z front, right	bridge
24	$M_{S,re-le,z}$	half bridge	track rod bending z rear, left	bridge
25	$M_{S,re-mi,z}$	half bridge	track rod bending z rear, centre	bridge
26	$M_{S,re-ri,z}$	half bridge	track rod bending z rear, right	bridge
27	$F_{cyl,j,z}$	pressure p_{cyl}	actuation cylinder force left front	diff
28	$s_{A,y}$	linear transducer	lateral displacement left front	diff
29	$s_{B,y}$	linear transducer	lateral displacement left rear	diff
30	$s_{C,y}$	linear transducer	lateral displacement right front	diff
31	$s_{D,y}$	linear transducer	lateral displacement right rear	diff
32	$s_{A,z}$	linear transducer	vertical displacement left front	diff
33	$s_{B,z}$	linear transducer	vertical displacement left rear	diff
34	$s_{C,z}$	linear transducer	vertical displacement right front	diff
35	$s_{D,z}$	linear transducer	vertical displacement right rear	diff

Continued on next page

Table A.1 – continued from previous page

Pos.	Symbol	Sensor type	Long name	DAQ
36	$a_{DG,x}$	piezo ICP	bogie, dynamic accerleration x	diff/ICP
37	$a_{DG,y}$	piezo ICP	bogie, dynamic accerleration y	diff/ICP
38	$a_{DG,z}$	piezo ICP	bogie, dynamic accerleration z	diff/ICP
39	$a_{MG,x}$	piezo ICP	track brake, dynamic accerleration x	diff/ICP
40	$a_{MG,y}$	piezo ICP	track brake, dynamic accerleration y	diff/ICP
41	$a_{MG,z}$	piezo ICP	track brake, dynamic accerleration z	diff/ICP
42	i_A	hall current probe	current, left front	diff
43	i_B	hall current probe	current, left rear	diff
44	i_C	hall current probe	current, right front	diff
45	i_D	hall current probe	current, right rear	diff
46	$a_{vcl,x}$	capacitive	acceleration vehicle	diff
47	$v_{vcl,x}$	optical	velocity vehicle	CAN
48	$s_{vcl,x}$	optical	distance travelled	CAN
49	GPS	GPS antenna	position	NMEA

Identification of system parameters

B.1 Identification of contact parameters

Analyses with the multibody dynamics model aim to calculate simulation results that are comparable with vehicle tests, Chapter 5. To reproduce the behaviour of the magnetic track brake, knowledge of the contact conditions of the magnets on the rail is relevant. These are determined by the geometric tolerances of the intermediate elements and the coil body, Figure 3.3. Pick-up weldings on the pole shoes, as well as external forces, can cause the positions of the contacts to shift during braking which makes the identification more difficult. This section presents a method to estimate the contact parameters of the multibody dynamics model based on vehicle test data.

In the multibody dynamics model, the contact points between the magnet and the rail are simulated by three contact points, Figure 3.7. The position of the intermediate contact point is defined by the coordinates e_x and e_z . In Section 2.2, the track brake activation process is analysed and split into different phases, Figure 2.5. In *Phase III*, the track brake comes into contact with the rail but electric voltage is not yet applied. The brake is pressed onto the rail only by the force of the actuation cylinders F_{cyl} .

Figure B.1 shows the state of a brake magnet at the beginning of *Phase III*, assuming a pick-up welding at the centre intermediate element. The position and height of the pick-up welding is defined by e_x and e_z . In the figure, neither the inward, nor the outward endpiece is in contact with the rail yet. The actuation cylinder force F_{cyl} increases with the pressure p_{cyl} , which causes a bending moment in the connecting beam $M_{V,y}$. The connector beam is bent about the intermediate contact point until contact is established between the outward end piece and the rail.

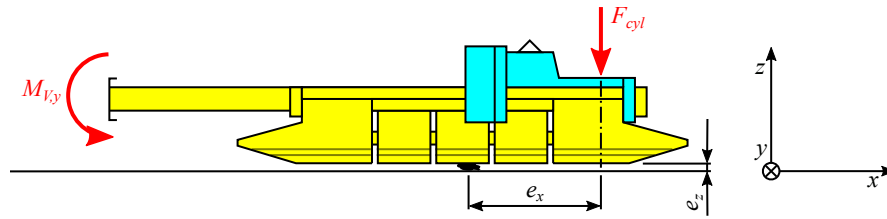


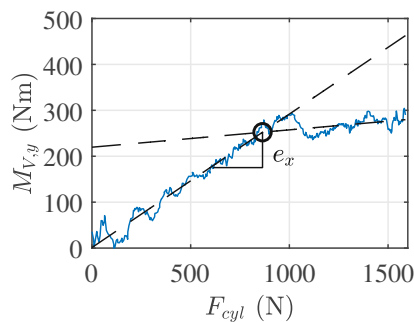
Figure B.1: Track brake-rail contact

e_z and e_x are evaluated from the $M_{V,y}$ - F_{cyl} diagram, Figure B.2(a). Starting at $F_{cyl} = 0$, $M_{V,y} = 0$, $M_{V,y}$ increases roughly linearly with F_{cyl} . The slope of the linear regression (dashed line) equals the longitudinal distance e_x between the contact point and the line of action of F_{cyl} , (B.1).

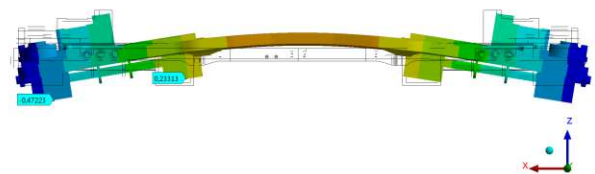
$$e_x = \frac{\Delta M_{V,y}}{\Delta F_{cyl}} \quad (\text{B.1})$$

A kink in the $M_{V,y}$ - F_{cyl} characteristics marks an increase of stiffness at the moment the endpiece comes into contact with the rail. Again, the characteristics are roughly linear. With the distance e_x and the cylinder force F_{cyl} , the deformation of the track brake is calculated in a finite element analysis, Figure B.2(b). The vertical deflection of the outward endpieces in the figure equals to e_z .

The method is used to evaluate e_x and e_z for the selected measurements V1008 and V1014, Table B.1. For both measurements, a longitudinal distance of $e_x \approx 31$ cm is derived which corresponds to the position of the centre intermediate element. As a result, the inward endpieces are not in contact with the rail.



(a) bending moment vs. cylinder force



(b) vertical deformation under cylinder load

Figure B.2: Analysis of contact conditions between the track brake and the rail

Test ID	e_x	e_z	Comment
V1008	31 cm	0.47 mm	vibrations, high brake force
V1014	31 cm	0.80 mm	no vibrations, low brake force

Table B.1: Coordinates of intermediate contact points during field tests

B.2 Identification of the effective air-gap

The magnetic forces derived from the magnetic sub-model strongly depend on the effective air-gap s , Section 3.2. s influences both the reluctance of the air gap R_m (3.10) and as a result the magnetic flux ϕ (3.9). A (small) effective air gap between the pole shoes and the rail is always present during braking due to imperfections of the contacting geometries. The assumption of a realistic values for s is required to qualitatively investigate the behaviour of the magnetic track brake.

This section presents a method to determine s by comparing normalised magnetic attraction forces derived from laboratory tests and the vehicle tests presented in Section 2.2.

Measurement of magnetisation curves

Assuming the magnetic attraction force F_A can be calculated from (B.2), the magnetic flux ϕ through the pole shoes of a brake magnet is measured in a laboratory experiment for varying air-gaps s .

$$F_A = \frac{\phi^2}{2\mu_0 A} \quad (\text{B.2})$$

A setup based on [58] is used to measure ϕ - i magnetisation curves, Figure B.3(a). A magnetic track brake with a secondary winding on a pole shoe is placed on a rail. Different dimensions of the air-gap between the magnet and the rail are simulated by sheets of non-magnetic material. The magnetic circuit is excited by the coil of the electromagnet with the number of windings N and the current i . The magnetic flux ϕ near the air-gap, is measured by evaluating the voltage induced in the secondary winding u_2 (B.3).

$$u_2 = N_2 \dot{\phi} \quad (\text{B.3})$$

With the number of turns N_2 and $s = 0.0$ - 1.2 mm, ϕ - i characteristics are determined, Figure B.3(b). For $s = 0.0$ mm, the ferromagnetic saturation of the magnetic circuit is clearly visible for $i > 4$ A. The saturation shifts towards higher excitation currents as the distance between the magnet and the rail increases.

From the measured data, $F_A(s, i)$ is calculated by (B.2) and normalised using reference values for each air gap $F_{A,ref}(s, i = i_{ref})$, with $i_{ref} = 10$ A:

$$\frac{F_A(s, i)}{F_{A,ref}(s, i_{ref})} = \frac{\frac{\phi(s, i)^2}{2\mu_0 A}}{\frac{\phi_{ref}(s)^2}{2\mu_0 A}} = \frac{\phi(s, i)^2}{\phi_{ref}(s)^2} \quad (\text{B.4})$$

The characteristics of the resulting normalised attraction force $\frac{F_A}{F_{A,ref}}$ with respect to i vary with the air gap, Figure B.4(a).

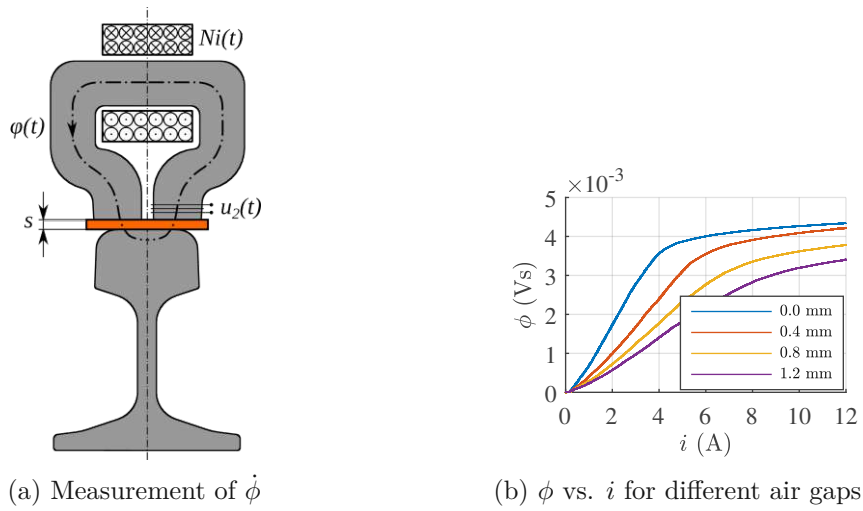


Figure B.3: Measurement of the magnetic flux

Comparison of magnetisation curves and field tests

To determine the effective air gap at the beginning of a braking manoeuvre, measurements from vehicle test are compared with the normalised magnetic attraction forces. As the pole shoes were not equipped with secondary windings during the driving tests, instead of ϕ the signals of the brake forces are used. Assuming the velocity $v_{vcl} \approx \text{const.}$ and the coefficient of friction $\mu_G \approx \text{const.}$ during the electric activation, the magnetic attraction force F_A in (B.4) can be substituted by the brake force $F_{B,x}$, Equation (B.5):

$$\frac{F_{B,x}}{F_{B,x,ref}} = \frac{\mu_G F_A}{\mu_G F_{A,ref}} = \frac{\phi^2}{\phi_{ref}^2} \quad (\text{B.5})$$

The relevant data is extracted from the track brake activation process described in Section 2.2. In *Phase IV* of the activation process, the track brake is electrically activated, see Figure 2.5. At the beginning of this phase, the track brake is in contact with the rail and pressed towards the rails by the actuation cylinders but the electric voltage is not yet applied. During the build-up phase of ≈ 0.5 s, the current and the brake forces increase from zero to a "steady" value.

Figure B.4(b) shows the normalised brake force with respect to the current i for measurement *V1008*. By comparing the characteristics of the normalised attraction forces (Figure B.4(a)) and the brake forces (Figure B.4(b)), the effective air gap s is estimated for the beginning of each braking manoeuvre.

For selected braking manoeuvres, Figure B.5 shows the effective air gaps determined using this method. The records *V1006*, *V1007* and *V1008* form a group in the range of $s = 0.6$ - 0.9 mm. For *V1014* and *V1019* effective air gaps of $s > 3$ mm are identified which indicates severe pick-up weldings.

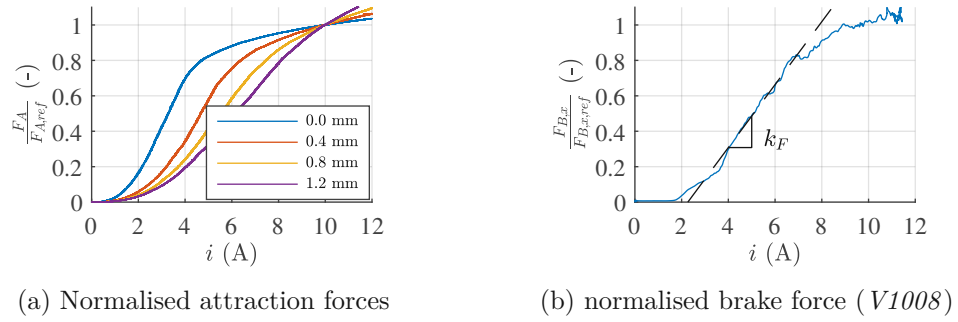


Figure B.4: Normalised forces

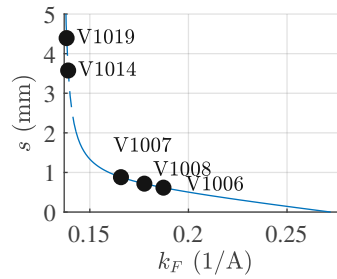


Figure B.5: Effective air gaps during the field tests

Bibliography

- [1] UIC 541-06: Brakes - Specifications for the construction of the various brake components - Magnetic brakes. UIC Code (2013). International Union of Railways
- [2] EN 16207:2014+A1:2019: Railway applications - Braking - Functional and performance criteria of Magnetic Track Brake systems for use in railway rolling stock. European standard (2019). European Committee for Standardization
- [3] Ergänzungsregelung Nr. B 012 für die technische Gestaltung der Magnetschienenbremse in Schienenfahrzeugen, Rev.6. Arbeitsgruppe DB/EBA/VDB/VDV (2018). Eisenbahn Bundesamt
- [4] Arias-Cuevas, O. and Li, Z.: Field investigations into the performance of magnetic track brakes of an electrical multiple unit against slippery tracks. Part 1: Adhesion improvement. *Proceedings of the Institution of Mechanical Engineers, Part F: Journal of Rail and Rapid Transit* 225, 613–636 (2011)
- [5] Arias-Cuevas, O. and Li, Z.: Field investigations into the performance of magnetic track brakes of an electrical multiple unit against slippery tracks. Part 2: Braking force and side effects. *Proceedings of the Institution of Mechanical Engineers, Part F: Journal of Rail and Rapid Transit* 226, 72–94 (2012)
- [6] ERRI B126/DT371: Braking problems – Precalculating the performance of the magnetic track brake. Technical report (1999). European Rail Research Institute
- [7] Gfatter, G., Haas, S., and Vohla, G.: *Schienenbremsen – Track Brakes*. Knorr-Bremse GmbH, Mödling, 1st edn. (2004)
- [8] Jirout, M.: *Mechanische Auslegung von Magnetschienenbremsen*. Dissertation, Technische Universität Wien (2006)
- [9] Hendrichs, W.: Das statische, dynamische und thermische Verhalten von Magnetschienenbremsen, Teil 3. *Elektrische Bahnen* 86, 357–360 (1988)
- [10] Bode, O., Fritzsche, G., Humburg, K., and Sudikatis, G.: Untersuchungen über das Verhalten von Magnetschienenbremsen im Straßenbahnbetrieb. *Deutsche Kraftfahrzeugforschung und Straßenverkehrstechnik* 107 (1957)

- [11] Montgomery, R. S.: Friction and wear at high sliding speeds. *Wear* 36, 275–298 (1976)
- [12] Desplanques, Y., Roussette, O., Degallaix, G., Copin, R., and Berthier, Y.: Analysis of tribological behaviour of pad–disc contact in railway braking. *Wear* 262, 582–591 (2007)
- [13] Leipholz, H.: *Stability theory: an introduction to the stability of dynamic systems and rigid bodies*. Teubner, Stuttgart, 2nd edn. (1987). ISBN 3519021056
- [14] Mack, W. and Plöchl, M.: Stabilitätsprobleme bewegter Systeme. Lecture notes (2009). Technische Universität Wien
- [15] Müller, P. C. and Schiehlen, W. O.: *Linear vibrations: a theoretical treatment of multi-degree-of-freedom vibrating systems*. Mechanics, dynamical systems. Martinus Nijhoff Publ., Dordrecht (1985). ISBN 9024729831
- [16] Kuznetsov, Y. A.: *Elements of Applied Bifurcation Theory*. Springer New York, 3rd edn. (2004). ISBN 978-1-4757-3978-7
- [17] Della Rossa, F., Mastinu, G., and Piccardi, C.: Bifurcation analysis of an automobile model negotiating a curve. *Vehicle System Dynamics* 50, 1539–1562 (2012)
- [18] Panciroli, R. and Abrate, S.: An Introduction to Self-Excited Oscillations. In *Proceedings of the ASME 2009 International Mechanical Engineering Congress and Exposition*, 69–78 (2009)
- [19] Hoffmann, N. and Gaul, L.: Effects of damping on mode-coupling instability in friction induced oscillations. *Zeitschrift für angewandte Mathematik und Mechanik* 83, 524–534 (2003)
- [20] Popp, K.: Modelling and control of friction-induced vibrations. *Mathematical and Computer Modelling of Dynamical Systems* 11, 345–369 (2005)
- [21] Chen, G.: Friction–vibration interactions. In *Handbook of Friction-Vibration Interactions*, 153–305. Woodhead Publishing (2014). ISBN 978-0-85709-458-2
- [22] Ibrahim, R. A.: Friction-Induced Vibration, Chatter, Squeal, and Chaos—Part I: Mechanics of Contact and Friction. *Applied Mechanics Reviews* 47, 209–226 (1994)
- [23] Hoffmann, N., Fischer, M., Allgaier, R., and Gaul, L.: A minimal model for studying properties of the mode-coupling type instability in friction induced oscillations. *Mechanics Research Communications* 29, 197 – 205 (2002)
- [24] Babitsky, V. I. and Landa, P. S.: Auto-oscillation Systems with Inertial Self-excitation. *ZAMM - Journal of Applied Mathematics and Mechanics / Zeitschrift für Angewandte Mathematik und Mechanik* 64, 329–339 (1984)

- [25] EN 13452:2003: Railway applications - Braking - Mass transit brake systems - Part 1: Performance requirements. European standard (2003). European Committee for Standardization
- [26] EN 13674-1:2011+A1:2017: Railway applications - Track - Rail - Part 1: Vignole railway rails 46 kg/m and above. European standard (2017). European Committee for Standardization
- [27] Olsson, H., Åström, K., Canudas de Wit, C., Gäfvert, M., and Lischinsky, P.: Friction Models and Friction Compensation. *European Journal of Control* 4, 176–195 (1998)
- [28] Ettles, C. M. M.: The Thermal Control of Friction at High Sliding Speeds. *Journal of Tribology* 108, 98–104 (1986)
- [29] Hale, C. S., Palazotto, A. N., and Baker, W. P.: Engineering Approach for the Evaluation of Mechanical Wear Considering the Experimental Holloman High-Speed Test Track. *Journal of Engineering Mechanics* 138, 1127–1140 (2012)
- [30] Lewis, R. and Olofsson, U.: Basic tribology of the wheel–rail contact. In *Wheel–Rail Interface Handbook*, 34–57. Woodhead Publishing (2009). ISBN 978-1-84569-412-8
- [31] Godet, M.: The third-body approach: A mechanical view of wear. *Wear* 100, 437–452 (1984)
- [32] Kalker, J. J.: *On the rolling contact of two elastic bodies in the presence of dry friction*. Dissertation, Technische Hogeschool Delft (1967)
- [33] Kalker, J. J.: A Fast Algorithm for the Simplified Theory of Rolling Contact. *Vehicle System Dynamics* 11, 1–13 (1982)
- [34] Polach, O.: A Fast Wheel-Rail Forces Calculation Computer Code. *Vehicle System Dynamics* 33, 728–739 (1999)
- [35] Zhang, W., Chen, J., Wu, X., and Jin, X.: Wheel/rail adhesion and analysis by using full scale roller rig. *Wear* 253, 82–88 (2002)
- [36] Polach, O.: Creep forces in simulations of traction vehicles running on adhesion limit. *Wear* 258, 992 – 1000 (2005). Contact Mechanics and Wear of Rail/Wheel Systems
- [37] Logston, C. F. and Itami, G. S.: Locomotive Friction-Creep Studies. *Journal of Engineering for Industry* 102, 275–281 (1980)
- [38] Fletcher, D. and Lewis, S.: Creep curve measurement to support wear and adhesion modelling, using a continuously variable creep twin disc machine. *Wear* 298-299, 57–65 (2013)

- [39] Kurzeck, B.: Combined friction induced oscillations of wheelset and track during the curving of metros and their influence on corrugation. In *Proceedings of the 8th International Conference on Contact Mechanics and Wear of Rail/Wheel Systems, Florence, 2009*, 299–310 (2009)
- [40] Jirout, M., Mack, W., and Lugner, P.: Non-smooth dynamics of a magnetic track brake. *Regular and Chaotic Dynamics* 14, 673–681 (2009)
- [41] Döbrössy, A.: *Simulation des Anzugsvorganges einer Magnetschienenbremse in Tiefaufhängung*. Master's thesis, FH Campus Wien (2013)
- [42] Cruceanu, C. and Craciun, C.: Necessity and conditionality regarding the electromagnetic track brake - parametric study. *MATEC Web of Conferences* 178 (2018)
- [43] Lu, S., Gu, Y., Chen, S., and Wang, S.: A Numerical Method of the Electromagnetic Force for the Electromagnetic Track Brake. *Applied Mechanics and Materials* 253-255, 2159–2162 (2012)
- [44] Galardi, E., Meli, E., Nocciolini, D., Pugi, L., and Rindi, A.: Development of efficient models of Magnetic Braking Systems of railway vehicles. *International Journal of Rail Transportation* 3, 97–118 (2015)
- [45] Kallenbach, E., Eick, R., Quendt, P., Ströhla, T., Feindt, K., Kallenbach, M., and Radler, O.: *Elektromagnete*. Vieweg Teubner Verlag (2012)
- [46] Darula, R. and Sorokin, S.: Simplifications in modelling of dynamical response of coupled electro-mechanical system. *Journal of Sound and Vibration* 385, 402–414 (2016)
- [47] Tippelt, D.: *Dynamische Simulation einer Magnetschienenbremse in Hochlage*. Diploma thesis, Technische Universität Wien (2011)
- [48] IEC 61373:2010: Railway applications - Rolling stock equipment - Shock and vibration tests. International Standard (2011). International Electrotechnical Commission
- [49] Pötscher, J.: *Berechnung und Validierung eines Modells einer Haftkraftwaage mittels Finite Elemente Methode*. Master's thesis, Technische Universität Wien, Wien (2016)
- [50] Tippelt, D., Edelmann, J., Plöchl, M., and Jirout, M.: Analysis of Self-excited Vibrations of an Electromagnetic Track Brake. In Klomp, M., Bruzelius, F., Nielsen, J., and Hillemyr, A., eds., *Advances in Dynamics of Vehicles on Roads and Tracks*, 442–451. Springer International Publishing, Cham (2020). ISBN 978-3-030-38077-9
- [51] Tippelt, D., Edelmann, J., Plöchl, M., and Jirout, M.: Modelling, analysis and mitigation of self-excited vibrations of a magnetic track brake. *Proceedings of the Institution of Mechanical Engineers, Part F: Journal of Rail and Rapid Transit* (2021)

- [52] Hendrichs, W.: Das statische, dynamische und thermische Verhalten von Magnetschienenbremsen, Teil 1. *Elektrische Bahnen* 86, 224–228 (1988)
- [53] Dassault Systemes Simulia Corp.: *Simpack 2017 Documentation* (2016)
- [54] Craig, R. R. and Bampton, M. C.: Coupling of substructures for dynamic analyses. *AIAA Journal* 6, 1313–1319 (1968)
- [55] Craig, R. R. and Kurdila, A. J.: *Fundamentals of Structural Dynamics*. WILEY (2006). ISBN 978-0-471-43044-5
- [56] The MathWorks, Inc.: *MATLAB Function Reference*, 2021b edn. (2021)
- [57] Kara, G. and Erdoğan, S.: Methods for reducing the specific mass of rolling stock. *Engineering Science and Technology, an International Journal* 16, 59–66 (2013)
- [58] Hendrichs, W.: Das statische, dynamische und thermische Verhalten von Magnetschienenbremsen, Teil 2. *Elektrische Bahnen* 86, 324–330 (1988)